CHARACTERIZATION OF THE GLOBAL HAWK LOW PRESSURE TURBINE FIRST ROTOR

THESIS

Timothy L. Garmoe, Captain, USAF

AFIT/GAE/ENY/05-S02

DEPARTMENT OF THE AIR FORCE
AIR UNIVERSITY

AIR FORCE INSTITUTE OF TECHNOLOGY

Wright-Patterson Air Force Base, Ohio

AFIT/GAE/ENY/05-S02

CHARACTERIZATION OF THE GLOBAL HAWK LOW PRESSURE TURBINE FIRST ROTOR

THESIS

Presented to the Faculty

Department of Aeronautics and Astronautics

Graduate School of Engineering and Management

Air Force Institute of Technology

Air University

Air Education and Training Command

In Partial Fulfillment of the Requirements for the

Degree of Master of Science in Aeronautical Engineering

Timothy L. Garmoe, BS

Captain, USAF

September 2005

AFIT/GAE/ENY/05-S02

CHARACTERIZATION OF THE GLOBAL HAWK LOW PRESSURE TURBINE FIRST ROTOR

Timothy L. Garmoe, BS
Captain, USAF

Approved:

//signed//	2 September 2005
Paul I. King Committee Chairman	date
//signed//	2 September 2005
Milton E. Franke Committee Member	date
//signed//	2 September 2005
Raymond C. Maple, Lt. Col. USAF Committee Member	date

Abstract

The Air Force Research Laboratory, Propulsion Directorate at Wright Patterson Air Force Base has studied the performance of turbine blade geometries utilizing a large scale, low speed, drawdown wind tunnel in an effort to better understand gas turbine blade aerodynamics. Currently, the Air Force's Unmanned Aerial Vehicle (UAV) Global Hawk has been operated primarily at flight conditions other than the design point of its Allison AE3007H turbofan engine. This off design condition decreased the Reynolds number at the low pressure turbine causing losses in efficiency and loading. Two different blades were studied to maximize performance of the Global Hawk turbine. The first was an experimental, high turning angle blade designated the Pak-B and the second was based on the two dimensional mean diameter section of the first stage blade of the low pressure turbine used in the Global Hawk (GH1R). The Pak-B blade has been the subject of past research.

The primary goals of this study were to validate the wind tunnel after previous upgrades, physically modify the test section to accept the Global Hawk blades, and to characterize the GH1R blades.

A Reynolds number sweep was performed from 10K to 100K by 5K increments on a linear turbine cascade of 8 first rotor test blades. Measurements of wake velocity, total pressure losses, and boundary layer velocity were made to examine the flow. These measurements resulted in an averaged integrated total pressure loss profile for the Global Hawk first rotor. The operational primary mission inlet Reynolds number for the GH1R blade was calculated to be 13,500 and compared to the loss profile. It was shown that the Global Hawk first rotor has much lower losses than that of the Pak-B blade, and shows no signs of mid-line separation.

Acknowledgments

I would like to express my sincere appreciation to my faculty advisor, Dr. Paul King, for his guidance and support throughout my tenure here at AFIT as well as during the course of this thesis effort. The insight and support offered was certainly appreciated. I would, also, like to thank my sponsor, Dr. Rolf Sondergaard of AFRL/PRTT for both the support and latitude provided to me in this endeavor.

Timothy L. Garmoe

Table of Contents

Page

List of Figures

Page

Page

Page

Page

Page

List of Tables

Page

List of Symbols

Symbol	Definition
C	Calibration curve fit constant, y – intercept
c	Axial chord length (m)
C_D	Aircraft drag coefficient
C_L	Aircraft lift coefficient
C_P	Pressure coefficient
c_P	Specific heat at constant pressure (J/kg K)
D	Calibration curve fit constant, curve slope
D	Diameter (m)
dP	Differential change in pressure (Pa)
ds	Differential change in entropy (J/kg K)
dT	Differential change in temperature (K)
E	Energy (J)
exp	Exponential
g	Acceleration due to gravity (m/s^2)
h_{pr}	Low heating value of the fuel
k	Depth (m)
k	Thousand
K-ε	Turbulent model
K-ω	Turbulent model
L	One pitch length
$\dot{m}$	Mass flow rate (kg/s)
Nu	Nusselt number
P	Pressure (Pa)

q	Dynamic pressure (Pa)
Q	Heat transfer (J)
R	Gas constant (J/kg K)
R	Range (m)
Re	Reynolds number
s	Blade pitch or spacing (m)
S	Entropy (J/kg K)
T	Temperature (K)
T-S	Temperature – Entropy
T-S	Tollmien - Schlichting
Tu	Freestream turbulence level (%)
U	Velocity (m/s)
W	Work (J)
W	Weight (N)
y	pitch direction

Greek

Symbol	**Definition**
Δ	Change
∂	Partial derivative
γ	Ratio of specific heats
γ	Average total pressure loss coefficient
η	Efficiency
μ	Viscosity (kg/m s)
π	Turbine stage total pressure ratio
ρ	Density (kg/m^3)

τ	Turbine stage total temperature ratio
ω	Local total pressure loss coefficient

Subscripts

Symbol	Definition
0-9	Engine station numbering
0	Total, stagnation, overall
c	Compressor
D	Drag
L	Lift
R	Relative to the rotor
s	Static
t	Total
t	Turbine

Superscripts

Symbol	Definition
$\bar{}$	Time-Average, mean value

Abbreviations

Symbol	Definition
2-D	Two-dimensional
3-D	Three-dimensional
A/D	Analog to Digital
AFRL	Air Force Research Laboratory
ASC	Aeronautical Systems Center
ASME	American Society of Mechanical Engineers

CFD	Computational fluid dynamics
DES	Detached eddy simulation
GH1R	Global Hawk first rotor
LEBU	Large-eddy break-up
LES	Large eddy simulation
LPT	Low pressure turbine
MEMS	Micro-electromechanical systems
MSRC	Major Shared Resource Center
NASA	National Aeronautics and Space Administration
PC	Personal computer
RANS	Reynolds Averaged Navier Stokes
TSFC	Thrust Specific Fuel Consumption
UAV	Unmanned aerial vehicles
USAF	United States Air Force
VBI	Vane blade interaction
VGD	Vortex generator device
VGJ	Vortex generator jet

CHARACTERIZATION OF THE GLOBAL HAWK LOW PRESSURE TURBINE FIRST ROTOR

CHAPTER 1. INTRODUCTION

1.1 Background

Unmanned aerial vehicles have achieved worldwide acclaim with their successful employment in recent operations over both Afghanistan and Iraq. The combat capability provided to military commanders has proven itself indispensable; thereby spurring the aerospace community to continue investment into this technology. UAVs were initially designed as Intelligence, Surveillance, and Reconnaissance (ISR) gathering platforms, which carry an array of cameras, sensors, and communications equipment (fas.org). Recent United States military operations have uncovered another face of warfare and are best represented by the global war on terror. Commanders are now faced with reclusive enemies using unconventional tactics that inherently requires leading edge combat capabilities. As a result, the UAV's mission is expanding to include direct combat missions with UAVs capable of autonomous target acquisition and attack. Military acquisition of UAVs began in 1964, and three programs have been successfully funded through full production (fas.org). The three successful UAV programs, Hunter, Predator, and Global Hawk, were designed to fulfill surveillance requirements at close range (50 km), short range (200 km) and endurance loitering (beyond 200 km) (fas.org). The Hunter, Predator and Global Hawk UAVs listed above are shown in Figures 1 through 3

respectively and are provided by the Federation of American Scientists through their website (www.fas.org).

Figure 1. Hunter short range UAV

Figure 2. Predator medium range UAV

Figure 3. RQ-4 Global Hawk long range UAV

Lt Jeff Mustin, in an article about the future development, tactics, and applications of UAVs stated that battle damage assessment is far too hazardous for manned assets but perfect for UAVs. The adventuresome undertaking of collecting signals intelligence on surface-to-air missile (SAM) sites is also well suited for unmanned assets [1].

The range and endurance of UAVs such as the RQ-4 Global Hawk, shown in Figure 3, are limited by the low-pressure turbine (LPT) efficiency at high altitude and low flight speed. This problem is seen in the Global Hawk program where the on-design flight conditions are a standard cruise velocity of Mach 0.6 at an altitude of 65,000 ft [2]. These flight conditions can result in LPT blade operating at inlet axial chord Reynolds number below 25k. Low Reynolds numbers experienced by LPT blades are known to cause losses in efficiency and loading. The immediate impact of this extremely low Reynolds number is the development of laminar boundary layers over the turbine blades. The combined effect of the laminar flow and large turning angles associated with LPT blades results in flow separation over a substantial section of the blade suction surface [8]. The loss in efficiency due to the boundary layer separation places restrictions on the aircraft range, altitude and electrical power extracted from the engine. A solution must be reached that will help delay separation at low Reynolds numbers, but not adversely affect blade efficiency at higher Reynolds numbers.

1.2 Current Research Objectives

Comprehensive research has been accomplished through the Air Force Research Laboratory (AFRL) in the area of boundary layer separation control as a feasible solution to this problem [2; 3; 4]. In addition to both refining and modernizing the drawdown wind tunnel facility operated by the turbine branch of AFRL, this study has characterized the performance of the first rotor of the Global Hawk's low pressure turbine through

extensive development of total pressure loss, wake velocity, and boundary layer velocity profiles. This information was compared with previous in-house studies performed on the Pak-B blade. The comparison was performed to extract potential performance gains realized through the application of high turning angle blades as well as to quantify potential operating conditions (Reynolds numbers) most likely to cause flow separation over the Global Hawk's current LPT blade. Furthermore, the pressure loss and velocity profile data gathered during this current experimental investigation utilizing the Pak-B blade was compared with its respective data generated through previous studies by Lake, Rouser and Casey [2,3,4] to ensure data integrity as extensive hardware and instrumentation modifications have been completed.

1.3 Chapter Summary

Due to the success of UAVs in recent military operations, those vehicles have permanently secured their place above the battlefield in the eyes of many theorists [1]. Therefore, the development, sustainment and procurement of current and future UAV platforms are of increasing importance to the war fighter. Sustainment, in particular, is of utmost importance to today's military forces because it by definition impacts UAVs currently available. As mentioned previously, the Global Hawk is the sole long range UAV in the Air Force inventory now, and current deficiencies must be immediately addressed to prevent the loss of military capability. The Global Hawk has been routinely operated at flight conditions that result in significant deviation from the design point of the LPT. The requirements to operate at these conditions have driven numerous studies directed to mitigate the issues that arise, namely the separation of the flow around the LPT airfoils. Briefly, studies have included the following: inclusion of high turning angle blades, passive control such as blade surface geometries and active control such as vortex jet generators. This study will pursue a solution to this issue through aerodynamic

characterization of a blade whose geometry was derived from the first stage rotor of the Global Hawk's LPT.

CHAPTER 2. BACKGROUND AND THEORY

Historically, turbomachinery design has been focused on developing compressors for maximum pressure ratio and high-pressure turbines to sustain maximum temperatures. Low pressure turbines (LPT) have continually been a focus of industry, laboratories and universities in a quest to improve the efficiency and performance of the gas turbine. This research on the LPT is intended to optimize aerodynamic characteristics and maximize loading and efficiency. One particular application is to further the capabilities of high altitude reconnaissance UAVs by enabling efficient operation of LPTs at low Reynolds numbers. The environment of the LPT offers both advantages and challenges to aerodynamicists when compared to the high pressure turbine (HPT). Because of its relative distance from the combustion chamber and upstream flow energy extraction by the HPT, the LPT operates with lower heat flux requirements. However, fluid flow, represented non-dimensionally by the Reynolds number, can experience ranges between 10,000 and 250,000 dependent upon operating conditions. The lower Reynolds numbers present a particular challenge to the aerodynamicist manifested through increased likelihood of fluid separation over the LPT airfoils. The separation is induced through several mechanisms. First, a major portion of the boundary layer, particularly along the suction surface, is laminar, especially at low Reynolds numbers. This flow regime can only withstand minor adverse pressure gradients before yielding to flow separation. Adverse pressure gradients are such that the pressure force tends to decelerate the fluid. Contrarily, turbulent boundary layers can withstand higher adverse pressure gradients due to the increased momentum transfer from the freestream through the boundary layer which tends to pull the flow toward the airfoil. The combination of low Reynolds numbers and adverse pressure gradients tend

to make the LPT airfoils susceptible to separation and increases the complexity of the boundary layer. Secondly, the periodic unsteady nature of the incoming flow associated with wakes substantially influences the boundary layer development including the onset and extent of the laminar separation and its turbulent re-attachment [4; 5]. As previously noted, the environment in the vicinity of the LPT is intrinsically unsteady. It is common for the blades to shed wakes periodically. These wakes, in turn, travel downstream and pass over the blades in the next row. Inside the wake is a region of high local freestream turbulence. Halstead et al. [6; 7] conclude the turbulence intensity can reach as high as 20%. The momentary high turbulence levels suppress boundary layer separation although this effect is only temporary. The laminar flow existing between shedding cycles is vulnerable to flow separation due to the low turbulence intensity [2].

2.1 Low Pressure Turbine Boundary Layer Aerodynamics

The flow fields about LPT blades are unsteady and transitional. Freestream turbulence levels exist between 1% and 20% [6; 7]. Halstead et al. [6; 7] documented the presence of passing wakes, centrifugal effects and vortices. The boundary layers on LPT blades operating at low Reynolds numbers gradually transition from laminar to turbulent over the suction surface of the blade as shown experimentally by Werle [8], Mayle [9], and Addison and Hodson [10]. The process of boundary layer transition is nearly steady, yet, intermittently affected by time-dependent wakes traveling downstream due to the relative motion of rotor and stator. As the wake travels downstream, the region on the blade affected by the wake quickly shifts from transitional flow to turbulent flow and then returns to transitional flow after the wake has passed [6].

There is a desire to determine the location of transition and the length of blade surface under transition to correlate transition duration to performance losses. This is a difficult task considering the many factors that influence the transitional modes. The

primary factors that affect transition are Reynolds number, freestream turbulence, and pressure gradients as shown in experiments by Mayle [9] and Walker [11]. Walker [11] also showed the three fundamental transition modes are: natural transition, bypass transition, and separation bubble transition.

The three primary transition modes exist under varying conditions. Natural transition is characterized by low freestream turbulence and no adverse pressure gradients. 2-D Tollmien-Schlichting (T-S) waves begin the process. As these T-S waves become unstable, they create 3-D loop vortices and large fluctuations [9]. The 3-D structures coalesce into turbulent spots. The turbulent spots grow as they move downstream. Eventually, the turbulent spots grow large enough to consume the entire boundary layer. Walker [11] dictated the end of the natural transition process occurs once the boundary layer becomes fully turbulent.

Flows consisting of higher levels of freestream turbulence can experience bypass transition. Freestream turbulence levels must be on the order of 20% in this case. The high turbulence environment allows for the manifestation of turbulent spots in the absence of 2-D Tollmien-Schlichting waves. Walker [11] found that linear stability theory could still be used to predict disturbances in this transition mode, helping predict the length of the transitional flow.

Laminar flow in the presence of adverse pressure gradients may produce a separation bubble. In this case, transition occurs in the shear layer between the separation bubble and the freestream. The investigations by Mayle [9], in addition to Qiu and Simon [18], verified re-attachment to the blade surface is catalyzed by the separated flow becoming fully turbulent. The Pak-B blade operating at low Reynolds numbers experiences laminar to turbulent transition due to the formation of a separation bubble.

2.2 GH1R Design Point

Information has been presented above to detail the complications of low Reynolds number flow through the LPT. The following data, Tables 1 and 2, were provided by Allison and show the relevant state points of both the design point and a common off-design point for the first stage rotor of the Global Hawk.

Table 1. Operating point comparison

	Design Point	**Global Hawk Off Design Flight Condition**
Condition	Max Cruise	High Cruise
Altitude (ft)	30,000	65,000
Mach #	Mach 0.70	Mach 0.60
Temp (deg R)	412	390
RPM	7682.1	7915.3

Table 2. Global Hawk low pressure turbine 1st rotor meanline conditions for off-design flight condition

State	**Off-Design Point**
Mach Number	0.391
Temperature Inlet (°R)	2104.4
Temperature Outlet (°R)	1998.8
Total Temperature (°R)	524.07
Pressure Inlet (psi)	4.26
Pressure Outlet (psi)	3.31
Ratio of Specific Heats	1.306
Blade Length (in)	1.074

Given the data above, Table 2, and assuming that the fluid behaves as an ideal gas and undergoes an isentropic process, the Reynolds number for both operating conditions can be obtained. Velocity was determined from the Mach number, specific gas constant

and the local static temperature as shown in equation 1. The characteristic length was taken to be the rotor length defined in the Table 2.

$$u = M \cdot \sqrt{\gamma \cdot R_{air} \cdot T_{ST}} \tag{1}$$

The viscosity was calculated by applying equation 2 considering that Sutherland's constant was 120 and the reference viscosity (μ_o) was 0.01827 centipoise at the reference temperature.

$$\mu = \mu_o \cdot \frac{0.55 \cdot T_o + C}{0.55 \cdot T_{ST} + C} \cdot \left(\frac{T_{ST}}{T_o} \right)^{\frac{3}{2}} \tag{2}$$

Finally, the familiar definition of Reynolds number shown in equation 3 was invoked.

$$Re = \frac{\rho \cdot u \cdot c}{\mu} \tag{3}$$

The Reynolds numbers for the off design point was 13,150. The reader should notice the significant difference between flow conditions in the LPT and that preventing flow separation may prevent a significant challenge for the rationale mentioned earlier in this chapter.

2.3 Determination of LPT Performance Improvements

A reasonable measure of aircraft engine performance is range capability. As seen in the Breguet range formula, aircraft cruise range is directly proportional to thrust specific fuel consumption (TSFC):

$$\frac{W_{final}}{W_{initial}} = \exp\left(-\frac{C_D}{C_L}\frac{TSFC * R}{U} g \right) \tag{4}$$

where U is the flight velocity, g is the acceleration due to gravity, CD is the aircraft drag coefficient, C_L is the aircraft lift coefficient, R is the range, W_{final} is aircraft final weight, and $W_{initial}$ is initial aircraft weight [12]. Rearranging Eq. 4 to solve for the range, it is clear that for a given aircraft, at similar flight conditions, minimizing TSFC results in maximizing the range:

$$R = -\frac{C_L}{C_D}\ln\left(\frac{W_{final}}{W_{initial}}\right)\frac{U}{TSFC}\frac{1}{g} \tag{5}$$

The TSFC is given by:

$$TSFC = \frac{U}{\eta_o h_{pr}} \tag{6}$$

where η_o represents the overall engine efficiency and h_{pr} is low heating value of the fuel [12]. Therefore, increasing the overall engine efficiency decreases the TSFC. Over time, these improvements could save enormous amounts of money as well as improve the aircraft mission effectiveness.

A T-S diagram illustrates overall engine efficiency, where T is temperature and S is entropy. A relation for the Brayton cycle representing the ideal jet engine and a T-S diagram is shown in Fig. 2 [12]. The temperature increases across the compressor isentropically as illustrated from stations 2 to 3:

$$p = const * T^{Cp/R} \tag{7}$$

where p is pressure, T is temperature, C_p is the average ratio of specific heats at constant pressure, and R is the gas constant [13]. The ideal Brayton cycle does not account for losses or entropy production across the compressor. From station 3 to 4, fuel is injected into the combustor causing an increase in temperature. Convention for an ideal engine assumes that this process occurs at constant pressure. The hot air expands through the ideal turbine and nozzle isentropically (stations 4 to 9). This results in a drop in both pressure and temperature.

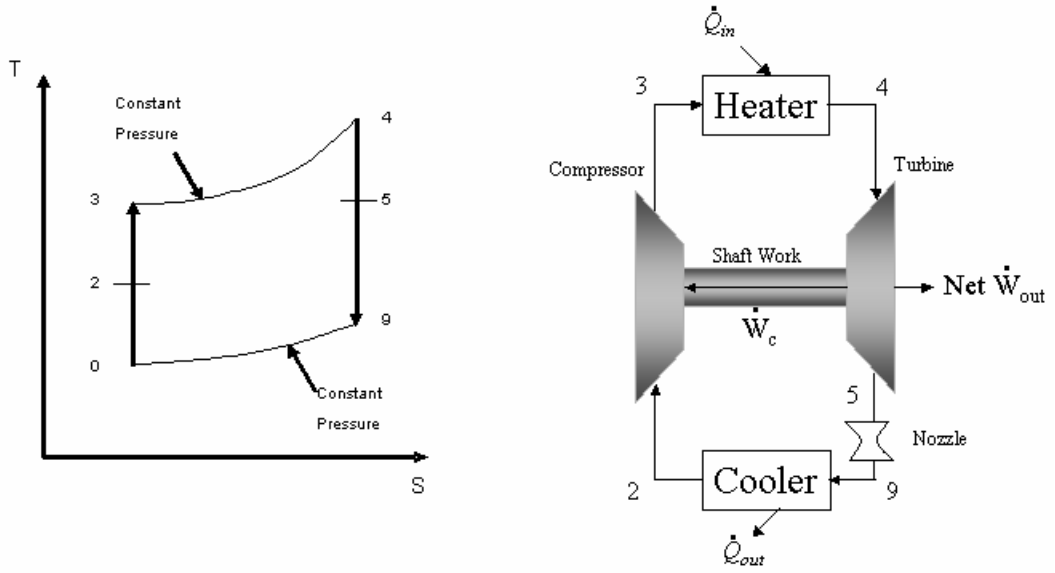

Figure 2. Brayton cycle and ideal gas turbine engine [12]

The first law of thermodynamics for a closed system is:

$$\Delta E = Q - W \tag{8}$$

where ΔE is the net energy, Q represents the net heat and W is the net work transferred through the system [13]. Given a calorically perfect gas, the analysis of the ideal Brayton cycle yields the following equations for the compressor and turbine, respectively:

$$\dot{W}_c = \dot{m}\ c_p\ (T_{t3} - T_{t2}) \tag{9}$$

$$\dot{W}_t = \dot{m}\ c_p\ (T_{t4} - T_{t5}) \tag{10}$$

where $\dot{m}$ is mass flow rate, c_p is the average specific heat at constant pressure and T_t is total temperature at the relevant position [12]. The work required by the compressor is supplied by the turbine such that $\dot{W}_c = \dot{W}_t$ for the ideal engine. Naturally, a real turbine engine cycle is less than ideal and also experiences some off design conditions. The losses associated with the turbine engine occur in many ways. One is flow separation. Flow separation is a major factor driving the overall turbine efficiency.

A T-S diagram can illustrate the non-ideal behavior of the turbine engine. Figure 3 depicts a T-S diagram for a single, non-ideal turbine stage. Entropy is generated and total pressure decreases over the stator at constant total temperature. Further, the entropy increases over the rotor. This is accompanied by a decrease in total pressure and total temperature.

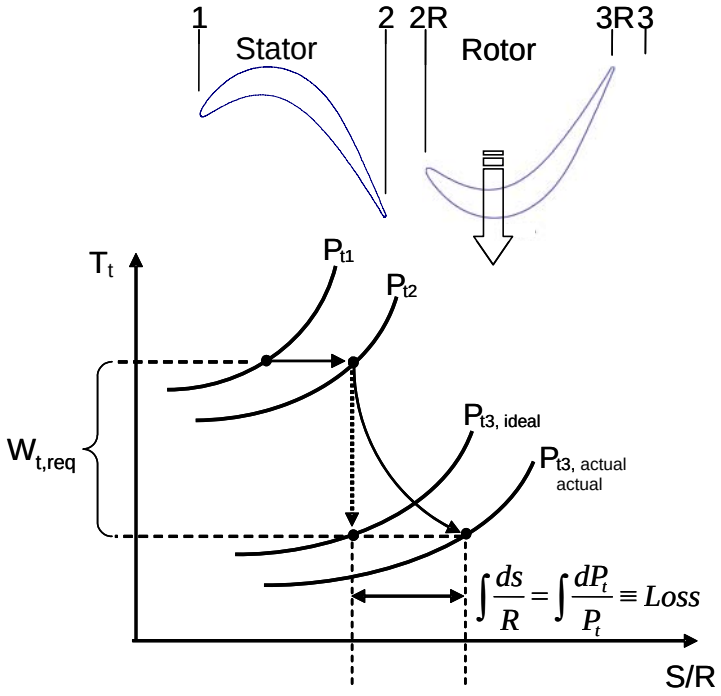

Figure 3. T-S diagram for a non-ideal turbine stage

Gibbs equation relates the change in entropy to the change in temperature and pressure:

$$ds = c_p \frac{dT_t}{T_t} - R \frac{dP_t}{P_t} \tag{11}$$

where ds is the change in entropy, R is the gas constant, T_t is total temperature, dT_t is the change in total temperature, P_t is total pressure and dP_t is the change in total pressure [Moran, 13]. As shown in Figure 3, total temperature is constant across the stator, and Eq. 11 reduces to the following:

$$ds = -R \frac{dP_t}{P_t} \tag{12}$$

Equation 12 shows the relationship between pressure drop and entropy production. Therefore, there must also be a relationship between pressure loss through a stage and stage efficiency. Mattingly [12: 358] correlates turbine stage efficiency and pressure drop in the following expression:

$$\eta_t = \frac{1 - \tau_t}{1 - \pi_t^{\gamma_t - 1 / \gamma_t}} \tag{13}$$

where γ_t is the ratio of specific heats in the turbine, $\tau_t = T_{t3}/T_{t1}$ and $\pi_t = P_{t3}/P_{t1}$. The consequence of a decrease in exit total pressure for a fixed total temperature ratio is a reduction in efficiency. Therefore, there is a direct relationship between turbine performance and exit total pressure. Exit total pressure is a measurable quantity within the linear cascade and can lead to conclusions on turbine efficiency. The equation below shows the total pressure loss coefficient:

$$\omega = \frac{P_{t,inlet} - P_{t,exit}}{q_{inlet}} \tag{14}$$

where ω is defined as the loss coefficient based on inlet dynamic pressure (q_{inlet}). Equation 14 shows that as the exit total pressure decreases the loss coefficients increase. Eliminating the separated flow would result in higher exit total pressures and correspondingly lower losses. Lake [2] theorized the effect of an improved exit total pressure in Fig. 4. The baseline plot represents a turbine without any surface modifications. Notice that a small improvement in exit total pressure (possibly by implementing boundary layer control) results in a significant decrease in entropy generation.

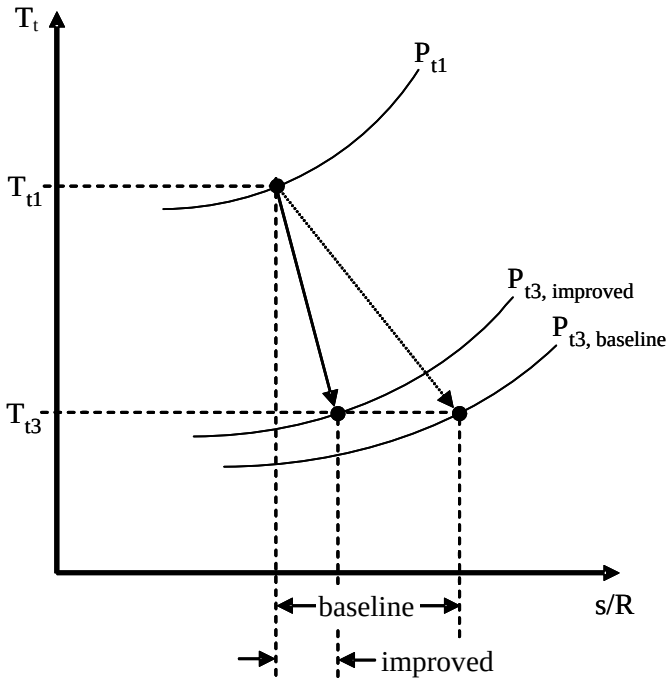

Figure 4. T-S diagram illustrating possible improvement with higher turbine exit total pressure [1]

Lake [1] assumed $\gamma_t = 1.3$, $\tau_t = 0.84$, $P_{t1} = 1731.6$ kPa, $P_{t2R} = 1043.0$ kPa, $T_3 = 1505.5$ K, $T_{t3R} = 1664.4$ K, $T_{t3} = 1560.0$K, and the stage loss coefficient, $\omega_{loss} = 0.15$. Applying these values to Eq. 15 returns a value of $P_{t3} = 748.1$ kPa:

$$P_{t3} = \frac{P_{t2R}}{1+\omega_{loss}\left[1-\left(\frac{T_3}{T_{t3R}}\right)^{\gamma_t/\gamma_t-1}\right]}\left(\frac{T_{t3}}{T_{t3R}}\right)^{\gamma_t/\gamma_t-1} \tag{15}$$

where γ_t is the ratio of specific heats at the turbine. Entering these values into Eq. 13 returns a stage efficiency of 0.9087. Lake [2] then showed that a 10% reduction in stage loss coefficient returns a 0.5% increase in stage efficiency.

Through his investigation, Lake [2] determined that dimples on the surface of a Pak-B blade reduced the loss coefficient. Rouser [8] showed in his research that a dimple at 65% of the axial chord had the greatest effect on reducing the loss coefficient. The current research further investigates the use of dimples at 65% of the axial chord varying the span-wise dimple spacing and incorporating an additional row at 76% of the axial chord for the reduction of losses. This is one more step towards optimizing the use of dimples as passive flow controllers on a low-pressure turbine blade.

2.4 Active and Passive Boundary Layer Control

In an attempt to study and improve LPT efficiency at low Reynolds number conditions, Pratt and Whitney developed the Pak-B blade. The commercially used Pratt and Whitney Pak airfoil was the foundation for the two-dimensional (2-D) Pak-B shape. Extruding the Pak-B shape in the span-wise direction yields a blade that can be used for local three-dimensional (3-D) analysis. This blade does not truly represent a 3-D blade since it neglects taper and twist [8].

Lake's [2] investigation involved testing various passive control techniques on a Pak-B blade. Ultimately, Lake [2] concluded that recessed dimples prevent separation if positioned just forward of the natural chord-wise separation location. He reported for an operating Reynolds number of 45,000 and freestream turbulence of 4% that losses were reduced as much as 51.7% [2]. Lake [2] inferred that the dimples energized the flow and forced the laminar boundary layer to transition to turbulence prior to separation thereby acting similar to vortex generators.

Recessed dimples possess great potential for reducing low Reynolds number losses without dramatically affecting higher Reynolds number efficiencies [8]. Moreover, these passive controls do not require a dramatic engine redesign. They do not carry with them any additional weight penalty nor require additional power from the engine. Most important, they can be easily retrofitted into existing engine hardware. It is important, however, that flow mechanisms produced by these passive controls be very well understood to assist in the exact size and placement of the dimples for an optimal engine design.

Casey's [14] research investigated several dimple patterns for suppression of boundary layer separation on the Pak-B low pressure turbine blade. He found that all the various patterns performed the same, so the dimples placed at 65% of the axial chord with 4.44 cm center-on-center spacing is the easiest to manufacture and is therefore the pattern of choice.

Previous experiments involving Reynolds numbers less than 200k have increased the understanding of the transitional boundary layers around LPT blades at low Reynolds numbers. Many of these experimentalists utilized linear cascades to help with their

research. Rivir [15] used a Langston airfoil to examine turbulent length scale effects on transition locations. Sharma et al. [16] discovered the loss coefficient nearly tripled as the Reynolds number was brought below 95k as compared to higher Reynolds numbers. Murawski et al. [17] and Qiu and Simon [18] have shown that flow separation from a Pak-B blade at low Reynolds numbers deteriorates the LPT performance, and have documented velocities, surface pressures, separation locations and boundary layer thicknesses. Murawski et al. [17] reported separation from 75% to 90% of the axial chord at inlet axial chord Reynolds numbers as low as 53k. Further, Qui and Simon [18] confirmed turbulent reattachment occurs aft the 90% axial chord location. Simon and Volino [19] have reported the efficiency losses of the Pak-B profile operating at conditions similar to those seen by high altitude UAVs. Hourmouziadis [20] also experimented with low Reynolds numbers and documented a reduction in efficiency and a dramatic increase in profile losses.

Much of the above research laid a firm foundation for Lake [2] to quantify the losses associated with flow separation at low Reynolds numbers for the Pak-B profile. Lake [2] confirmed an increase in the total pressure loss coefficient and wake momentum deficit related to the separated flow. He resolved that a natural chord-wise separation location exists at about 70% of the axial chord on a Pak-B blade at an inlet axial chord Reynolds number of 45k and sought to control the separated-flow transition and laminar separation on a Pak-B blade [2]. Lake [2] experimented with trip wires, span-wise V-grooves and recessed dimples. He documented a reduction of the losses associated with separated flow due to the successful integration of surface modifications [Lake, 2]. Lake [2] concluded that, of the techniques he explored, dimples had the greatest potential in

effectively eliminating losses associated with low Reynolds numbers. Lake's work provided a detailed understanding of LPT performance at low Reynolds operating conditions.

Rouser [8] furthered Lake's work by investigating full dimples as well as stream-wise half-dimples at 50%, 55%, and 65% axial chord locations and extended the research to an operating Reynolds number of 25k. Rouser [8] concluded that for an inlet axial chord Reynolds number of 25k full dimples placed at 65% of the axial chord reduced separation losses by as much as 28%. He also developed computational models of the Pak-B blade with full and half-dimples at 60% of the axial chord, in addition to a grid representing a Pak-B blade without any surface modifications.

Casey [14] investigated several dimple patterns for suppression of boundary layer separation on the Pak-B low pressure turbine blade. Dimples placed at 65% of the axial chord with 2.22 cm and 4.44 cm center-on-center spacing and a multiple row case featuring dimples at 65% and 76% of the axial chord spaced 4.44 cm center-on-center were the cases investigated. The dimples in the multiple row case were arranged in a chevron pattern such that the center of an upstream dimple aligned with the midpoint between two downstream dimples. The unmodified blade was also tested for comparison.

2.5 Chapter Summary

The current research afforded numerous challenges in data collection and analysis. The problem posed involved determining improvements in overall turbine efficiency due to surface modifications in unsteady, transitional flow. With all turbine efficiency

explorations, the effect of even the most modest improvement in engine efficiency could result in radical improvements in range, service ceiling, endurance, and extracted engine power to operate onboard systems. As a result, the experimental efforts focused on obtaining any data that may correlate to turbine efficiency. Within the confines of the linear cascade, velocity and pressure measurements were the most readily available parameters. These elements were used to develop loss coefficients that were helpful in comparing efficiencies.

This investigation was specifically geared to improving the turbine efficiency of high altitude reconnaissance aircraft. The operating Reynolds number experienced by the LPT for these missions falls as low as 13k. The suction surface boundary layer is known to separate under these conditions. It is believed that reducing the separated region may dramatically improve turbine efficiency. Pressure and velocity measurements made in the downstream wake of the blades provided a macroscopic view of the separation effect.

CHAPTER 3. METHODOLOGY

Turbine aerodynamics is often studied with linear cascade tunnels. Two-dimensional effects can be studied using linear cascades, as the blades are not rotating, and the flow is nearly uniform in the span-wise direction as it enters the test section [Rouser, 8]. A linear cascade consists of several blades lined-up in a row simulating the turning angle experienced in the low-pressure turbine. The following presents a detailed discussion of the linear cascade tunnel used in the current research.

A modified open loop Aerolab Corporation wind tunnel has been configured for low-speed linear turbine cascade testing. The tunnel is operated by the AFRL turbine technology branch, and is shown in Figure 5. For this study, an 8-blade 8-passage linear turbine cascade was used to simulate flow through a low-pressure turbine. Blade 5 in the linear cascade was the blade of interest for characterization and comparison purposes. The blade was chosen primarily due to its central location within the linear cascade and relative distance from the periphery of the test section, minimizing edge effects. The study was conducted using two measurement techniques; wake velocity traverses and wake pressure traverses. Wake traverses were performed to ascertain the Reynolds numbers where losses are greatest, as well as the areas of the greatest change. Both velocity and pressure wake traverses were conducted for a Reynolds number sweep range of 10,000 to 100,000. Finally, boundary layer traverses were taken to map the development of the boundary layer on the suction side of a turbine blade.

3.1 Wind Tunnel and Cascade Characteristics

This drawdown tunnel, Figure 5, has been designed to allow for variable turning angles in the test section, which include inlet flow angle, outlet flow angle, and total turning angle. The tunnel and test section were slightly modified from that used by Lake [2], Rouser [8] and Casey [14]. Rouser [8] describes in detail the wind tunnel characteristics. A summary is provided here for convenience.

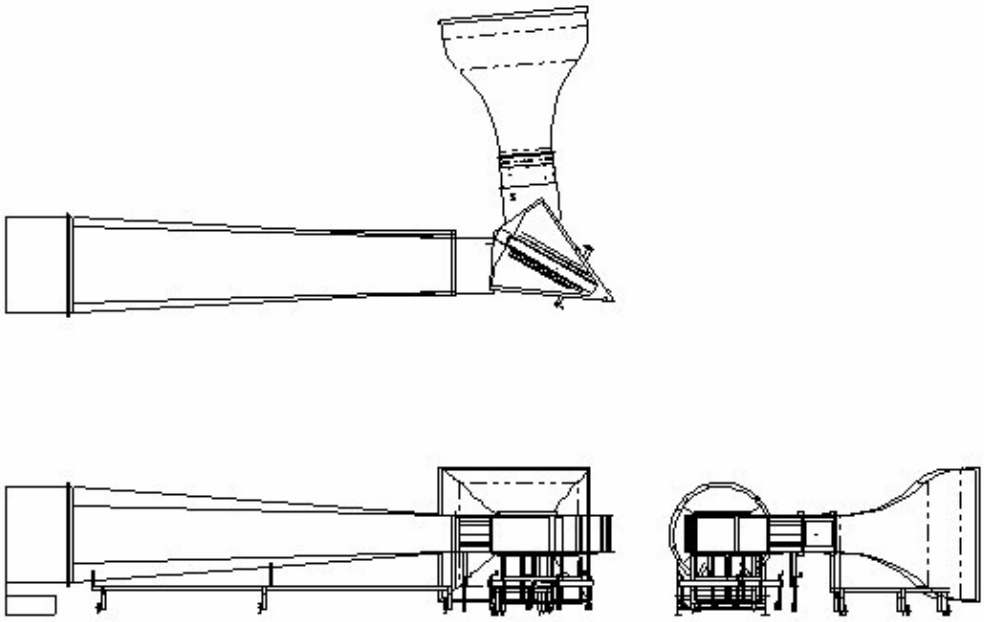

Figure 5. Aerolab Corporation modified drawdown wind tunnel

3.1.1 Wind Tunnel Geometry and Features

A Joy Technologies Axivane axial flow fan draws air through the wind tunnel. A Harmon/Commonwealth Corporation variable frequency motor controller fixes the motor RPM and adjusts the power input to maintain the motor speed. The motor speed determines the flow speed in the tunnel.

The inlet bell-mouth is 305 cm wide and 267 cm tall. A honeycomb flow straightener leads in to a convergent nozzle 229 cm long with exit dimensions 122 cm

wide by 85.1 cm tall. This is an area reduction of 87%. Styrofoam inserts, as displayed in Figure 6, help minimize corner vortices. The flow straightener and corner vortex suppression help obtain freestream turbulence levels less than 1% in the test section.

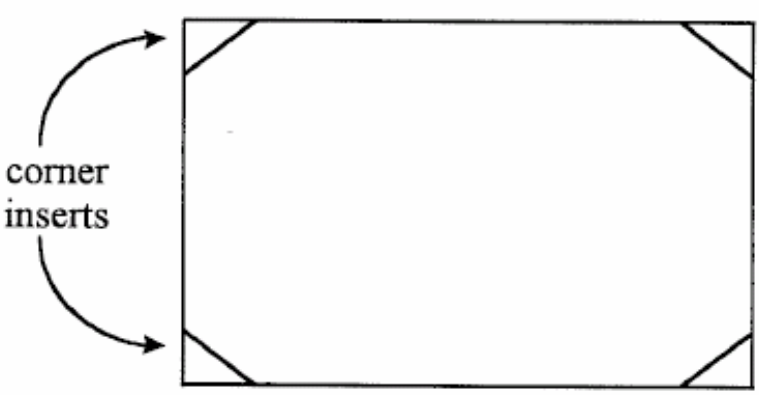

Figure 6. Cross-sectional area of wind tunnel

Just downstream of the nozzle and 190.7 cm upstream of blade #1 is a turbulence generation section. The tunnel can be run with the turbulence grid out yielding a clean configuration and less than 1% turbulence. A passive turbulence grid, Figure 7, can also be installed in this section yielding freestream turbulence levels of approximately 4% from 127 cm to 254 cm downstream of the turbulence grid. Isotropy and length scales were characterized by Lake [2].

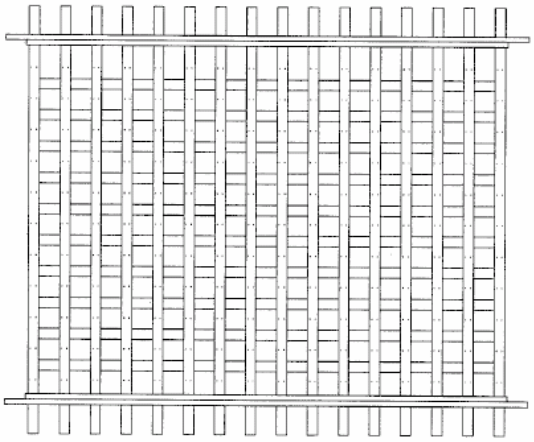

Figure 7. Passive Turbulence grid - generates approximately 4% Tu

The wind tunnel is capable of flow total turning angles up to 130^{o} with the adjustable test section. The central hinge pivot joint allows for inlet and outlet flow angles to be altered independently, once the total turning angle is set, as shown in Figure 8. These angles were set using geometry, a detailed discussion of how these angles are adjusted can be found in Appendix B.

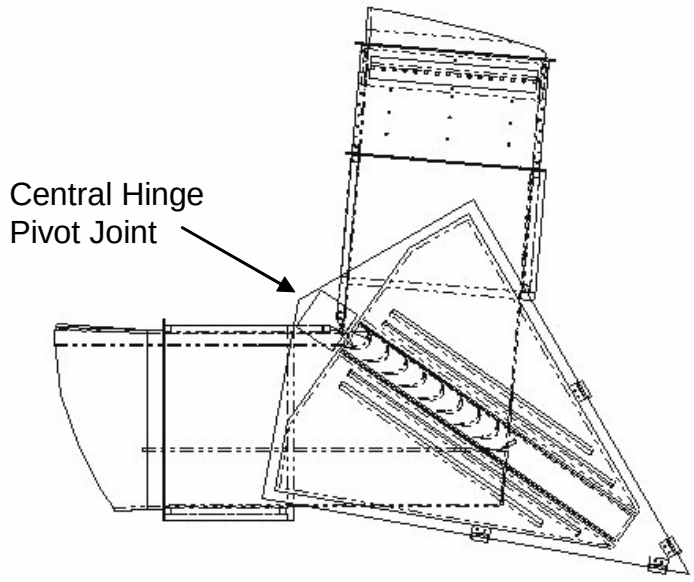

Figure 8. Plan view of test section

3.1.2 Test Section Characteristics

Figure 9 shows a cut away of the test section of the wind tunnel. The test section is constructed out of Plexiglas for optimal visibility and supported by steel struts. An outer tailboard guides the exhaust region to ensure a proper exit angle. The wind tunnel exhibits good uniformity and periodicity as demonstrated by Lake [2]. For the current research the tunnel was used as set by Lake [2], and used by Rouser [3] and Casey [14] in

order to validate the wind tunnel upgrades and then set to the design specifications for the GH1R. These settings for the GH1R, as well as the original settings for the Pak-B are summarized in Table 3. The innermost and outermost walls of the test section have been shaped to approximate the blade suction and pressure surfaces, respectively.

Table 3. Blade design specifications

	Pak-B	GH1R
Total Turning Angle	95	91.69
Inlet Flow Angle	35	30.75
Outlet Flow Angle	-60	-60.94

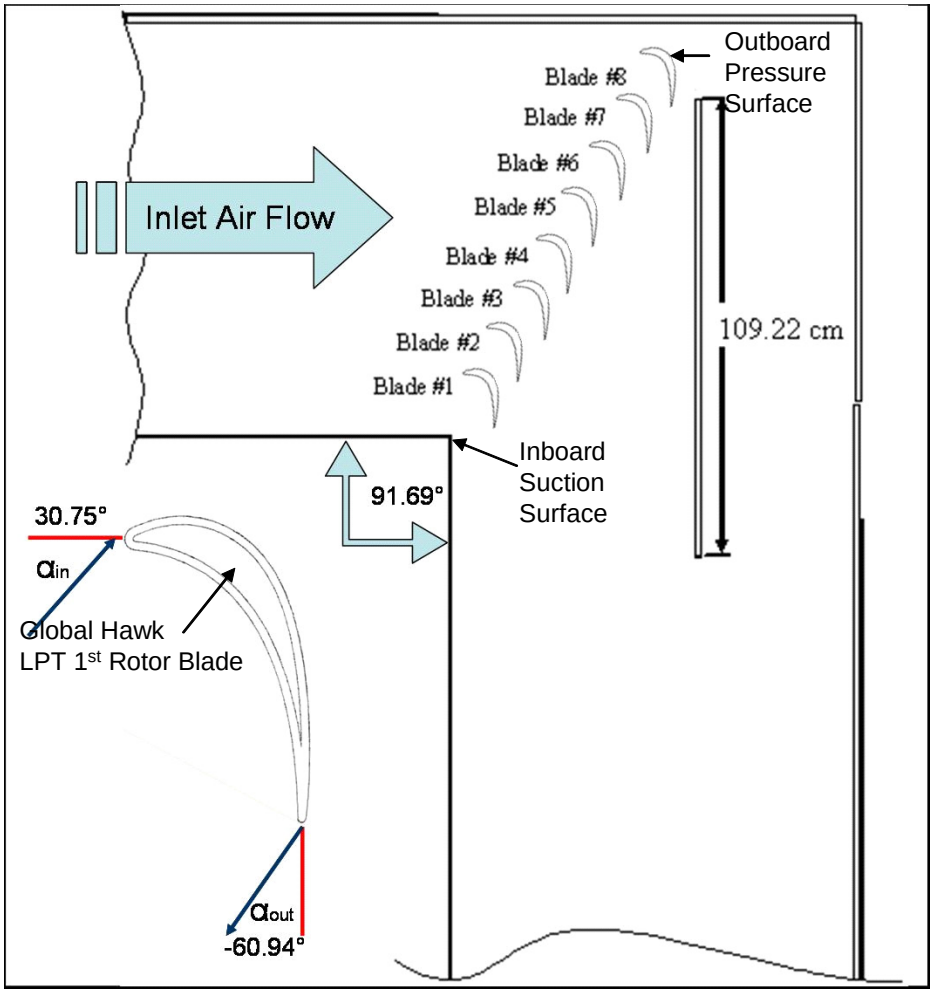

Figure 9. GH1R test section geometry

3.1.3 Cascade Features

The blade cassette, Figure 10, is fashioned from clear Plexiglas top and bottom plates to which the eight blades and outboard pressure surface blade are bolted. The two plates are supported by steel runners which assure it is flush with the tunnel surface. The two plates, eight blades, and outboard pressure surface form the cascade.

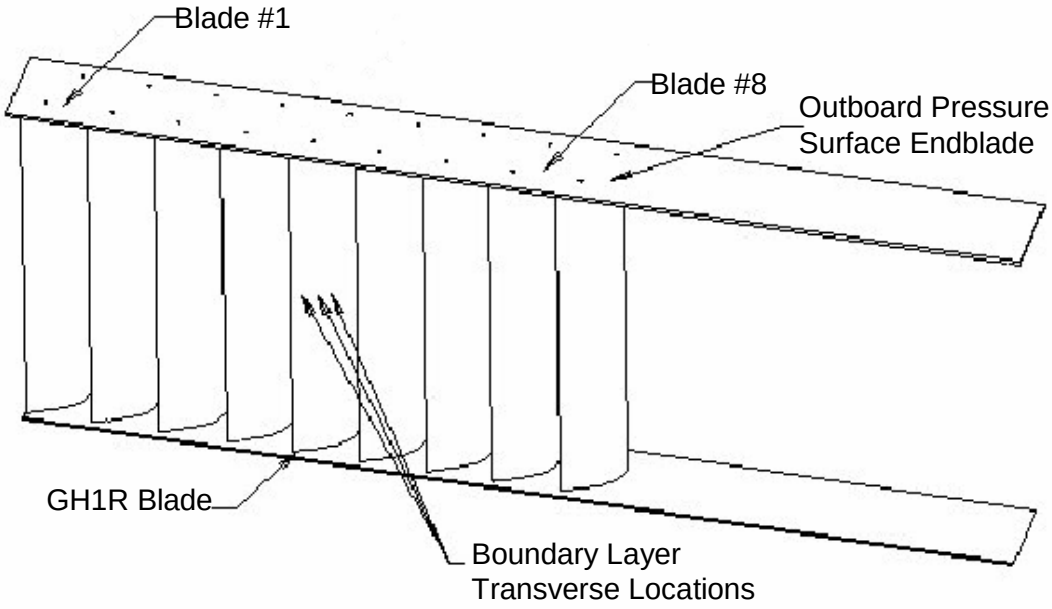

Figure 10. Removable cascade of eight Global Hawk first rotor blades and endblade

Two cascades were utilized for this series of testing. The first cascade was based on the Pack-B design and the second was based on the Global Hawk first rotor blade (GH1R). The current tunnel configuration is representative of the design specifications for the GH1R.

The eight GH1R blades in the linear cascade have an axial chord of 17.78 cm. Each blade has a true chord of 21.26 cm. The aspect ratio of 4.92 approximates a 2-D flowfield about the mid-span. The blade size and shape is arrived at by taking the cross

section at the mid diameter of the real Global Hawk low pressure turbine first rotor blade and using this as a form. This form is then enlarged using a scaling factor of 7.8; this new larger blade image is then used to extrude the test blades. The blades in the test section were molded from Ultralloy 108 white resin with a span of 78.63 cm.

Blade #1 is farthest inboard at 198 cm downstream of the turbulence grid. Blade #8 is farthest outboard at 300 cm downstream of the turbulence grid. The blade of interest is in the fifth position 218 cm downstream of the turbulence grid within the 4% turbulence intensity region.

3.2 Data Collection

A personal computer (PC) data acquisition system with integrated signal conditioning capability was configured to acquire fluid properties within the test section. Several parameters were monitored to characterize flow in and around the cascade blades. Most notably temperature, pressure and velocity measurements were collected. Figure 12 shows the location of these transducers.

Figure 11 illustrates the instrumentation system implemented in the current research to collect and process the data. The primary controller is a Dell Pentium 4 personal computer (PC). Installed in the PC is an MXI-3 fiber-optic interface board that is connected to a National Instruments PXI 1010 chassis. Three PCI cards are also contained in the Dell to drive the traverses and collect data from the hot-films.

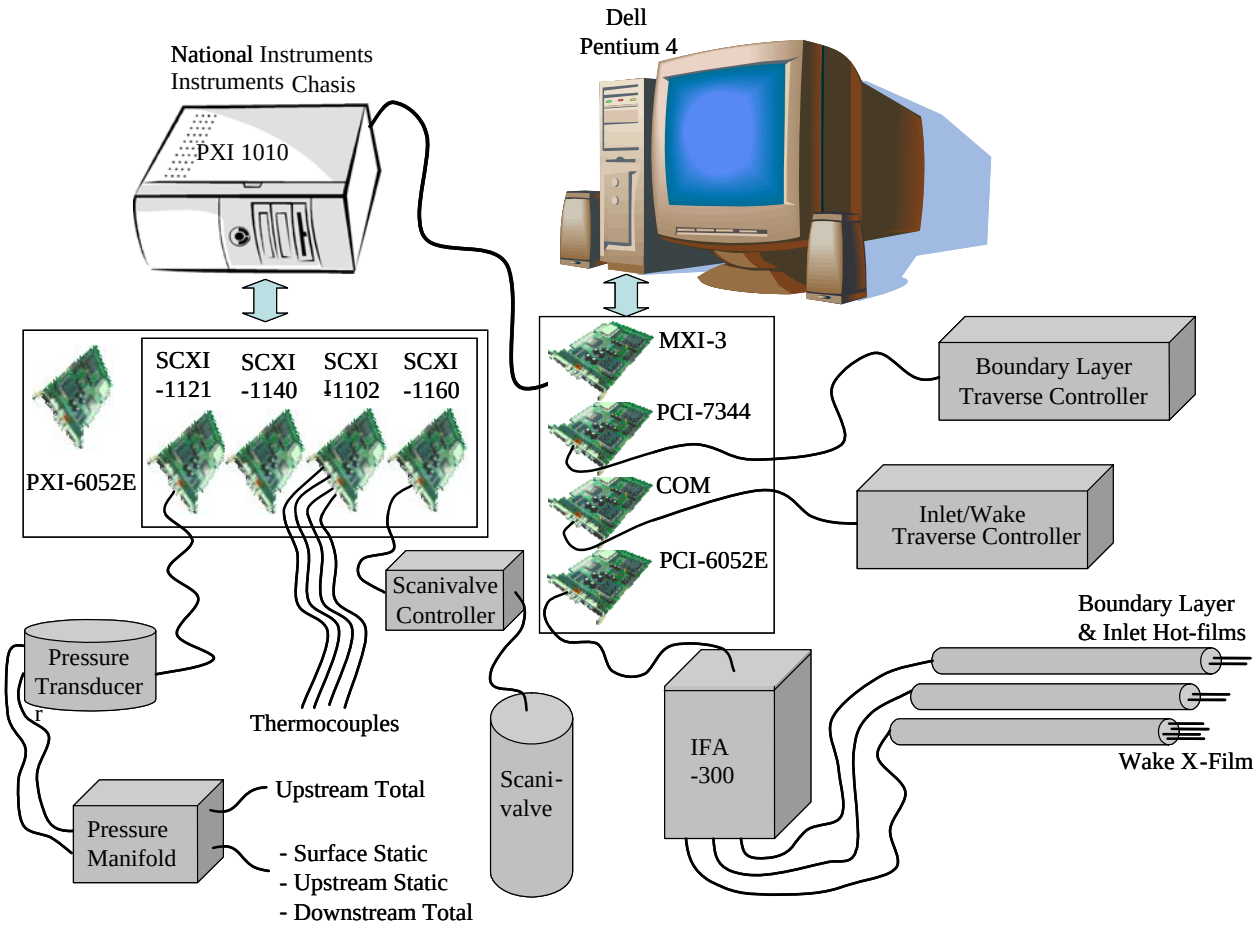

Figure 11. Instrumentation schematic

An IFA-300 receives a direct signal from the hot-film elements. The IFA-300 is set up using a calibration file each time it is used. This calibration file is created using a Labview VI. The single element hot-films utilize a non-dimensional curve fit between Nusselt and Reynolds numbers for calibration, as described by Bruun [21]. The heat transfer across the element is determined by balancing a Wheatstone bridge within the IFA-100. The Nusselt number is related to the heat transfer. The heat transfer is a function of velocity. A non-dimensional relationship is as follows:

$$\mathrm{Nu} = C + D\,(\mathrm{Re}^{0.45}) \tag{16}$$

where Nu is Nusselt number, *C* is the curve intercept on the Y-axis and *D* is the slope. The exponential value of 0.45 is chosen to provide an acceptable curve fit for measuring low speed flow [Rouser, 8]. Equation 16 yields a correlation between voltage and velocity. The calibration was performed using a TSI Model 1127 calibration stand and the Druck LPM 5481 pressure transducer. Detailed calibration procedures are outlined in Appendix C.

The main three axial Velmex traverse sits on top of the tunnel, and positions the downstream Kiel probe and hot-film, and the upstream pitot-static probe. This traverse is controlled through the PC via a standard RS 232 Com card. The power and control component for the main traverse is a Velmex V-9000 controller combined with a Sony LH61 digital position display accurate to $\pm$0.005. The TSI, Inc. IFA-300 Flow Analyzer sends the voltages returned from the hot-film and hot-film directly to the PC through a National Instruments PCI-6052E A/D card which has a 16 bit resolution and a 333 ks/s sampling rate per channel.

The boundary layer traverse, a National Aperture, Inc. motorized 5.08 cm MM-3M micro traverse, is controlled through the PCI-7344 card inside the PC. It has a movement resolution of 20157.4 steps per cm. The traverse position encoder provides a linear spatial resolution of $\pm 5.08 \times 10^{-5}$ cm. The traverse position is controlled and powered by a National Aperture, Inc. MC-4SA servo amplifier, which is in-turn connected to the PCI-7344 card.

A PXI-6052E A/D board with 16-bit resolution over $\pm$10 volts is contained within the PXI 1010 chassis. The A/D board is connected to an SCXI cluster. A thermocouple board designated SCXI-1102 is connected to the four thermocouples. Further, an SCXI-

1160 relay controller included in the SCXI cluster commands three Scanivalve controllers. The pressure transducer is a Druck LPM 5481 connected to an SCXI-1121 signal-conditioning card. The Druck's range is -0.2 to 0.8 in H_2O. It requires a 10-30 volt power supply and outputs 0-5 volts. One side of the pressure transducer always receives the inlet total pressure from the upstream pitot-static probe. The Scanivalve determine whether the input to the other side of the Druck is inlet static pressure, exit total pressure, or surface static pressure. The two inputs received allow for differential pressure readings.

The four thermocouples connect to the PXI 1010 chassis through the SCXI-1102. The SCXI-1102 is used as a signal conditioner, and connects to an SCXI-1303 thermocouple block. The SCXI-1303 uses a thermistor for a cold junction temperature reference. Differential measurements are made between thermocouples and the thermistor inside the SCXI-1303. Voltages are relayed through the PXI 1010 chassis to the A/D board in the PC. The computer then converts the voltages to temperatures.

3.3 Instrumentation

A series of thermocouples, pressure sensors and hot-films comprise the measurement devices used in the current research. Figure 12 illustrates the location of each of the measurement devices.

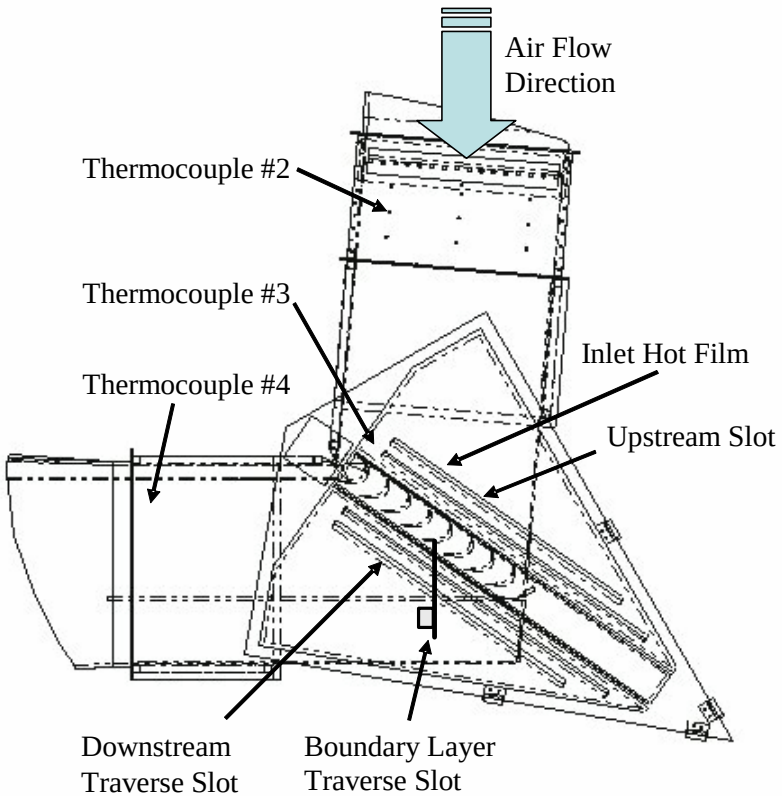

Figure 12. Wind tunnel instrumentation locations

There are three physical quantities measured in this research; temperature, velocity, and pressure. A series of thermocouples provide continuous accurate measurements of the flow temperature throughout the tunnel. Two hot-film probes are used to determine flow speeds at different points in the tunnel. An inlet hot-film is used to set the tunnel inlet flow speed and acts as a Reynolds number reference. Another hot-film inserted through a downstream traverse slot measures wake velocities. A pitot-static probe extends through an upstream slot to gather the inlet total and static pressures. A Kiel probe is supported through a downstream traverse slot to measure the downstream total pressure. Figure 13 demonstrates the resulting data from the four measurements taken during a three wake traverse.

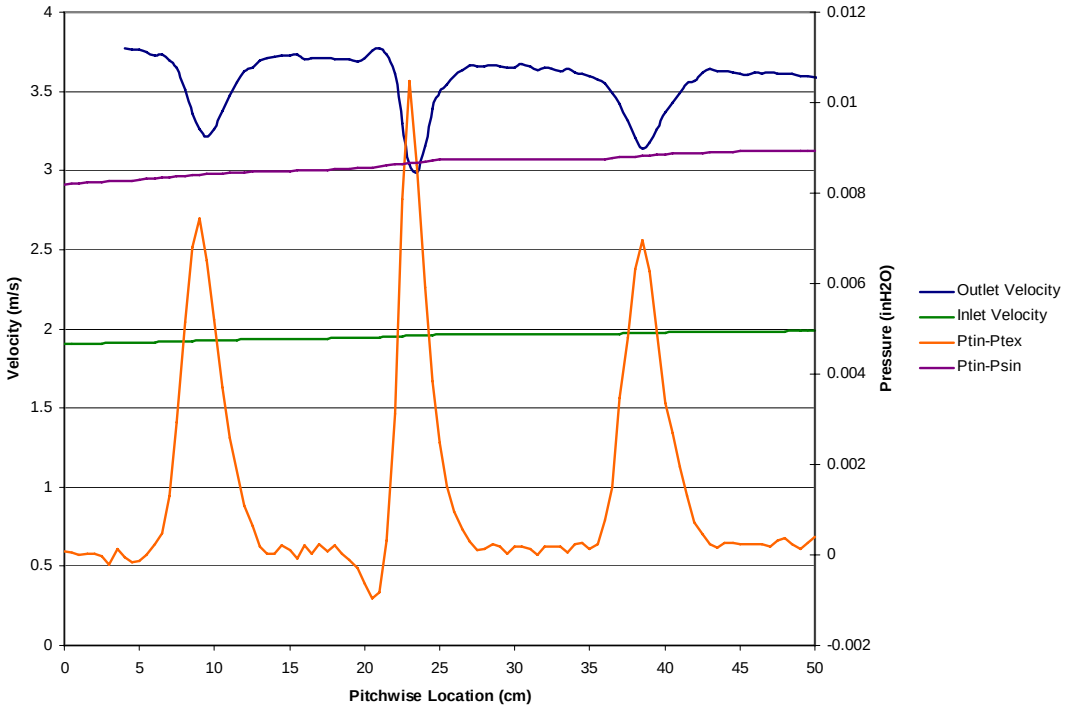

Figure 13. GH1R sample of data from four measurements, 20K Re

3.3.1 Temperature Instrumentation

Four J-type thermocouples are used to measure static temperatures (Figure 12). The air conditioned instrumentation rack is monitored by thermocouple #1. The inlet temperature is measured by thermocouple #2, which is suspended 45.7 cm downstream of the turbulence grid and 145 cm upstream of blade #1. Thermocouple #3 is located just upstream of the flow straightener honeycomb in the bell mouth. Thermocouple #4 is suspended at the 40% axial chord line of blade #1. The thermocouples are accurate to $\pm 0.2^{o}$F. The only thermocouple used for this research is thermocouple #2.

Static temperature measurements are used in the software to calculate density. The experimental conditions were such that incompressibility was assumed (M on the order of 0.006 to 0.026), and the ideal gas law was used:

$$\rho = \frac{P}{RT} \tag{17}$$

where ρ is density, P is ambient static pressure, T is tunnel temperature and R is the gas constant for air [13]. The ambient static pressure is a user input.

3.3.2 Velocity Instrumentation

Hot-films were used for all velocity measurements. Inlet velocities and exit velocities are measured using a single element hot-film (TSI 1211-20). The inlet velocity measurements set the tunnel speed for Reynolds number matching. The measured exit velocities are used to obtain wake velocity profiles.

The inlet hot-film is inserted into the tunnel through the test section floor (Figure 12). It is positioned one axial chord length upstream of the passage between blade #4 and blade #5. The purpose of this hot-film is to measure the inlet velocity used in Reynolds number calculations and act as a reference for setting inlet flow speed. The Reynolds number in the tunnel is determined using Eq. 18:

$$\mathrm{Re}_c = \frac{\rho U c}{\mu} = \frac{\left(\frac{P}{RT}\right) U c}{\mu} \tag{18}$$

where c is axial chord, U is inlet velocity from the hot-film, T is the tunnel adiabatic wall temperature, P is the ambient pressure, and μ is the viscosity of air as function of temperature.

The exit velocity hot-film is supported by a Velmex 3-axis traverse. Although the traverse can move 182.88 cm from inboard to outboard, only a 50 cm traverse from inboard of Blade #4 to outboard of Blade #6 was routinely used. The hot-film is positioned downstream of the blade cascade extending through the downstream traverse slot (Figure 12). The purpose of this element is to measure the wake velocities to determine the flow structure in the exit plane of the linear cascade.

Another hot-film is used to measure boundary layer velocity and velocity unsteadiness. This probe is inserted through a slot in the outer tailboard (Fig. 12) through the boundary layer traverse slot (Fig. 9). This probe is traversed orthogonally to the suction surface of Blade #5. Boundary layer traverses were taken at 4 chord-wise locations 65.7%, 79.4%, 90.8%, and 100%.

3.3.3 Pressure Instrumentation

A pitot-static probe extends from the bottom of the tunnel one axial chord length upstream of blade #5 through the upstream slot (Figure 12) and is supported by a Velmex 3-axis traverse. The pitot-static probe moves with the traverse. The difference between total and static pressure at this location yields the inlet dynamic pressure. The pitot-static probe is used as the upstream total pressure reference. In the current research, the pitot-

static probe was inserted one axial chord length upstream of blade #5 about 30 cm from the tunnel floor.

A Kiel probe is located one axial chord length downstream of the cascade. The Kiel probe is suspended into the tunnel by the same Velmex traverse system as the exit hot-film and positioned approximately 4 cm behind the hot-film on the same mount. The two instruments step together as the traverse moves. It extends into the tunnel through the downstream traverse slot (Figure 12). During wake loss traverses, the Kiel traverses along the exit plane from the turbine cascade in unison with the hot-film. The upstream and downstream total pressures are measure periodically by the pitot-static tube and Kiel probe, respectively. The difference in total pressure is used to calculate a total pressure loss coefficient. Local total pressure loss coefficient is the differential between inlet and exit total pressure divided by the differential between inlet total and static pressure:

$$\omega = \frac{\left(\overline{P_{t,inlet} - P_{t,exit}}\right)}{\left(\overline{P_{t,inlet} - P_{s,inlet}}\right)} \tag{19}$$

where $\left(\overline{P_{t,inlet} - P_{t,exit}}\right)$ is a time average of direct differential samples of inlet and exit total pressures, and $\left(\overline{P_{t,inlet} - P_{s,inlet}}\right)$ is a time average of direct differential samples of inlet total and static pressures.

All of the pressure measurements are fed through a pressure manifold and into a Druck LPM 5481 pressure transducer. This transducer converts the pressure readings to voltages understood by the data acquisition cards. Figure 14 illustrates the pressure instrumentation system. The computer program controls the Scanivalve selector and determines from which source the pressure transducer receives an input. The selected

pressure is sent through the pressure manifold into the transducer. The upstream total pressure is always sent through the manifold. The manifold can be set to vent either side of the transducer during calibration.

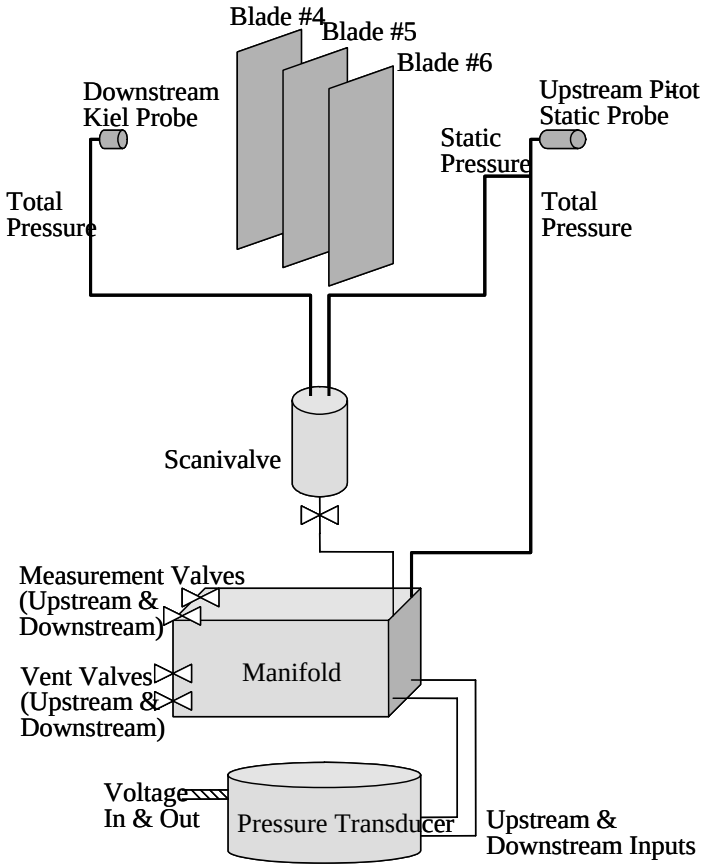

Figure 14. Pressure instrumentation schematic

3.4 Data Collection Methodology

Various LabVIEW^{TM} programs or virtual instruments (VIs) are used in this study. There are three main VIs that were used. The first is the VI to calibrate the pressure transducers. The pressure transducer is calibrated off line using a high precision

reference. This program uses the voltage returned from the pressure transducer at known pressures stepped up throughout the calibration to return a slope and x-intercept. These two values comprise a calibration file for the pressure transducer that is called up by other VIs.

The second main program is the one used to calibrate the hot-films and hot-wires. During this calibration the pressure calibration file created in the previously discussed VI is called up and used. The pressure transducer is used with a hot-film calibration stand to set known velocities. The voltage is collected at each of these known velocities and used to create a hot-film calibration file, which is called up in the data collection VIs.

The final and mainly used VI is the data acquisition VI. This program uses the hot-wire calibration files to convert voltages returned by the hot-film into velocities and Reynolds numbers. Once the wind tunnel flow speed is set, the data acquisition VI is started. The LabVIEW™ data acquisition program requires hot-film calibration data, pressure transducer calibration data, current dew point temperature, and current ambient pressure. The slope of the pressure transducer calibration curve is very stable, but the intercept can shift day to day with temperature. To account for this a zero intercept is taken at the beginning and end of each data run.

The data acquisition program drives the Velmex V-9000 traverse supporting the Hot-film and Kiel probe, and inlet pitot-static probe. For this experiment, the traverse was taken across blades #4, #5, and #6 in a 50 cm pitch-wise sweep in 0.5 cm steps. Measurements were recorded for many different Reynolds numbers.

As the traverse moves from inboard to outboard in 0.5 cm steps, the exit velocity and total pressure differential between the upstream and downstream locations are

recorded. At the farthest outboard position, the Scanivalve selector switches to the upstream static pressure input. As the traverse returns to the inboard position in 10 equal steps, the upstream total to static pressure differential (dynamic pressure) is recorded. At the beginning and end of a traverse, the Scanivalve selector switches to an ambient pressure port to record a zero pressure differential, ensuring minimal thermal drift in the pressure transducer.

3.5 Data Reduction and Analysis

Further calculations were performed on the types of data mentioned above to quantify total pressure loss, outlet turbulence, and the integrated total pressure loss coefficient. The data reduction and use of each of these data types will be briefly discussed here.

3.5.1 Wake Velocity Profiles

Wake velocity profiles provide meaningful information about the flow structure leaving the turbine blades. The velocity profiles aid in the visualization of the momentum deficit. A smooth, stable flow field is evidence of the blade operating efficiently. A choppy wake could indicate large vortical structures shedding off the blades. Ideally, the wake profile is a series of peaks and valleys. The maximum velocity should occur at the centerline of a blade passage with a minimum just behind the trailing edge of a blade. As the Reynolds number decreases the flow does not turn all the way

around the blades and the peak velocity shifts outboard as does the minimum velocity. At very low Reynolds numbers, the flow separates effectively changing the blade shape and thus further reducing the turning angle (Figure 15). A larger turning angle yields more extractable work from the flow. All profiles generated in this study are non-dimensionalized by the maximum velocity recorded for a given traverse. All of the traverses were run from the pressure side of blade #4 to the suction side of blade #6, and the plots represent the wake region behind blade #5. A complete set of profiles is included in Appendix D.

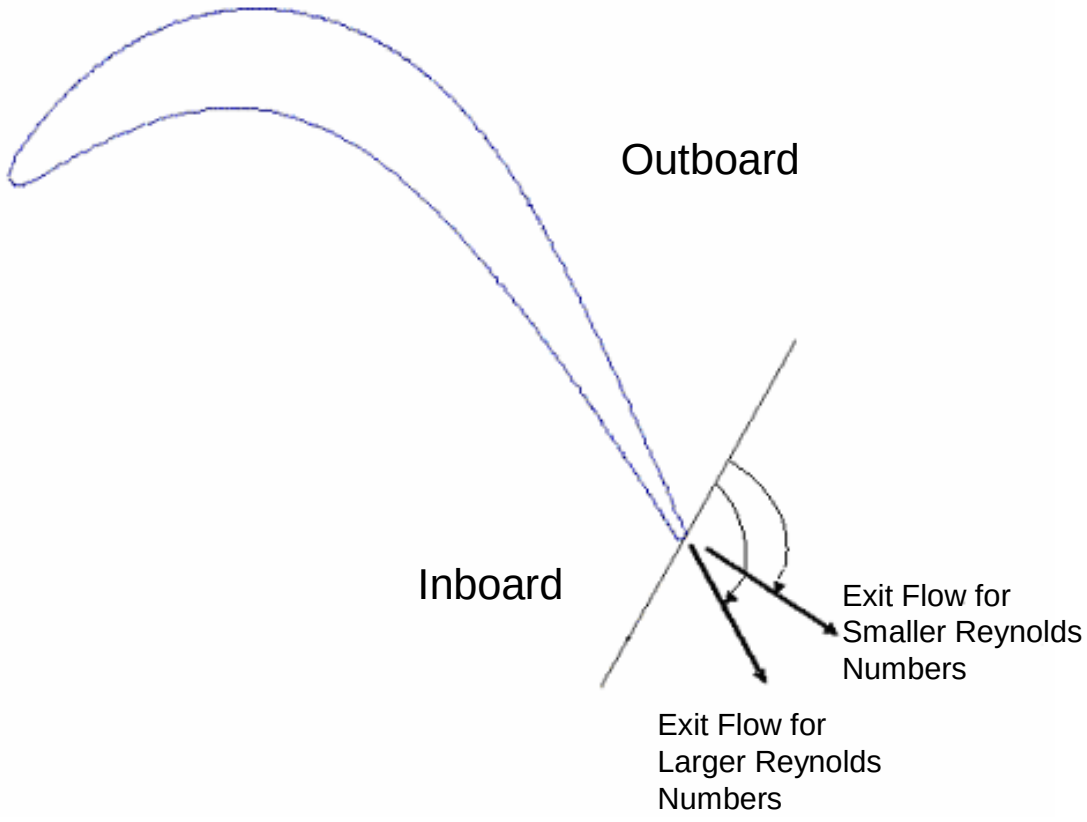

Figure 15. Reynolds number effect on exit velocity angles

Figure 16 shows the effect of Reynolds number on wake velocity profiles. The measured velocities have been normalized by the maximum measured in the outlet wake during the traverse velocity to obtain a percent of the maximum velocity.

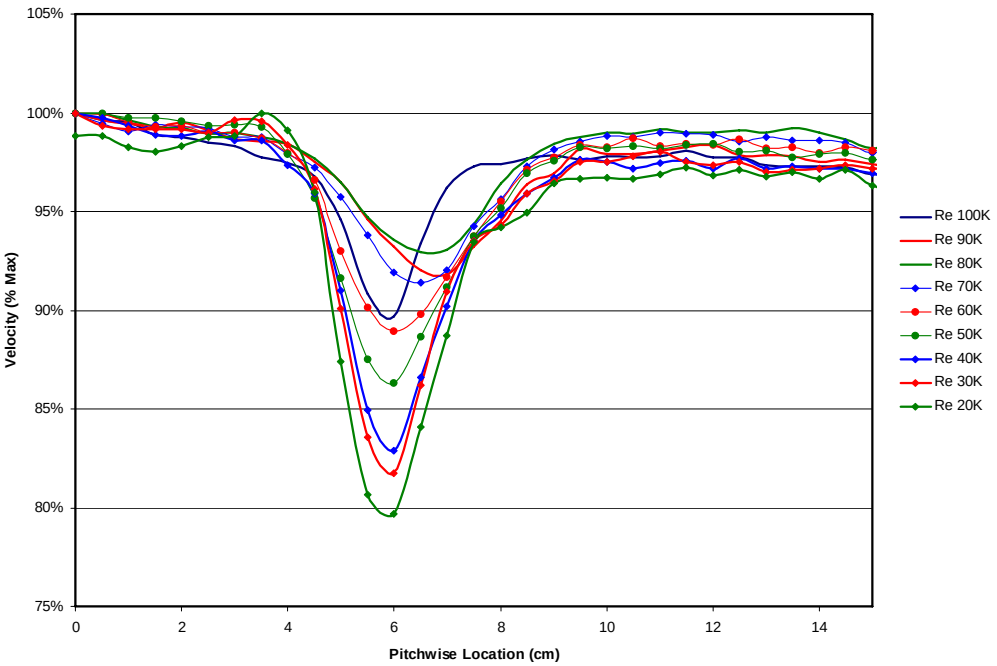

Figure 16. Reynolds number effect on wake velocity profile of a GH1R blade

As expected the higher Reynolds numbers have a narrower deficit region. At Re 20k, the minimum value is 80% of the freestream and is centered at about 6 cm. The valley spans about 6 cm. Increasing the Reynolds number to 50k, yields a minimum velocity of 86% of the freestream centered about 6 cm. Further, at a Reynolds number of 100k the minimum velocity is about 90%. There is little improvement in the minimum velocity when compared to the Re 60k case; however, the expanse of the valley for the Re 100k case is about half as wide decreasing from 4 cm to 2 cm and centered about 6 cm. The pitch-wise shift and decrease in valley expanse indicates the flow is more attached and is exiting the cascade on a more on-design angle. These effects suggest a higher blade loading due to a greater wetted surface and more efficient blade operation

due to the reduce wake region. It can also be noted that the velocity peak actually decreases from 100K to 80K and then begins increasing again from 80K until 20K. This early increase in velocity is due to shedding frequency and increased mixing.

3.5.2 Total Pressure Loss Coefficient

Measurements of total pressure loss through the cascade are the most direct way to evaluate turbine performance. Total pressure loss measurements evaluate the entropy production in the system. In this research, total pressure is measured both upstream and downstream of the GH1R blade cascade. From this information a non-dimensional quantity can be calculated, namely the total pressure loss coefficient. The total pressure loss has a direct correlation to engine efficiency as shown in Eq. 12.

Similar to the wake velocity profiles, the loss coefficient profiles focused on the wake region behind blade #5. A complete set of profiles is included in Appendix D.

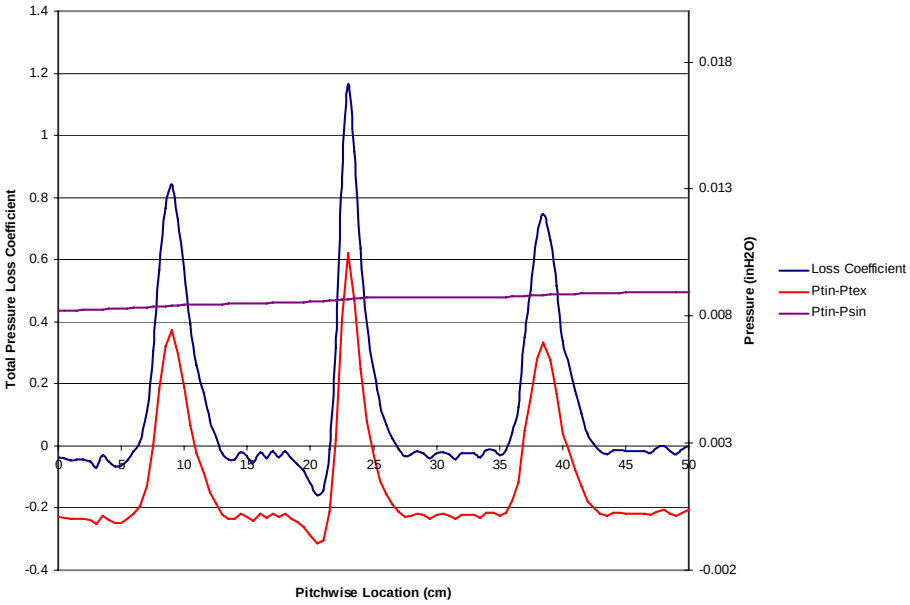

Figure 17. Sample of pressure data taken and the resulting total pressure loss coefficient, Re 20K

3.5.3 Comparison of Integrated Total Pressure Loss Coefficients

Integrating the local total pressure loss coefficient, ω, across the cascade pitch (14.8 cm) and normalizing by the pitch yields an integrated total pressure loss coefficient, γ. This is a bulk quantity that provides insight into the total effect of any changes made and is much easier to compare than the total pressure loss coefficient lines. An area-weighted average total pressure loss coefficient using the inlet dynamic pressure based on the differential of inlet total and static pressure was used in this research (Eq. 19). Also, for a bulk performance indicator the local total pressure loss coefficient was integrated over and normalized by the pitch.

Figure 18 is a sample of total pressure loss coefficient wake traverses at a Reynolds number of 20,000, 25,000, and 30,000. These plots were randomly chosen to show that it is somewhat difficult to compare total pressure loss coefficient wake plots.

Though the total pressure loss coefficient wake traverse plots may be difficult to compare, they are very useful to assure that certain known trends are present and allow you to assure that data sets are correct. For example, if you run many wake traverses at close to the same Reynolds number and one wake traverse plot does not look like the others; it allows you to determine that something went astray in that outlying data run.

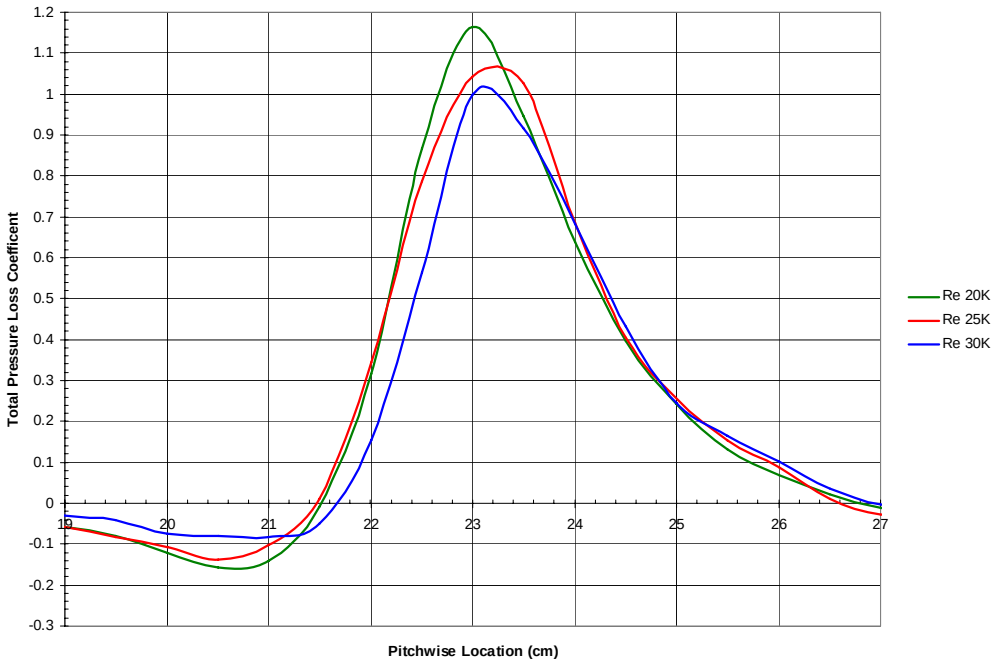

Figure 18. Sample total pressure loss coefficient wake traverses

By integrating under the total pressure loss coefficient wake traverse plot, using the Simpson's Rule, Eq. 20, and normalizing the result with the pitch of the GH1R cascade, 14.8 cm, you arrive at the integrated total pressure loss coefficient (ITPLC). The ITPLC for the three runs shown in Figure 18 has been calculated and plotted in Figure 19. It can be noted that these values are much easier to compare, especially when comparing many data sets. Each line becomes a single point on the graph.

$$\int_a^b f(x)\,dx = \frac{\Delta x}{3}\cdot\left(f\left(x_0\right) + 4\cdot f\left(x_1\right) + 2\cdot f\left(x_2\right) + 4\cdot f\left(x_3\right) + \ldots\ldots\ldots + 2\cdot f\left(x_{n-2}\right) + 4\cdot f\left(x_{n-1}\right) + f\left(x_n\right)\right)$$

$$\Delta x = \frac{b-a}{n} \qquad (20)$$

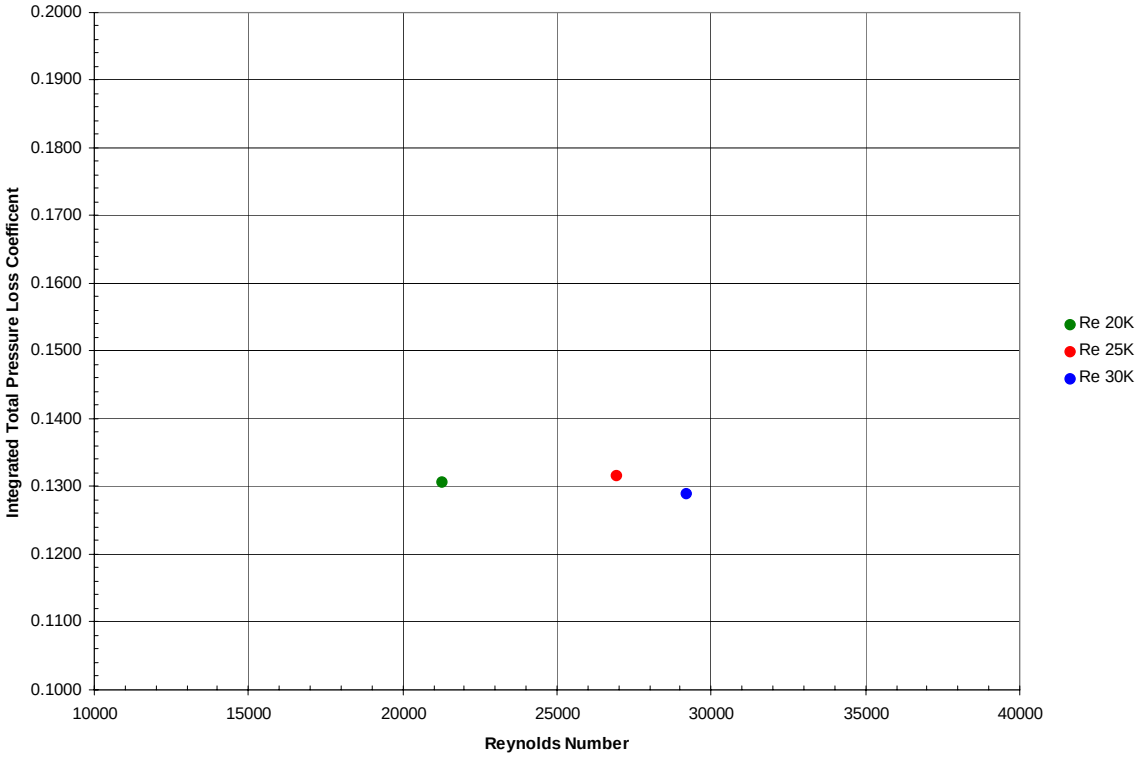

Figure 19. Sample integrated total pressure loss coefficient

The ITPLC is very useful and was the main plot used to characterize the GH1R blade set. A full set of runs, as will be shown in the results section, displays where the blade set has the highest losses and where these losses rapidly change. They also allow areas of interest to be determined for future studies.

3.5.4 Boundary Layer Profiles

A TSI 1210-20 hot-film was used to measure the velocity within the boundary layer at four axial chord locations on Blade #5. The hot-film is mounted to a National Aperture, Inc. motorized 5.08 cm MM-3M micro-traverse, and is operated using a LabVIEW™ VI.

The boundary layer traverses are the most difficult of each of the experiments and take the most time. Initially, the wind tunnel is set to a Reynolds number of 100k at 1%

turbulence. The probe is positioned approximately 30 mm above the blade surface. It is important that the probe be aligned orthogonal to the blade surface at the desired axial chord location. The LabVIEW™ program dedicated to recorded boundary layer traverses is started. User inputs drive the probe towards the blade slowly. At each step the hot-film returns velocity information. This information is displayed in the user interface to the LabVIEW™ program. Once the velocity measurements reduce to half of the freestream velocity, the user records the distance to the blade surface (or nominal wall location). The traverse direction is reversed and the small steps are taken away from the blade to finely resolve the boundary layer. At the end of the traverse, the tunnel is set to a Reynolds number of 50k, and the process was repeated. This time, however, the probe is driven to the previously recorded nominal wall location. This is repeated for Reynolds numbers of 25k, 15K, and 10K. At the end of these five runs, the tunnel is shut down again and the probe repositioned at the next axial chord location. The process is started again determining a new nominal wall location. Boundary layer traverses were taken at 65.7%, 79.4%, 90.8%, and 100% of the axial chord for the GH1R blade.

Figure 20 displays a sample of the resulting data from a traverse of the GH1R blade number 5 (Fig. 10) at 100% axial chord, which is the trailing edge of the blade, at a Reynolds number of 10K. This data set shows a freestream velocity of 1.4 m/s and it can be seen that the velocity rapidly decreases as the boundary layer is entered, in this case at a pitch normalized position of 0.05. This data example shows no separation.

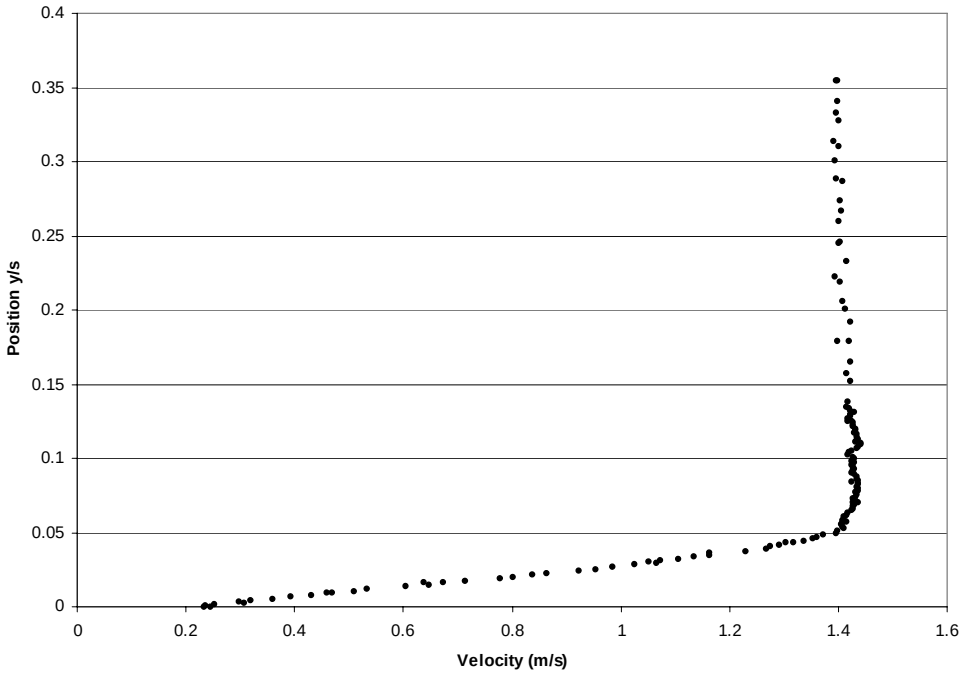

Figure 20. Example of GH1R boundary layer traverse data, Re 10K, 100% Axial Chord

3.6 Summary

In this study five different measurements were taken during wake traverses. One is a reference temperature measurement, which is used for atmospheric condition and hot-film calculations. Two of these are pressure measurements; the direct differential samples of inlet and exit total pressures, and the direct differential samples of inlet total and static pressures. These pressure measurements give the greatest ability to understand the blade set and compare performance at various Reynolds numbers. The last two are the upstream and down stream velocities. The upstream velocity measurement is used to calculate the Reynolds number of the run, while the downstream measurement is used for

velocity profiles that give more information about the runs at each Reynolds number. These measurements allow the blade set to be studied and better understood. Figure 20 is an excellent summary of these measurements and the values that are calculated from them for one run at a Reynolds number of 20,000.

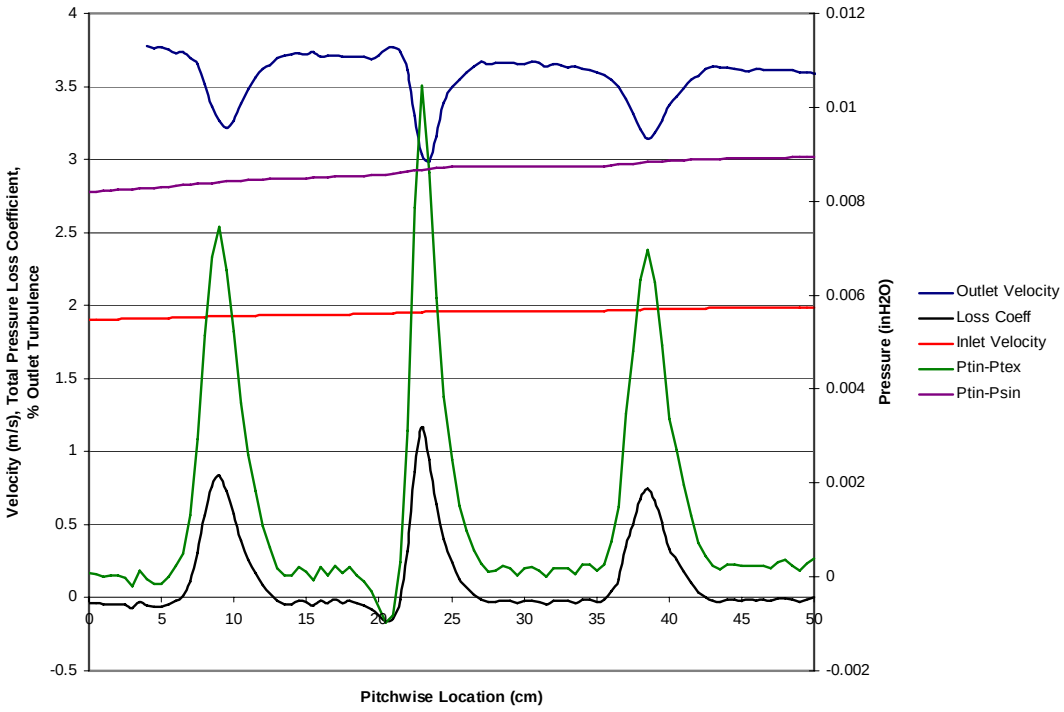

Figure 21. Re 20K summary of measurements and resulting calculations

In summary, the two pressure measurements displayed in Figure 20 are used to calculate the total pressure loss coefficient line, and then the area under this curve normalized by the pitch of the blade set is the integrated total pressure loss coefficient, which is the main tool for comparison and understanding of this blade set. The inlet velocity is used to calculate the Reynolds number of each run. The outlet velocity is used to learn more about each run.

During the boundary layer traverse only 3 measurements are taken, the inlet hot-film velocity which is used to set the Reynolds number of the run, the boundary layer

hot-film velocity, and a reference temperature used by the hot-film. The boundary layer traverses are used to better understand what is occurring on the blade surface.

CHAPTER 4. ANALYSIS AND RESULTS

The first objective of this study was to take data and assure that it matched past data taken by Casey [14]. These early validation runs were performed on the test set up previously used with the Pak-B cascade. In this way, it was confirmed that the test set up was producing repeatable results. The wind tunnel was found to be operating as well, if not better, than in past studies. This validation is discussed in detail in Appendix A.

The second objective of this study was the physical modification of the wind tunnel to accept the GH1R blade set and to adjust it to the GH1R operating angles. This was also successfully completed and the methods of this change over are fully discussed in Appendix B.

The third and final objective of this study was the preliminary characterization of the GH1R blades set. This process was begun by taking data sets at various Reynolds numbers and assuring that it matched past trends. In this way it was assured that the data were reasonable before moving on. Past research [2; 3; 14] has shown that as the Reynolds number decreases the total pressure loss coefficient traverse profile should become thinner and taller. It can be seen from Figure 22, that the data for the GH1R blade set did indeed follow this trend providing an initial level of reassurance regarding the validity of the data.

After the data was shown to match past trends indicating that the test set up and instrumentation were apparently working properly, many more data sets were acquired in order to fully characterize the GH1R blade set. First, data were taken at Reynolds number increments of 10,000, starting at 100K and working down to 20K. Next, the gaps were filled once again using 10K increments starting at a Reynolds number of 95K and

working down to 15K. During this process, more troubleshooting was required on the test set up. This process is fully discussed in Appendix D.

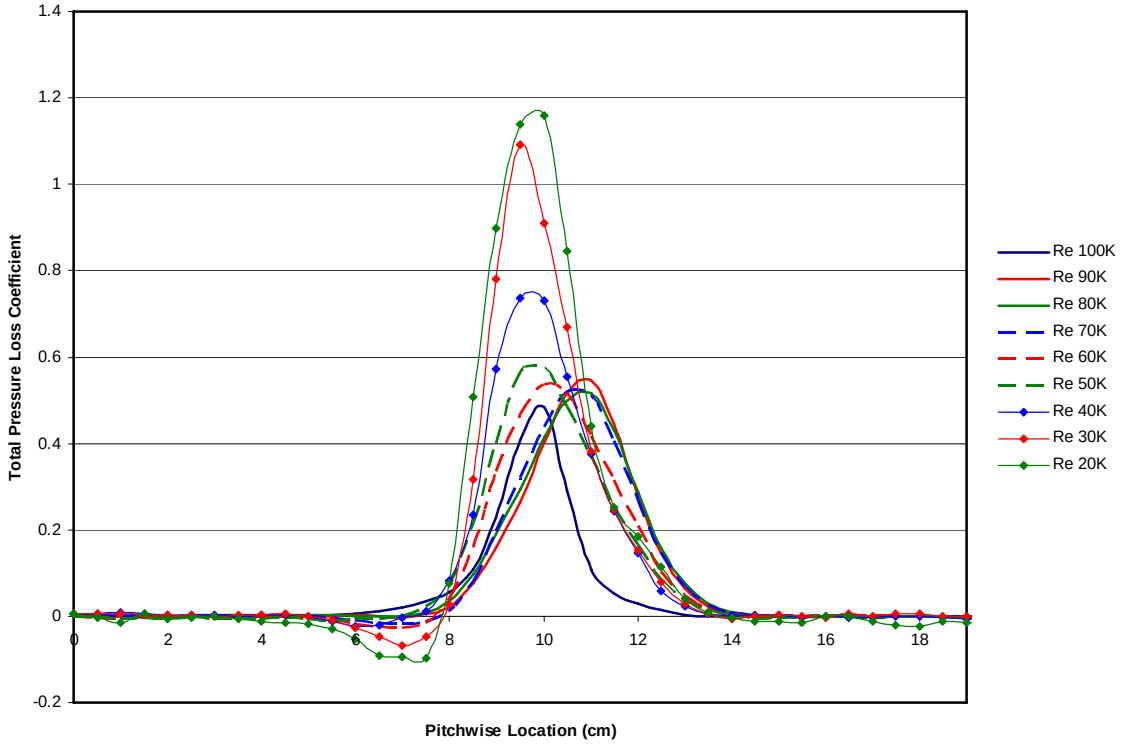

Figure 22. Total pressure loss coefficient Re 20K to Re 100K

The total pressure loss coefficient wake traverse profiles closely followed past trends. As Reynolds number was decreased the profiles became taller and wider, which leads to higher losses. It can be noted that the total pressure loss coefficient is hard to compare, and this is only nine data sets, as more are added the plot becomes impossible to read. These losses are more easily compared using the integrated total pressure loss coefficient plots as discussed earlier, though studying the non-integrated plots did display trends not previously noticed in the Pak-B studies. As shown in Figure 21, there is negative loss region, or gain, for low Reynolds numbers, most notably 20k and 30k,

between 5 and 8 centimeters along the pitch-wise span. This effect begins at Reynolds numbers around 70K and incrementally increases as the Reynolds number is reduced. This trend was also seen in the velocity profiles as an increase in velocity, at the same location as the gain begins, which reduces again at the same point the gain decreases (Fig.15). More research is required to determine the cause of this trend, but it is speculated that the gain is due to pressure side separation on the previous blade, which causes a localized jet, and in turn a gain, or negative pressure loss.

Figure 23 is the result of integrating all of the total pressure loss coefficient profiles and normalizing by the GH1R cascade pitch, 14.8 cm. It can be seen that the GH1R data shows the same trends previously seen in the Pak-B studies [2; 3; 14], as the Reynolds number increases, the ITPLC decreases.

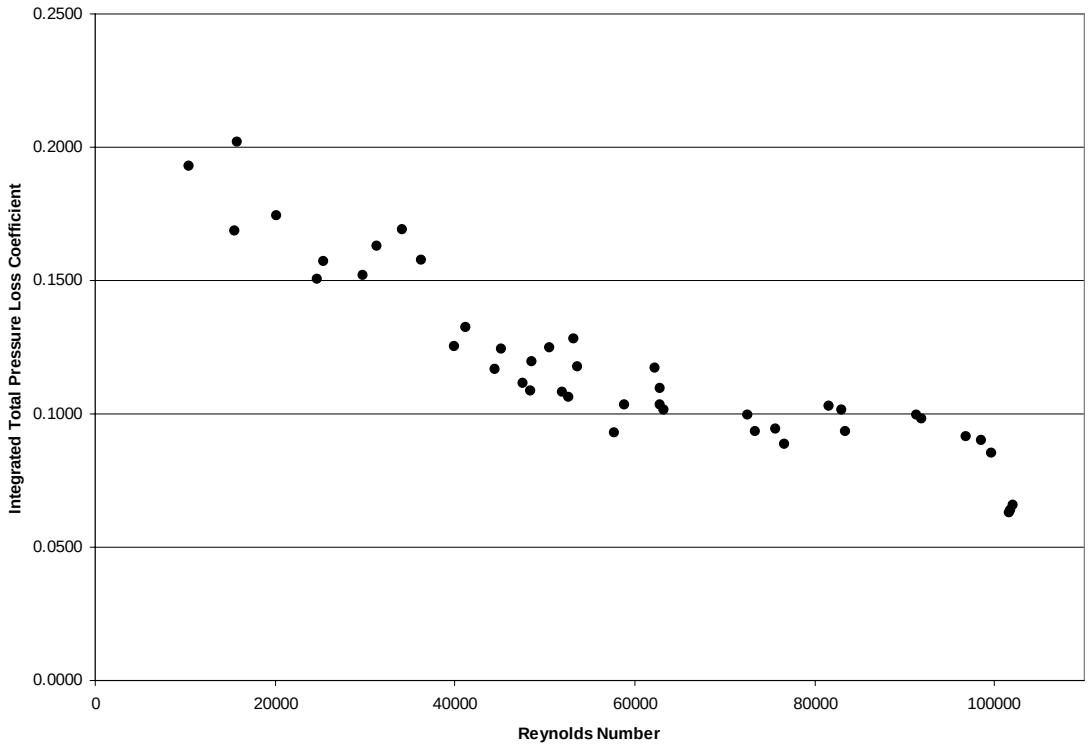

Figure 23. Integrated total pressure loss coefficient final data for the GH1R blade set

In order to gain a better understanding of the actual profile being formed, the data was averaged within Reynolds number bands. These bands were from 15K to 100K incremented by 5K. The average Reynolds numbers that fell within 2,500 of these bands were averaged together to form the data plot displayed in Figure 24. The data bands showed little variance except for extreme points and the mid range. The mid range and low Reynolds number variance is most likely due to lack of resolution of the pressure transducer. This problem was found in the data taken for Reynolds numbers below 40K and corrected, but appeared again at and below 15K. This is discussed in appendix F. The variance at the 100K band is due to a rapid drop in AITPL that occurs below 100K. Some of the data sets in that band are above 100K and show a noticeable decrease in loss, as can be seen in Figure 23.

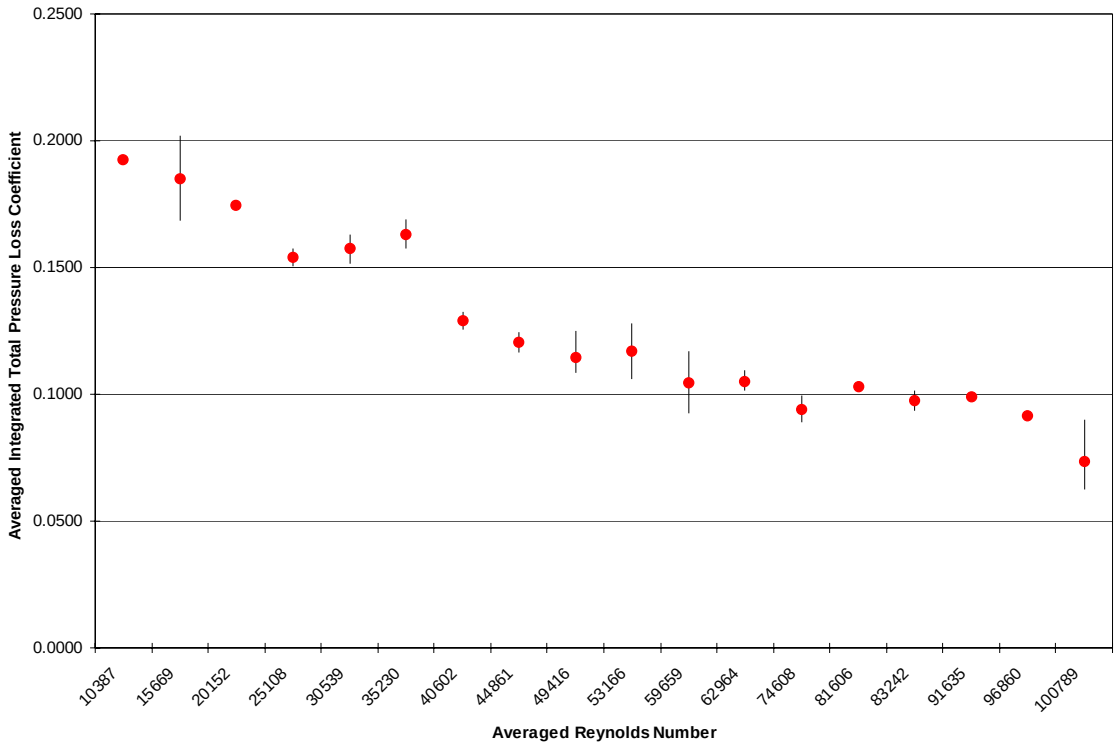

Figure 24. Average integrated total pressure loss coefficient for the GH1R with error bars

A comparison of the GH1R ITPLC profile to that of the previously studied Pak-B, and the theoretical laminar loss model is shown in Figure 25, as well as the main operating condition of the Global Hawk. The operating condition is the inlet Reynolds number to the Global Hawk first rotor for a high cruise flight condition at 65,000 ft, -70 deg F, and a Mach number of 0.6. This is the operating condition where the Global Hawk spends most of its time. Computation of this value is discussed in the Background and Theory section.

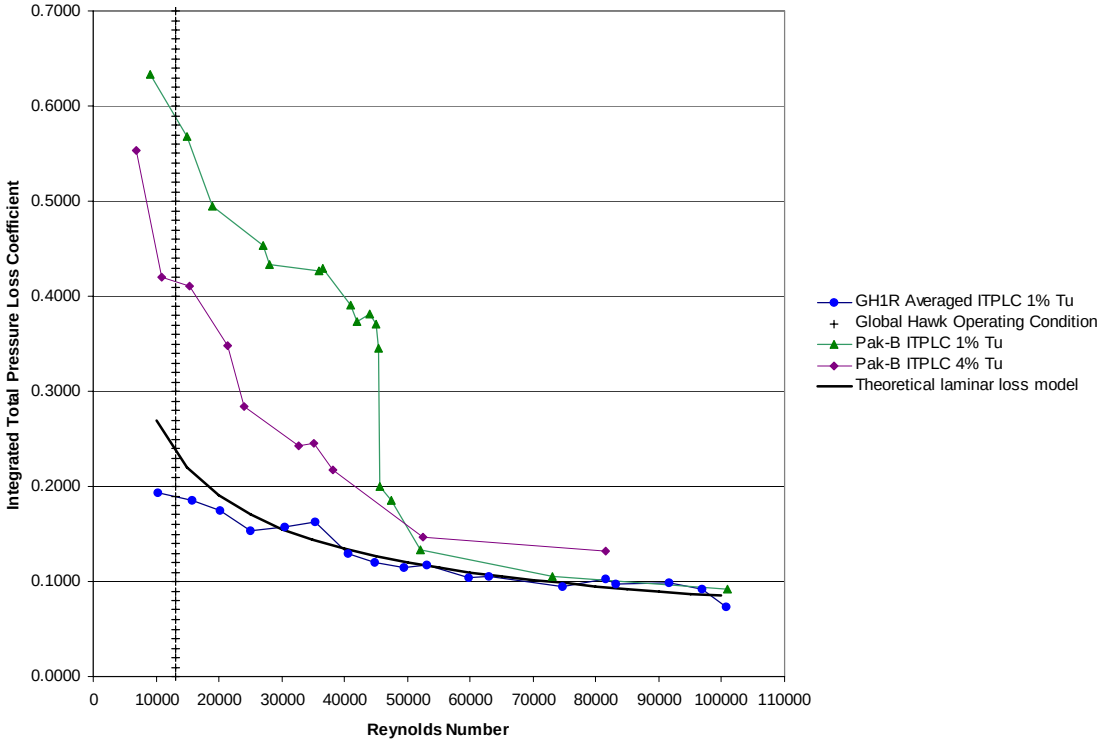

Figure 25. Comparison of GH1R ITPLC at 1% Tu to Pak-B ITPLC at 1% Tu and 4% Tu, theoretical laminar loss model, and Global Hawk operating Reynolds number

It can be seen that the operating Reynolds number for the Global Hawk first rotor is very low and much lower than the Reynolds numbers previously studied. Lake [2] performed studies with Reynolds numbers as low as 45K, while Rouser [3] and Casey [14] did studies with Reynolds numbers as low as 25K. More research should be

accomplished near the operating point of the Global Hawk's LPT. Figure 25 presents a comparison of the new GH1R data collected in this study to the Pak-B data provided by Dr. Rolf Sondergaard of AFRL, which is a much larger Reynolds number range than that covered by Lake, Rouser, or Casey [2; 3; 14]. It can be seen that though the GH1R shows the same basic trend as the Pak-B, and has similar loss values at high Reynolds numbers, the two data sets vary greatly at lower Reynolds numbers. Two Pak-B data sets are represented at two different turbulence levels. The GH1R data was taken at 1% turbulence, while the Pak-B data has been taken at both 1% and 4%. Higher turbulence leads to a reduction of losses. It is know that a laminar boundary layer can withstand only a minor adverse pressure gradient, while a turbulent boundary layer can withstand a much stronger adverse pressure gradient region without separation [4]. The GH1R shows much lower losses at lower Reynolds numbers than even the 4% turbulence Pak-B data set. The GH1R has a max loss of just under 0.2 while the Pak-B at 1% turbulence has a loss of 0.63, more than three times as large.

These very low losses were not previously expected due to the similarity between the Pak-B and GH1R blades. The Pak-B has a total turning of 95 deg with an inlet angle of 35 deg, and an exit angle of -60 deg, while the GH1R has a total turning of 91.69 deg with an inlet angle of 30.75 deg and an exit angle of -60.94 deg. The Pak-B and GH1R have very similar total turning, inlet and exit angles, so one should expect similar total pressure loss coefficients. This much lower loss is most likely due to the GH1R's higher solidity. Low solidity, or a small number of widely spaced blades, leads to high stagnation-pressure losses from separation of the flow from the suction surface [22].

The theoretical laminar loss model was also plotted in Figure 25. It can be seen that this model matches very nicely to the data for the GH1R. This means that the small losses shown by the GH1R are due to shear stress. To arrive at this line that was plotted,

it was noted that the average skin friction for laminar flow over a flat plate can be calculated using Equation 21:

$$C_f = \frac{0.664}{\sqrt{Re}} \tag{21}$$

where C_f is the skin friction coefficient [21]. This shows that skin friction, and there for shear stress, varies as one over the square root of the Reynolds number. If this is the case, then to determine if the GH1R's losses are mainly due to shear stress, we can plot equation 22, and compare it to the GH1R data:

$$\omega = k(Re)^{-\frac{1}{2}} \tag{22}$$

where ω is the ITPLC, k is a constant, and Re is the Reynolds number. To determine the constant, a reference point was used and the equation was modified to (Eq.23):

$$\frac{\omega}{\omega_o} = \left(\frac{Re_o}{Re}\right)^{\frac{1}{2}}$$

$$k = \omega_o \cdot Re_o \tag{23}$$

where Re_o and ω_o are the Reynolds number and ITPLC reference conditions used to find the constant. As can be seen in Figure 25 the theoretical line matches very well with the GH1R ITPLC data. This, in turn, shows that the losses seen for the GH1R blade set are due mainly to shear stress and not separation.

The low losses displayed by the integrated total pressure loss coefficient profile for the GH1R blade set and the theoretical laminar loss model plot show that there may be very little separation over the blade even at low Reynolds numbers. This hypothesis was confirmed during boundary layer traverses. There was no midline separation for the GH1R at Reynolds numbers of 10K or 15K (Fig. 26), which bracket the operating condition of the Global Hawk. Separation was also not seen at Re's of 25K, 50K, or

100K, which can be found in Appendix G. Figure 27 is an example of what the data would look like if separation had occurred. The boundary layer, or near zero velocity region, is much larger for the separation case, which shows that a separation bubble has formed. The GH1R data shows a very thin boundary layer and no separation.

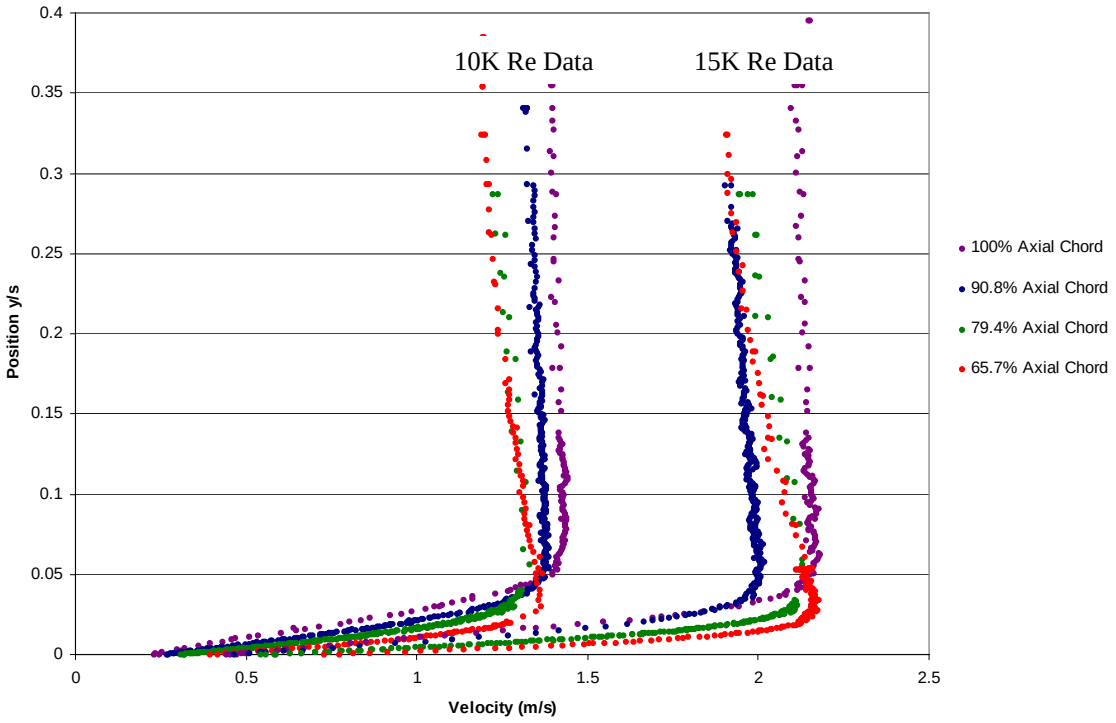

Figure 26. GH1R boundary layer profiles for 100%, 90.8%, 79.4%, and 65.7% axial chord for 10K and 15K Re

Though somewhat unexpected, characterization of the GH1R has shown that this blade set shows no separation and will not be a good candidate for pass methods of loss reduction. Though this blade is not a good candidate, one of the other five Global Hawk low pressure turbine blades may be.

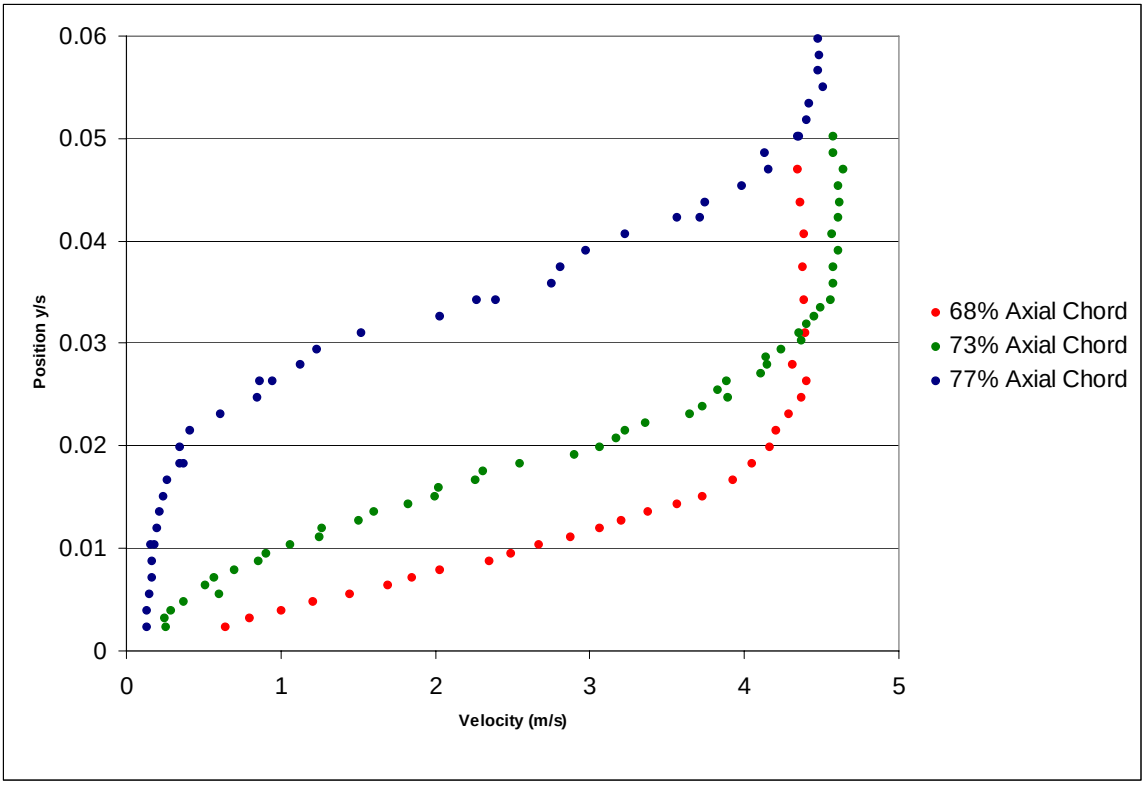

Figure 27. Sample plot of what boundary separation would look like

CHAPTER 5. CONCLUSIONS AND RECOMMENDATIONS

The low-pressure turbines in aircraft flying at high altitudes and low velocities experience low Reynolds number conditions. The effect of the large turning angles associated with the low-pressure turbine blades operating at low Reynolds numbers leads to laminar flow separation. Mission essential systems, such as Global Hawk, are impacted by the problem of boundary layer separation resulting from low Reynolds number flows. Naturally, the decreased loading associated with the separated flow results in a dramatic reduction in the turbine efficiency. Decreasing the turbine efficiency directly results in limiting the aircraft range, operating ceiling and extractable electrical power from the turbine.

The objective of the current research was three fold. The first objective was to check out, troubleshoot, and validate the wind tunnel after current upgrades. This objective was met; the wind tunnel's current configuration has been debugged and validated. The upgrades to the output files to include reference temperature and inlet velocity will not only provide beneficial data but avoid future problems, such as faulty or miss-calibrated hot-films or thermocouples. In the least these additions to the data files will speed up trouble shooting. The test set up needs a device to measure dew point inside the hangar where the wind tunnel is operated. This information is currently being taken from weather.com, and we do not know where or how this data is measured. The wind tunnel is run in a non-air-conditioned hangar, which absorbs heat during the day

and retains it at night, so no mater where this data is taken, it will not be the same as in the hangar.

The second objective was the physical modification of the wind tunnel to allow the testing of the GH1R blade set. This was completed with minimal problems. The eight GH1R blade cascade has been installed, the total turning, inlet, and exit angles have been set, and the test section has been modified to allow parallel inlet and exit flow. A step by step detailed description of this modification is given in Appendix B.

The final objective was the characterization of the GH1R blade set. The GH1R blade set was run through 58 wake traverse runs in order to gain an understanding of its loss profile. It was found that the loss profile was much lower than that of the Pak-B blade set that has been the subject of study for the previous three experiments done in this wind tunnel. It was also discovered that the pressure measurements for the GH1R blade set are much lower and therefore require a pressure transducer with better resolution. Though it was not attempted in this study, using a higher resolution pressure transducer should reduce scatter fro the highly scattered region of 50K to 80K, as it did for Reynolds numbers below 45K, as discussed in Appendix F. Comparison to the laminar loss model showed that the small losses found are mainly due to shear stress, and that there was most likely no separation. Boundary layer traverses confirmed that no midline separation is experienced by the GH1R blade set.

With the calculation of the Global Hawk's main flight condition resulting in an inlet Reynolds number of 13,500, there is a better understanding of what Reynolds numbers should be studied. My recommendation for the next stage of this research is to repeat these studies for another Global Hawk low pressure turbine blade set. This will

show whether or not dimpling will help decrease losses for the low pressure turbine and improve the efficiency of the Global Hawk.

APPENDIX A. Wind Tunnel Upgrade and Validation

The first objective of this study was to check out, troubleshooting, and validate the wind tunnel after current upgrades. Wind tunnel validation included running test sets on the pack-B blade set originally set up in the wind tunnel. These tests included pressure and velocity wake traverses and a comparison to previous data provided by Casey [14], since he was the most recent user of this wind tunnel.

Many changes were made to the test configuration to both modernize it and to increase data quality. These changes were thought to be minor, but turned out to have many unplanned and unwanted ramifications. I will discuss each change and what effects it had.

Upgrade to IFA 300:

The first and most major change made was updating the TSI model IFA 100 constant temperature anemometer system to the TSI model IFA 300 constant temperature anemometer system. This was thought to be an easy upgrade but had wide spread effects on both test methods and computer virtual instruments (VIs). This change required many hours of trouble shooting on all used VIs and supporting VIs. The IFA 300 also must be reprogrammed before each test run, where the IFA 100 was hard coded with the required information.

Relocation of Data Acquisition Rack:

In order to shorten wire runs for instrumentation, the data acquisition rack was moved closer to the tunnel. This change required a new air conditioned rack due to the

high temperatures in the hanger during summer months. The new instrumentation rack caused many unexpected electrical noise problems that had to be eliminated.

First the air conditioner in the new rack and the new electrical circuit were causing ground loop problems and other electrical noise problems. This was rectified by installing two isolation transformers one for the instrumentation and one for the air conditioner, as well as connecting to an isolated instrument ground installed outside the hanger.

Electrical/Radio Frequency Noise:

Trouble shooting the previous problems made it obvious that we had other electrical/RF noise issues. The isolation transformer and new instrumentation ground helped to reduce this noise greatly, but it was still not in acceptable limits. Various circuitry and computer based filters were tried, but the effects on the data were unacceptable. To remedy these problems we replaced much of the wiring with shielded cables. It was also discovered that a Y-Banana to coax converter was acting as an excellent and greatly unwanted antenna. The previous changes brought the electrical noise into acceptable limits.

New Hot-film Type:

Previous tests used the TSI 1210-20 (Fig. 28)cylindrical film sensor (hot-film). It was determined that a more directionally insensitive hot-film would be preferable. The TSI 1211-20 (Fig. 29) was chosen. Changing to this hot-film has removed the need to precisely align the hot-films.

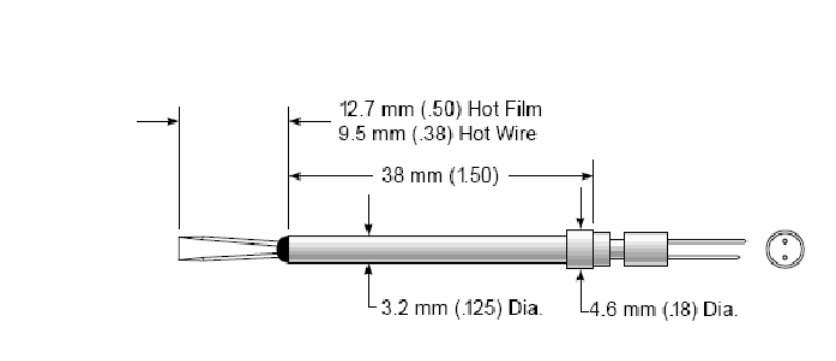

Figure 28. TSI Model 1210 general purpose probe

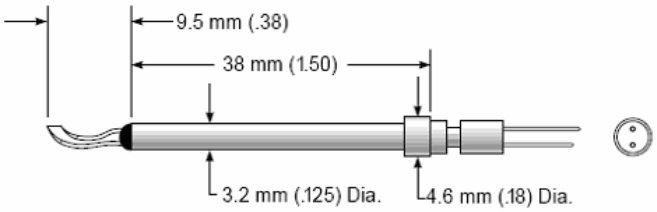

Figure 29. TSI Model 1211 standard probe

Modified Calibration Methods:

Calibration methods were found to be another area that needed some modification while trouble shooting to find noise problems. The method used to calibrate the pressure transducer was not changed, but the hot-film calibration method was greatly altered. In the previous calibration method a zero point was taken and then the velocity was stepped from 2 m/s to 24 m/s in 2 m/s increments. There were two problems found with this method. First, the pressure transducer being used in this calibration only had a range of 0 inches of water to .8 inches of water. This range only allowed a maximum velocity of about 18.9 m/s depending on current atmospheric conditions. So, the pressure transducer was being over pressurized every time a hot-film was calibrated. The pressure transducer

was checked and had not been damaged. The second issue was that in the test we are conducting we are mainly concerned with lower velocities. To fix both these issues the method was changed to taking a zero point and stepping to 5 m/s by 0.5 m/s increments, then stepping to from 5 m/s to 10 m/s by 1 m/s increments, and finally stepping from 10 m/s to 18 m/s by 2 m/s increments. This method both avoids over pressurization of the pressure transducer and gives greater accuracy at the lower velocities.

New instrumentation alignment techniques:

In previous tests the hot-films, pitot static probe, and Kiel probe were aligned by sight. To improve alignment a new VI was written and used to position these instruments. The new VI allows velocity/pressure to be constantly monitored and the instrument can be rotated until velocity/pressure is maximized depending on the instrument. This should allow better repeatability and accuracy of data.

Building Air Supply Noise:

One of the last possibilities I would have considered for noise is the building air source, but it was found to be greatly affecting the calibration of the hot-films. The building air supply was varying by 25 psi vary rapidly. This caused the known velocity being provided by the pressure transducer for the calibration of the hot-films to be inaccurate. The known velocity would be set and then would vary while the hot-film data was being taken. To remedy this, two high sensitivity regulators were used in series for the air being supplied to the calibrator. This corrected the air pressure fluctuation, and improved the accuracy of the hot-films.

Updated VIs:

As discussed above, due to changes in devices and instrumentation many LabView Virtual Instruments that had been previously used had to be updated. These updates caused many other problems along the way. In the process of updating and cleaning up the VIs other bugs were introduced. The troubleshooting and correction of the VIs was a lengthy process. The following are some of the VIs that had to be updated:

Pressure Transducer calibration VI

Hot wire/hot-film calibration VI

Loss Coefficient traverse VI

Boundary Layer VI

Supporting VIs (IFA 300 setup VI)

Data Acquisition System Validation:

The final step in the upgrade of the system was to validate that the system still worked properly. Obviously this was an iterative process and was repeated many times before the results were acceptable. To do this validation pack-B data sets were run and compared the most resent testing done by Casey [14]. As can be seen in Figures 30 and 31, the new data runs with the modified system matched up very well, both in TPLC and ITPLC. It can also be observed that the data sets taken with the new setup are much smoother due to the efforts taken to reduce noise.

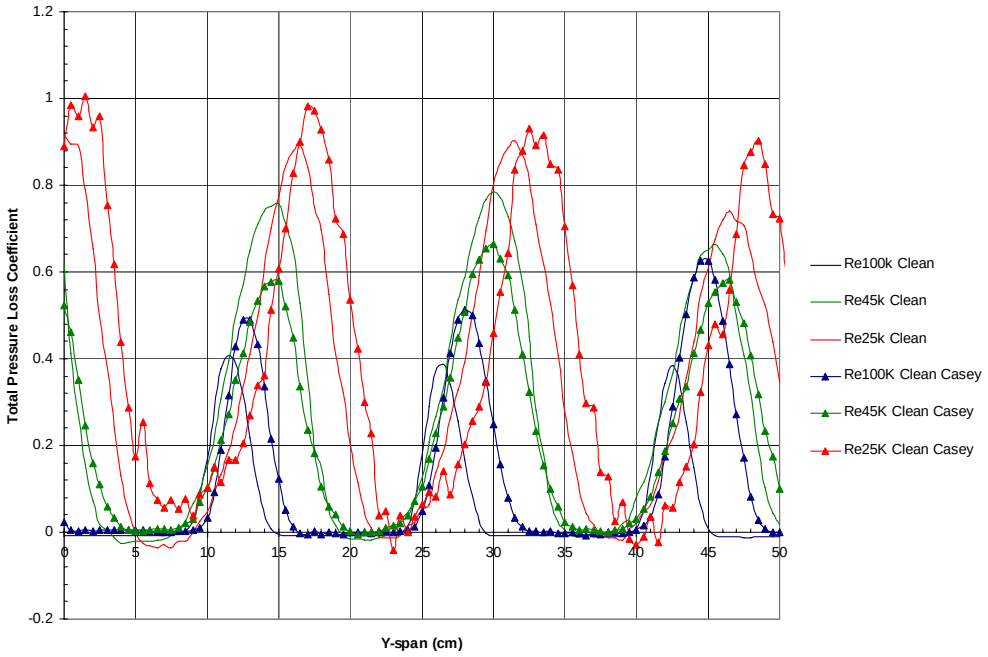

Figure 30. Total Pressure Loss Coefficient traverses compared to Casey's data [14] for wind tunnel validation

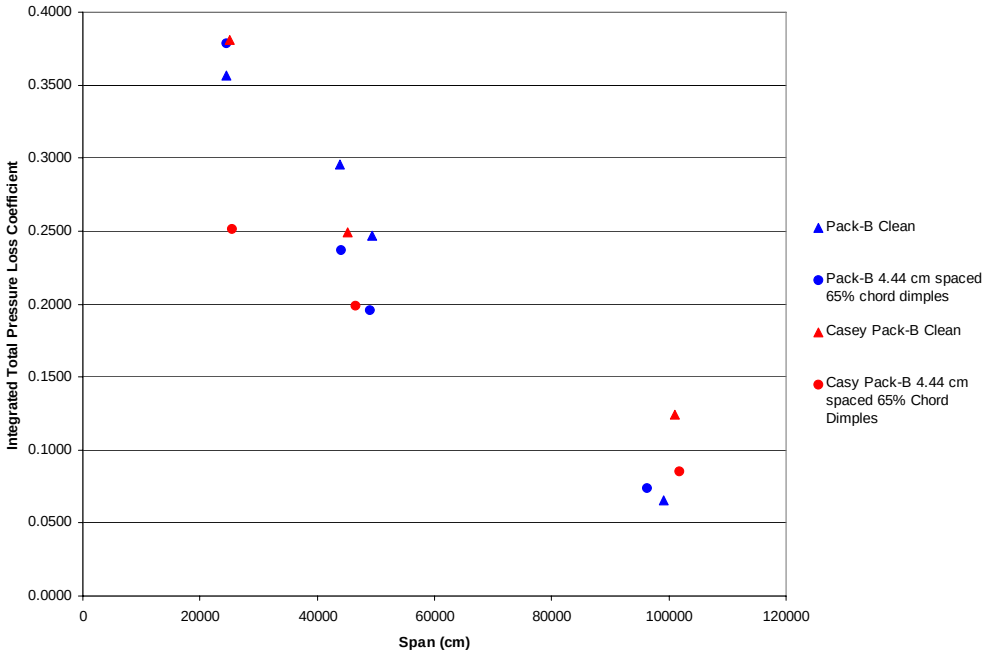

Figure 31. Integrated Total Pressure Loss Coefficient runs compared to Casey's data [14] for wind tunnel validation

Table 4. Pak-B Integrated Total Pressure Loss Coefficient comparison for wind tunnel validation

Data Type	Re of Run	Blade 5 Average Re	Integrated Total Pressure Loss Sum (cm)	Pak-B Pitch (cm)	Integrated Total Pressure Loss Coefficient
Garmoe Clean	25000	24401	5.6107	15.75	0.3562
Garmoe Clean	45000	43884	4.6540	15.75	0.2955
Garmoe Clean	50000	49380	3.8929	15.75	0.2472
Garmoe Clean	100000	99065	1.0293	15.75	0.0654
Garmoe Dimpled	25000	24571	5.9690	15.75	0.3790
Garmoe Dimpled	45000	44010	3.7271	15.75	0.2366
Garmoe Dimpled	50000	48953	3.0786	15.75	0.1955
Garmoe Dimpled	100000	96252	1.1676	15.75	0.0741
Casey Clean	25000	25146	5.9972	15.75	0.3808
Casey Clean	45000	45239	3.9279	15.75	0.2494
Casey Clean	100000	100951	1.9575	15.75	0.1243
Casey Dimpled	25000	25316	3.9558	15.75	0.2512
Casey Dimpled	45000	46071	3.1316	15.75	0.1988
Casey Dimpled	100000	101526	1.3433	15.75	0.0853

APPENDIX B. Wind Tunnel Modification

The following are steps that were required to modify the wind tunnel from the pack-B blade set to the new Global Hawk first rotor blade set. The tunnel was designed by Lake [2] with the possibility of testing other blades in mind, though the change over was more a modification than a quick change. The following steps will need to be followed for any future blade set changes.

The first step is to disconnect all of the instrumentation and remove it from the wind tunnel. This was both to have it out of the way and to avoid damaging it. The instrumentation included the upstream hot-film probe and Kiel probe, and the inlet hot-film probe and pitot-static probe. The Inlet hot-wire was not in the way and did not have to be removed.

Next the exterior upstream and downstream Plexiglas side walls had to be removed. This requires unhinging the central two walls and unbolting the walls connected to the inlet and exit section of the wind tunnel. Removing these walls allowed access to the inside of the test section. The current Pak-B blade set must remain in place until last because with the removal of the walls the blades are necessary to support the top of the test section.

After the exterior walls are removed the angle iron used to support the tunnel and guide the exterior walls must be removed. This angle iron can be found on the top and bottom interior of the test section and connects the test section to the inlet and exit section of the wind tunnel and must either be completely removed or disconnected from the test section in order to adjust the total turning angle. Failure to disconnect these supports will cause them to be bent or to rip the bolts out of the Plexiglas, neither of which is acceptable. With the angle iron disconnected the hinge point should be able to move freely.

Next the total turning angle for the new blade set must be determined. The total turning angle for the GH1R is 91.69 degrees. Because it is very hard to read this interior angle on the test section with turning foam in the way on the inside and supporting structure in the way on the outside, a new method was devised. A point 46" from the center or the hinge point was marked on the top of the wind tunnel on the inlet and exit sections. With these two know lengths forming two sides of a triangle the angle could be precisely measured by the length of the third side of the triangle. This method is visually displayed in Figures 32 and 33. The new required angle can then be used to determine a much more easily measured length using Figure 33 and equation 24. It should be noted that the angle being used in the calculation is not the actual angle but a geometric component of the angle, which is easily determined. To arrive at an angle of 91.69 deg for the GH1R blade set, the required length was calculated to be 64.0874 in.

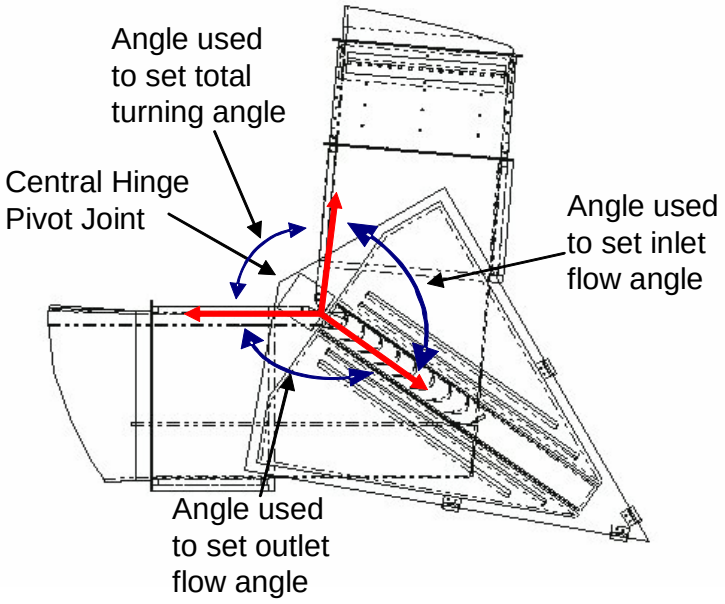

Figure 32. Location of angles used to determine and set total turning, inlet flow and outlet flow angles

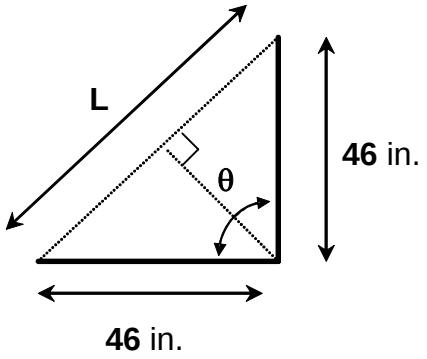

Figure 33. Triangle formed using any two of the known 46 in lengths

$$\sin\left(\frac{\theta}{2}\right) = \frac{\text{opposite}}{\text{hypotenuse}} \qquad \sin\left(\frac{\theta}{2}\right) = \frac{\frac{L}{2}}{46\cdot\text{in}} \qquad L = 2\cdot(46\cdot\text{in})\cdot\sin\left(\frac{\theta}{2}\right) \tag{24}$$

The new turning angle is set by pulling (rotating) the inlet section of the wind tunnel with a forklift. To make this easier and to avoid damage to the wind tunnel or the hangar, the floor was greased in front of the support legs in the direction of motion. Using a lifting strap, the wind tunnel is then drug slowly while the required length on the top of the wind tunnel in monitored. When the correct value is reached, the floor is marked at one of the supporting legs on the inlet section. This is a very good practice since four days after we set the new turning angle the inlet of the test section was struck with a forklift moving the test section about four times as far as we had moved it to set the new angle. Unfortunately the angle iron had already been installed and was bent, so can no longer be used to determine where to drill the holes for the angle iron, as will be discussed shortly.

Now that total angle is set, inlet and exit angles must be adjusted. First, the inlet and exit angles must be determined. The inlet and exit flow angles for the GH1R were 30.75 deg and -60.94 deg respectively. To measure the new angle the same process used to

measure the total turning angle was used once again. A point 46 in. from the center of the hinge point in the center of the top mounting plate of the current blade set was marked. The length of the third side of the triangle must once again be determined. It is only necessary to calculate this for either the inlet or exit angle since setting one sets the other in turn, but it is nice to find both as an additional check. These lengths for the GH1R were found to be 79.973 in. for the inlet angle and 89.057 in. for the exit angle. The test section is on wheels and much lighter than the inlet section and can therefore be moved by hand. The test section was rotated while the distance was monitored on the top of the test section until the new inlet angle was reached. The distance for the exit angle was then checked as an extra precaution.

The current blade set, Pack-B in this case, was then removed since additional support of the top of the test section was no longer required. There was no longer any need to move around on top of the test section and measure angles. The blade set is taken out by removing 4 bolts from each blade, two top and bottom and removing the blades one at a time.

With the blades removed and much greater access to the inside of the test section work on reconstructing the test section can begin. First, masking tape was put down on the inlet/ inlet test section marking flow parallel to the inlet flow. This is used to double check alignment of the instrumentation. The next step is to reinstall the angle iron connecting the test section to the exit section of the wind tunnel. Before the wind tunnel was hit, this could be done by bolting the angle iron to the exit section and marking and drilling new holes using the then straight angle iron to assure the wall was parallel to the exit section. Because the angle iron was bent, a laser marking tool was used to mark a straight line parallel to the outlet section's wall. The angle iron was attached to the outlet section and then bent until it was the correct distance from this line and the position of the new holes were marked and drilled. The angle iron is then bolted back into place.

This was then repeated for the top of the wind tunnel. This process is then repeated for the inlet section of the wind tunnel.

In order to locate the position of the tail board, blades one and eight must be installed. Remove the top and bottom mounting plates for the previous blade set and install the mounting plates for the new blade set. The mounting plates have been predrilled with holes in the correct pattern to maintain blade pitch and angle. Blade one is positioned in the first set of predrilled holes that allow the blade pitch to be achieved or spacing slightly larger than the blade pitch. The holes are predrilled based on the blade pitch for the GH1R and once the first blade position is set, every fourth set of holes is used. With this knowledge of blade spacing, the eighth blade can be installed and then the outside turning blade.

Next the tailboard is installed. It must be parallel to the exit section flow and come in contact with the turning blade. So the turning blade sets the distance from the outside wall and new holes must be drilled to place the tailboard against the outside turning blade and parallel to the outside wall. Once holes are drilled the tailboard is bolted in place. This must be done for the top and bottom of the tailboard.

Now that the angle iron for the exterior walls and the tailboard has been installed, the rest of the blades (blades two through seven) can be installed insuring cascade pitch. Once, all the blades are reinstalled the exterior test section walls can be wedged back in place and rebolted/hinged.

Finally, the instrumentation can be reinstalled and reconnected. The instrumentation must be realigned and test run to check for damage. The wind tunnel should also be run at various speeds starting very low and left to sit, and then slowly stepped up to insure everything is securely mounted. Once all of this is completed, you can begin testing the new blade set.

APPENDIX C. Calibration Procedures

The pressure transducer and each of the hot-films used in this research require calibration. The pressure transducer needed to be calibrated first since it is used during the calibration of the hot-films.

C.1 Pressure Transducer Calibration

Hardware Setup

1. Carefully unpack deadweight pressure calibration device
2. Set up pressure calibrator following the instruction manual [21]
3. Connect output from positive pressure reference on calibrator to high side (+) of transducer
4. Unhook or vent low side of transducer

Software Setup

1. Open LabView
2. Open ‘Pressure Cal’ vi
3. Set Xdcr Ch (1) to ‘1’ (first input on MIO)
4. Set device to ‘2’ (MIO board controlling SCXI)
5. Set ‘Pxdcr Ch’ to ‘sc1 ! md1 ! 0’ (SCXI device 1, module 1, channel 0)
6. Select sample rate and number (recommend 1000Hz max & 30,000 samples min)

Calibration Procedure

1. Place reference weight for max desired pressure on reference
2. Run vi and enter data filename
3. Enter reference pressure setting and hit OK
4. Wait for data acquisition

5. Change out reference weight to reduce pressure
6. Allow approximately 15 seconds for pressure to stabilize
7. Press ‘TAKE DATA’ button to take next data point
8. Repeat from step 3 until data taken at minimum reference pressure
9. Shut off reference and vent both sides of transducer (zero pressure point)
10. Press ‘TAKE DATA’ button
11. Enter ‘0’ for pressure setting and hit OK
12. Wait for data acquisition
13. Press ‘DONE DO FIT’ button
14. Replace calibration file in the ‘current active cals” folder.

Hardware Takedown

1. Disconnect and repack pressure calibrator
2. Reconnect instruments to transducer
   Reset valves on transducer (vents closed, measure open)

C.2 Single-Element Hot-wire/Hot-film Calibration

Hardware setup

1. Verify calibration of pressure transducer if required
2. Connect hotwire/hot-film calibrator pressure tap to pressure transducer high side
3. Vent both sides of pressure transducer
4. Blow dust out of calibrator by opening valves fully
5. Shut valves
6. Mount hotwire/hot-film in calibrator with sensor centered over nozzle perpendicular to flow
7. Follow instructions for IFA100 setup

Software Setup

1. Open LabView
2. Open ‘Hot wire Cal’ vi
3. Set device to ‘2’ (MIO board controlling SCXI)
4. Set ‘Pxdcr Ch’ ‘sc1 ! md 1 ! 0’
5. Load most recent calibration file for the pressure transducer
6. Set dew point and barometric pressure
7. Set number of samples and sample rate
8. Set DAQ channel to correct MIO channel (depends on IFA channel – Check IFA note or wiring)
9. Enter probe parameters from container

Calibration Procedure

1. Verify both sides of the pressure transducer are vented “zero pressure”
2. Run ‘Continuous Ptrans Scan’ vi
3. Obtain current zero intercept from ‘Continuous Ptrans Scan’ vi, and enter this value in the ‘Hot wire cal’ vi
4. Stop ‘Continuous Ptrans Scan’ vi
5. Open valves on calibrator slightly to begin flow over hotwire/hot-film
6. Set high side of pressure transducer to measure
7. Set appropriate IFA HW channel to “RUN”
8. Run ‘Hot wire cal’ vi
9. Enter data filename. <u>First data is taken as soon as file is created.</u>
10. Open valves on calibrator until jet is at the maximum desired calibration velocity
    DO NOT EXCEED TRANSDUCER MAXIMUM PRESSURE

11. Wait for ‘Taking Data’ light to go out
12. Reduce calibrator flow to next desired calibration point
13. Allow approximately 15 seconds for pressures to stabilize
14. Press ‘TAKE DATA’ button
15. Wait for ‘Taking Data’ light to go out
16. Repeat steps 12-15 until full calibration range is covered
17. Press ‘DONE DO FIT’ button
18. Record calibration constants (C, D, MSE). Flag with RED ink.

Hardware Takedown

1. Shut off isolator valve to calibrator
2. Mount hotwire/hot-film in tunnel
3. Disconnect calibrator pressure tap from transducer
4. Reconnect instrumentation lines to transducer
5. Reset valves on transducer (vents closed, measure open)

APPENDIX D. Total Pressure Loss Coefficient and Wake Velocity Profiles

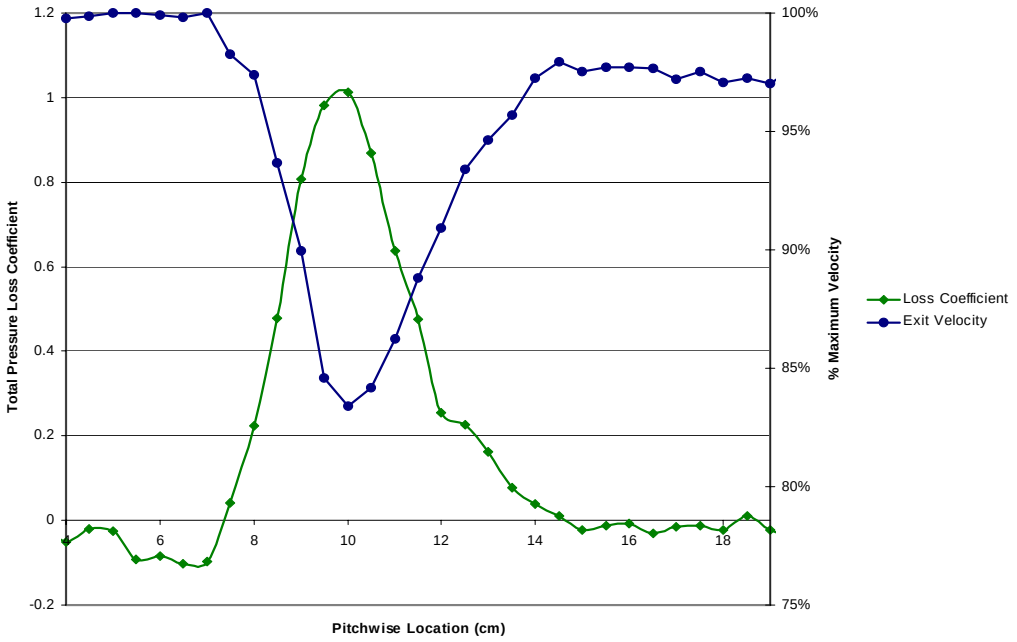

Figure 34. GH1R characterization profile for average Reynolds number of 10,387

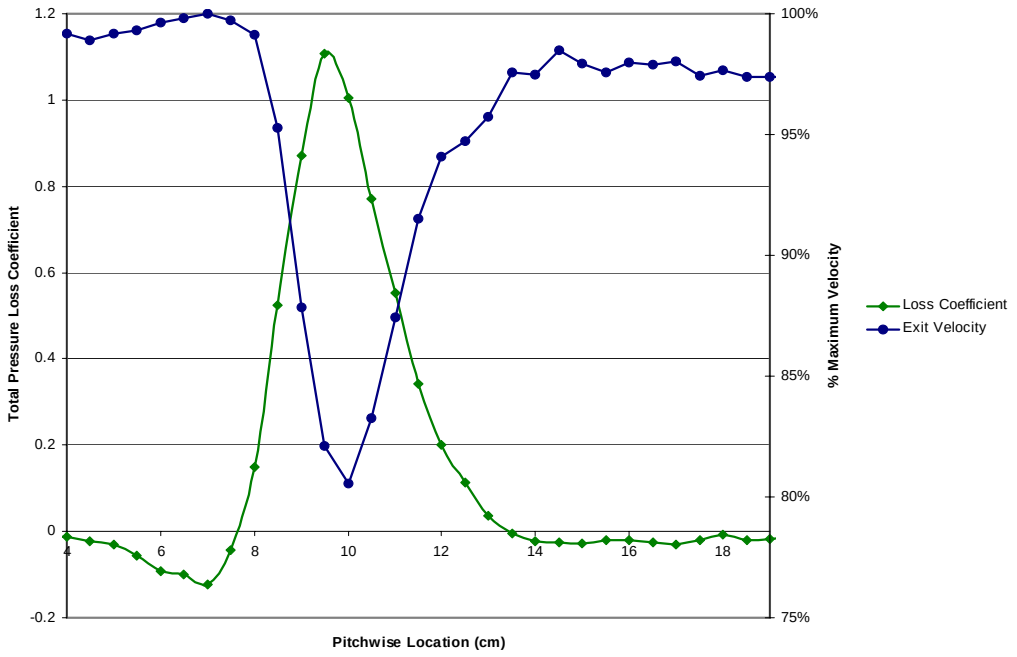

Figure 35. GH1R characterization profile for average Reynolds number of 15,551

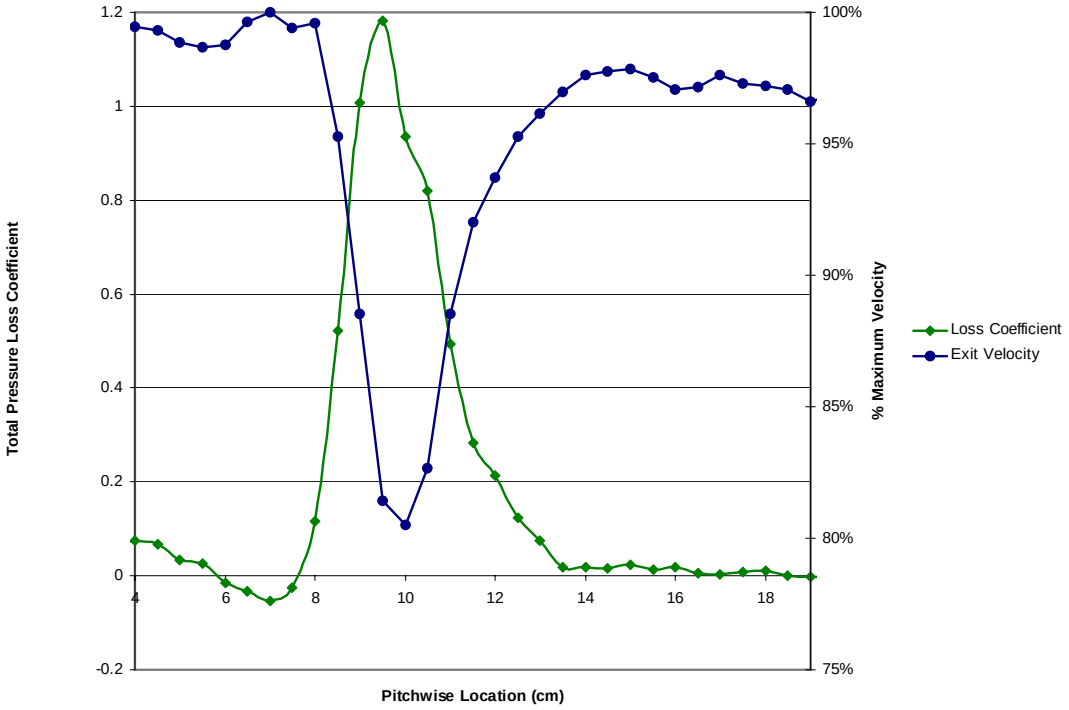

Figure 36. GH1R characterization profile for average Reynolds number of 15,787

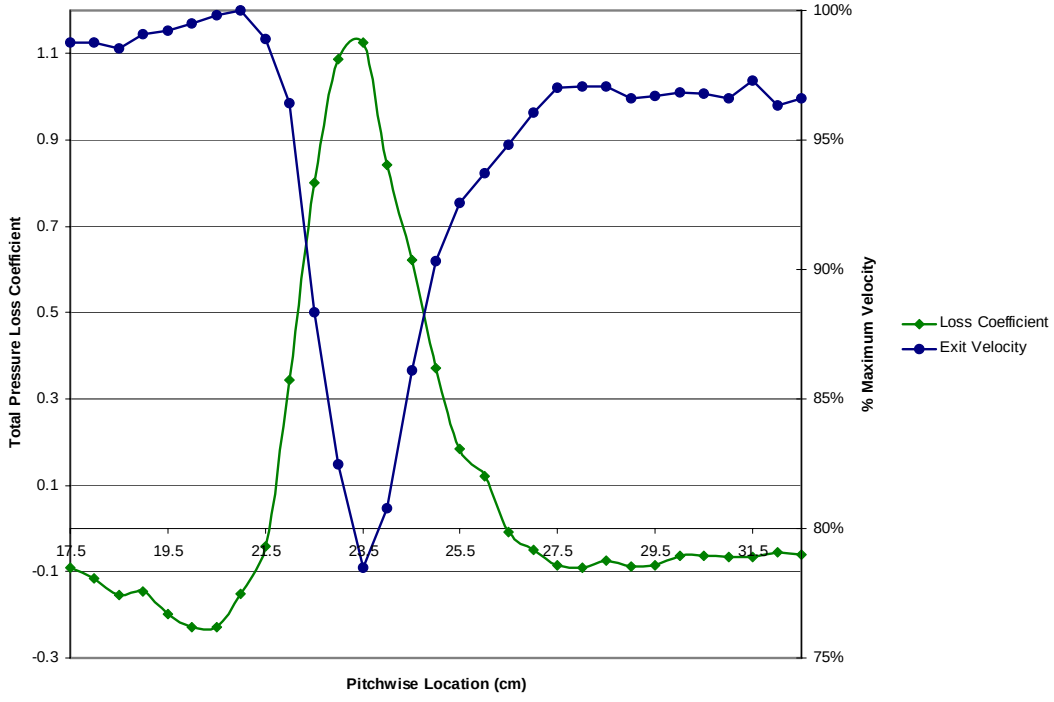

Figure 37. GH1R characterization profile for average Reynolds number of 15860

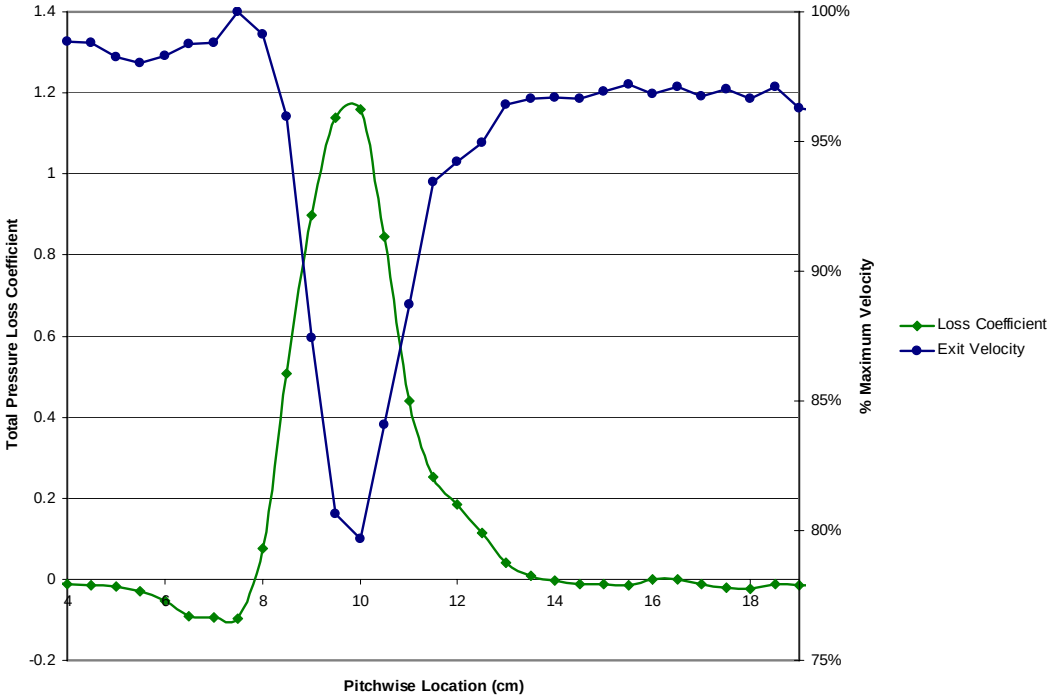

Figure 38. GH1R characterization profile for average Reynolds number of 20,152

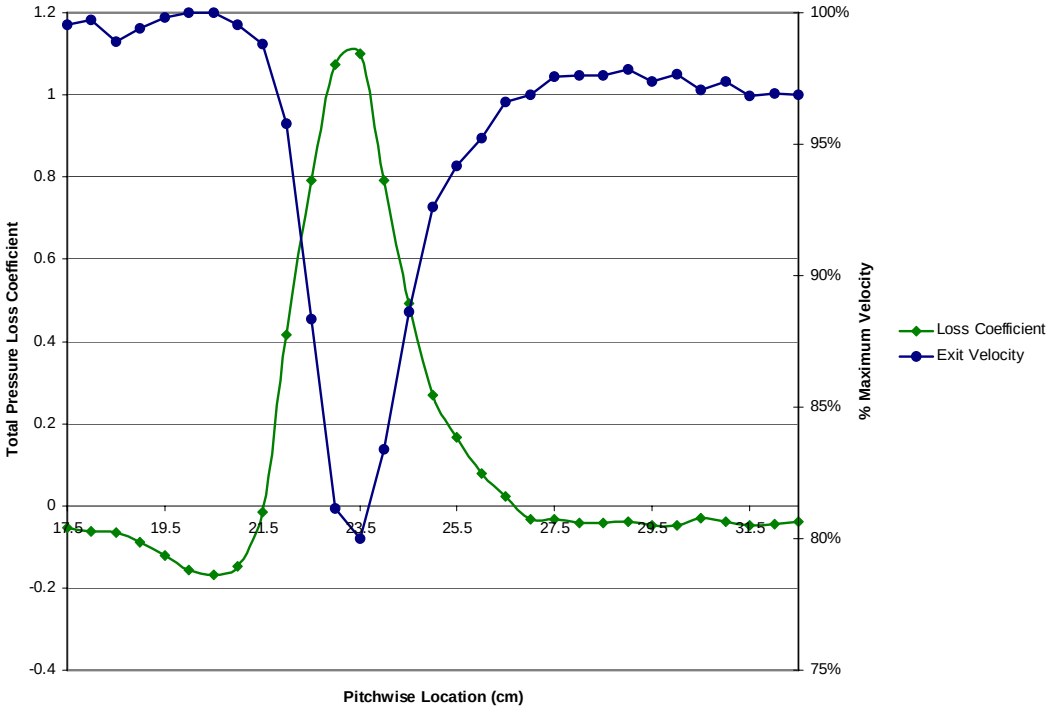

Figure 39. GH1R characterization profile for average Reynolds number of 20,583

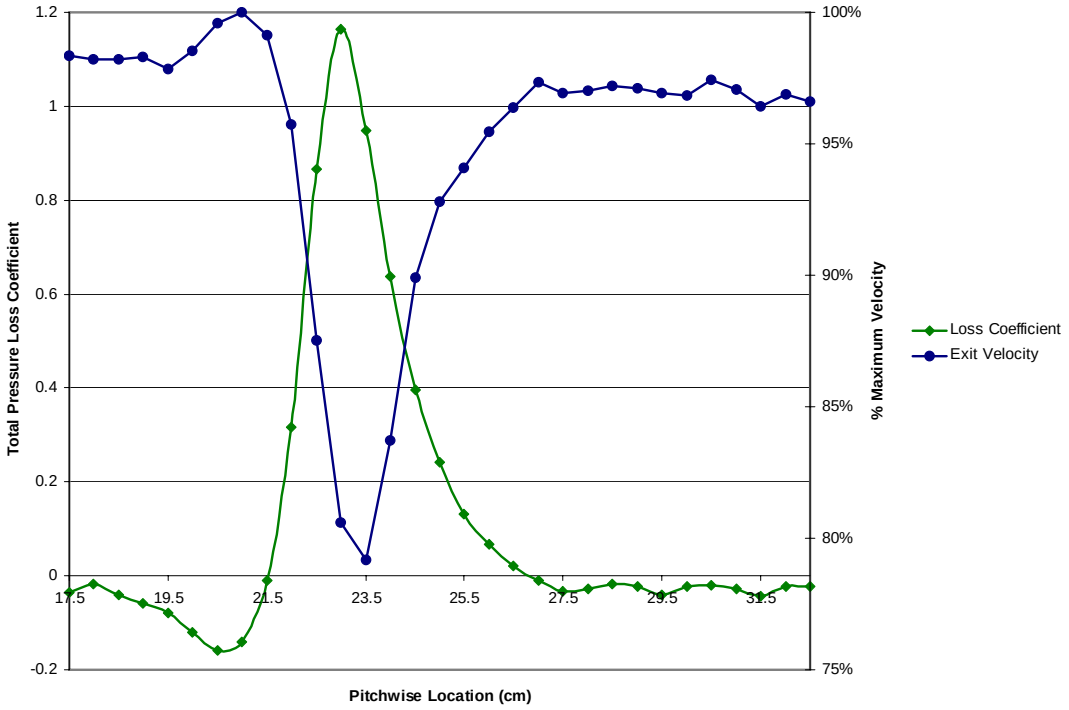

Figure 40. GH1R characterization profile for average Reynolds number of 21,273

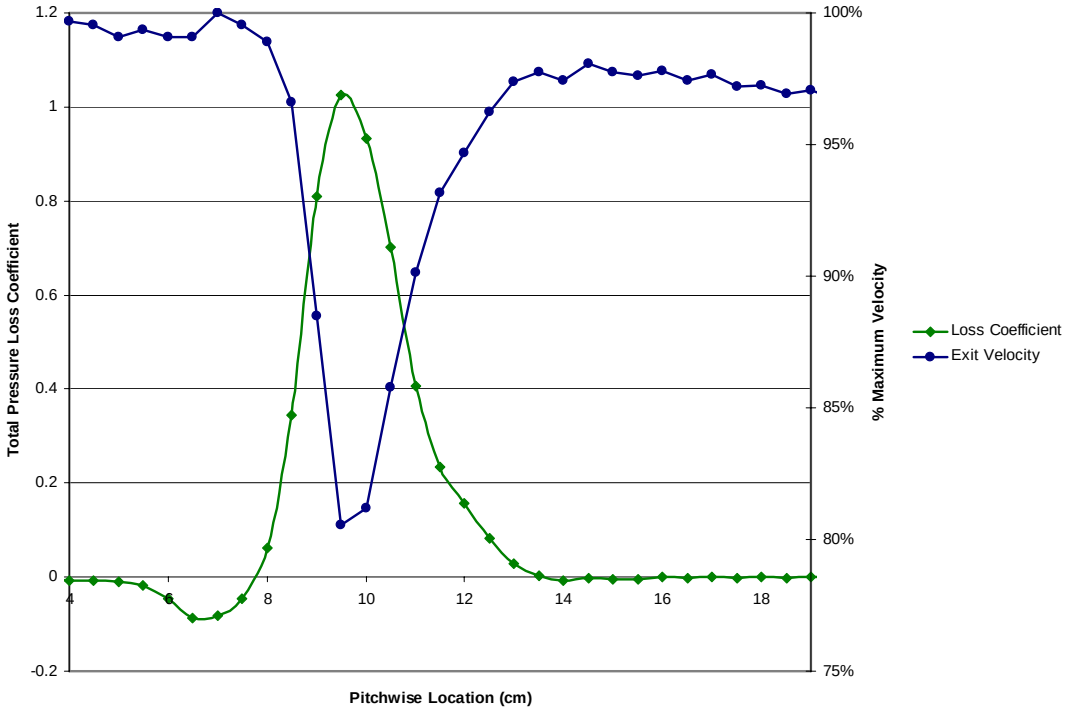

Figure 41. GH1R characterization profile for average Reynolds number of 24,739

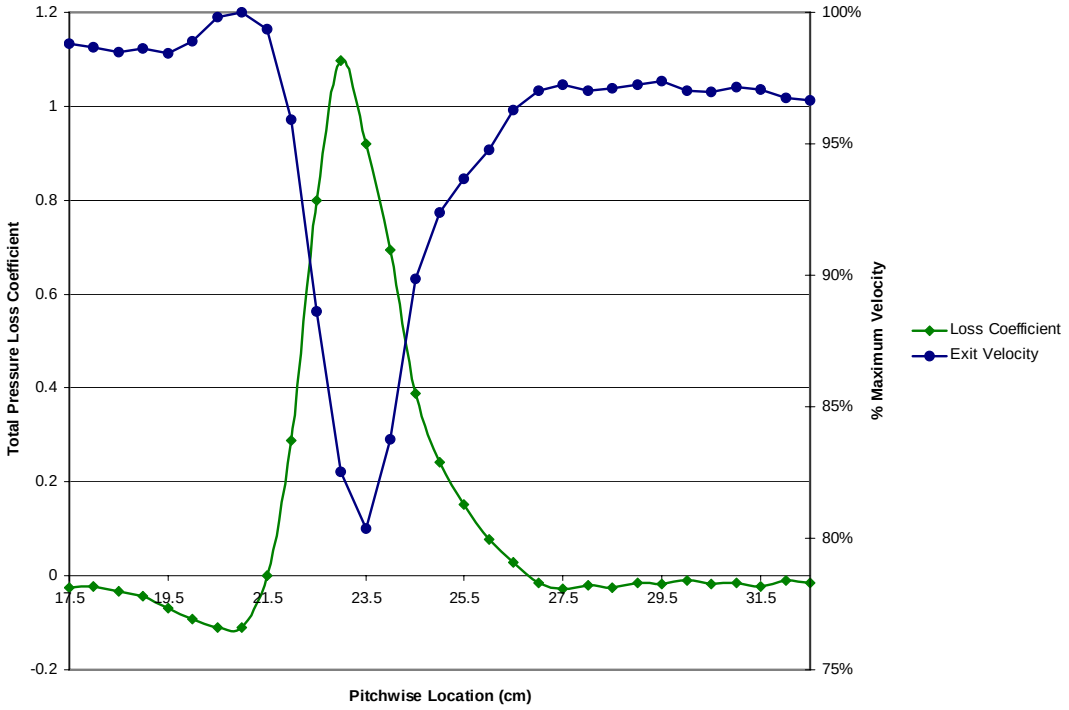

Figure 42. GH1R characterization profile for average Reynolds number of 25,212

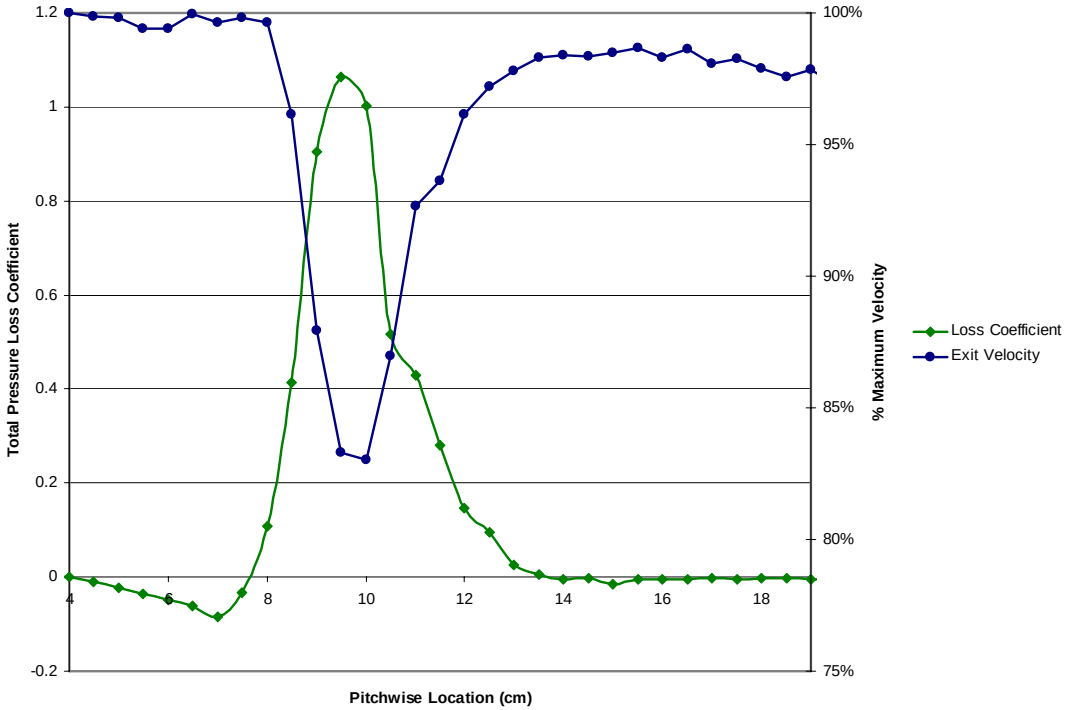

Figure 43. GH1R characterization profile for average Reynolds number of 25,478

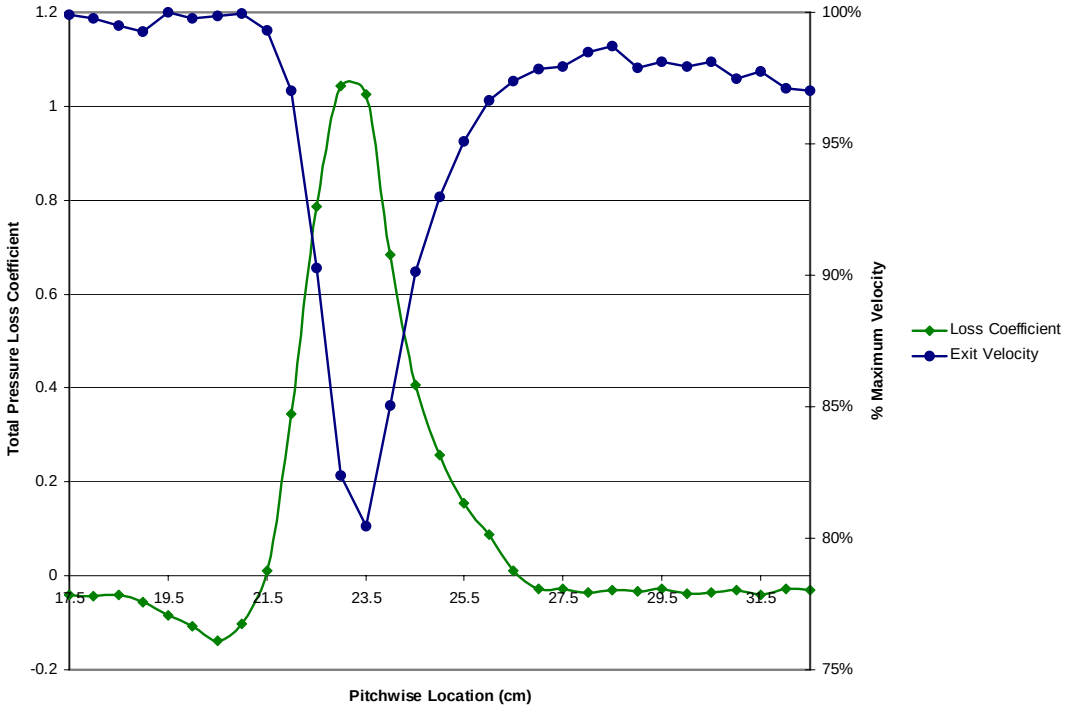

Figure 44. GH1R characterization profile for average Reynolds number of 26,934

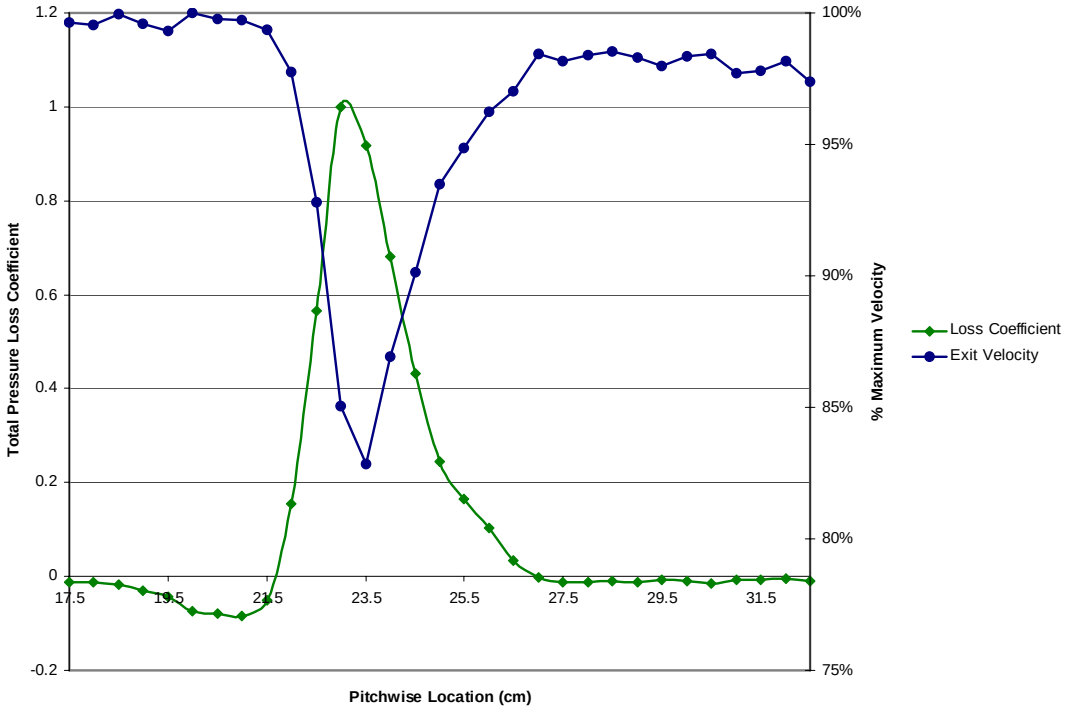

Figure 45. GH1R characterization profile for average Reynolds number of 29,182

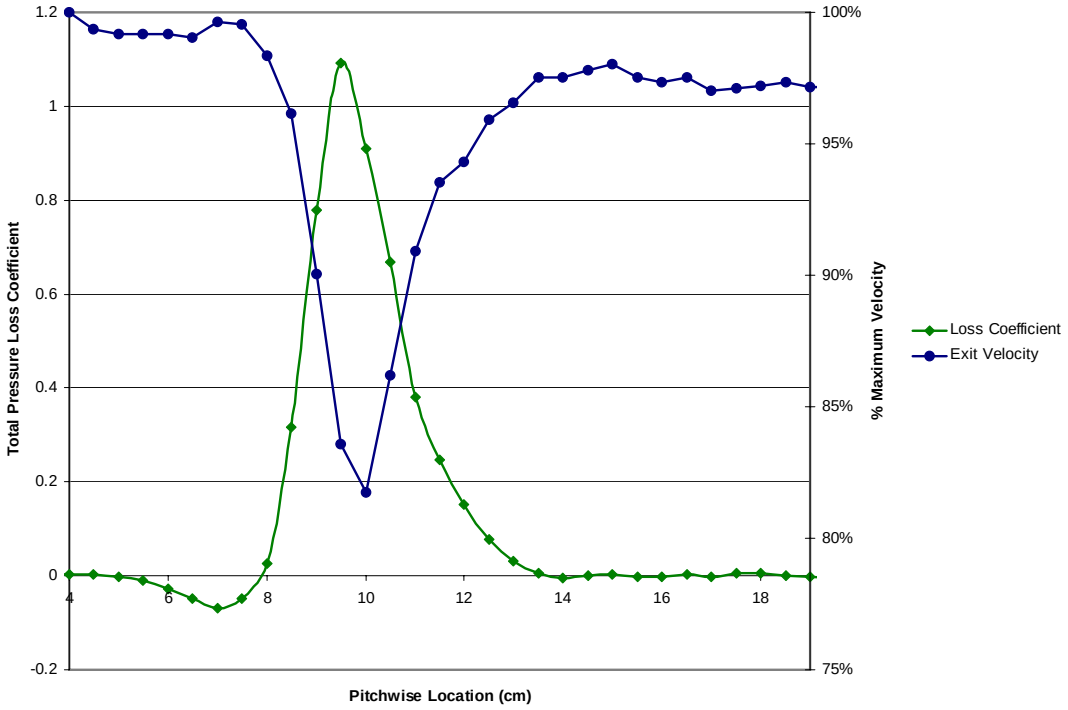

Figure 46. GH1R characterization profile for average Reynolds number of 29,776

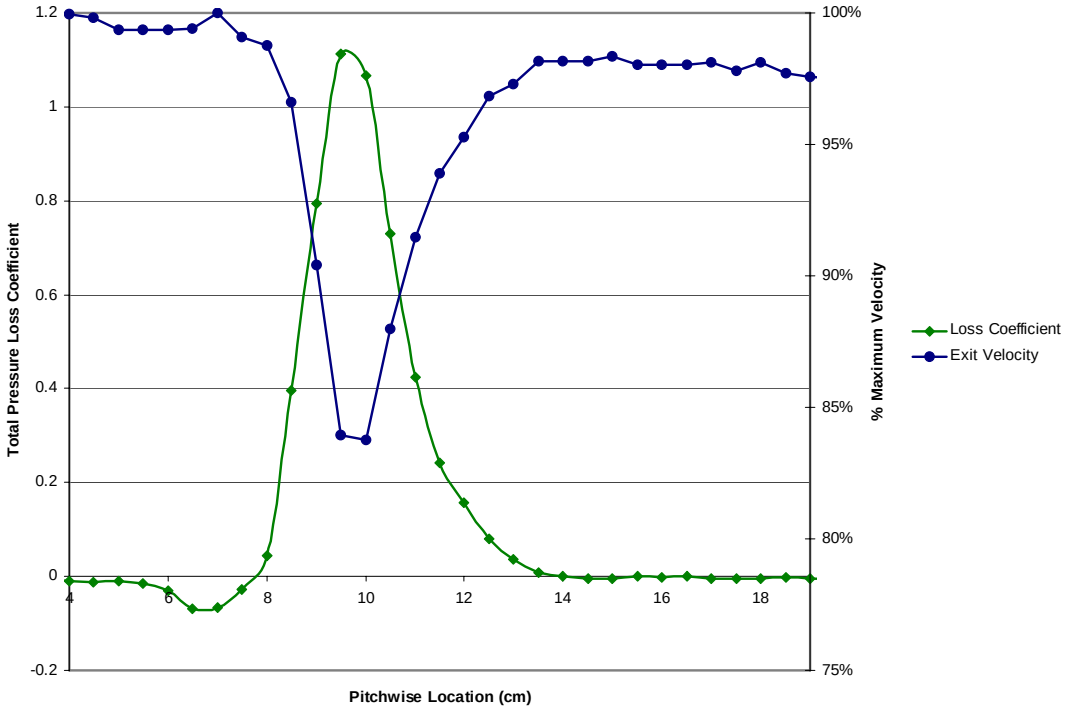

Figure 47. GH1R characterization profile for average Reynolds number of 31,302

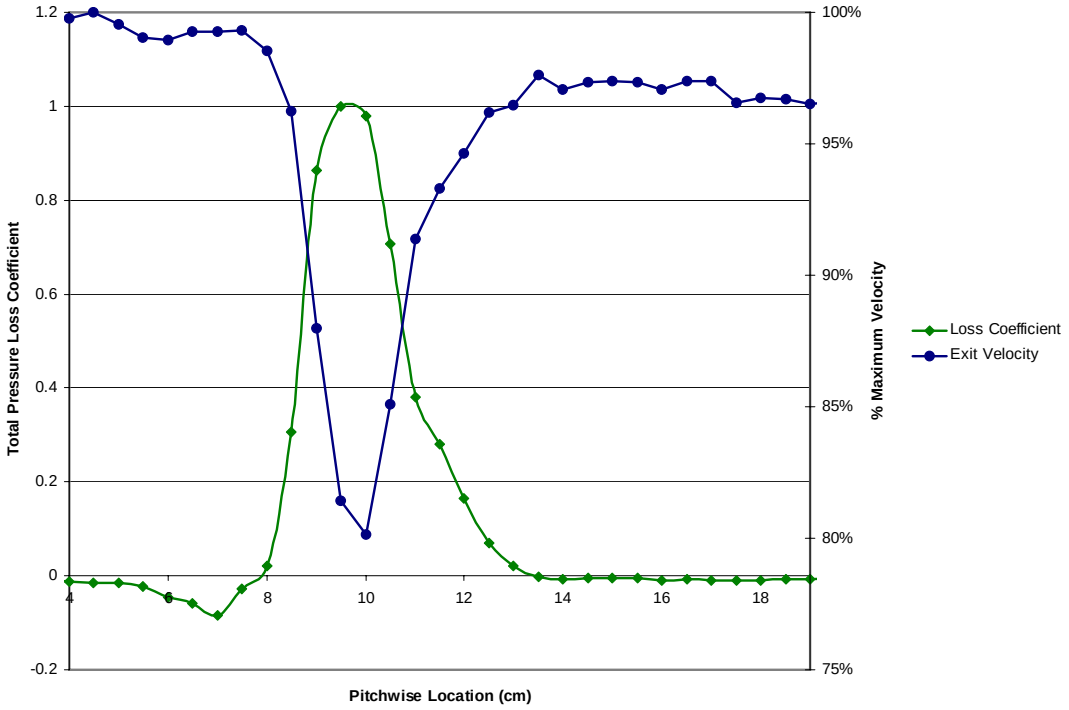

Figure 48. GH1R characterization profile for average Reynolds number of 31,655

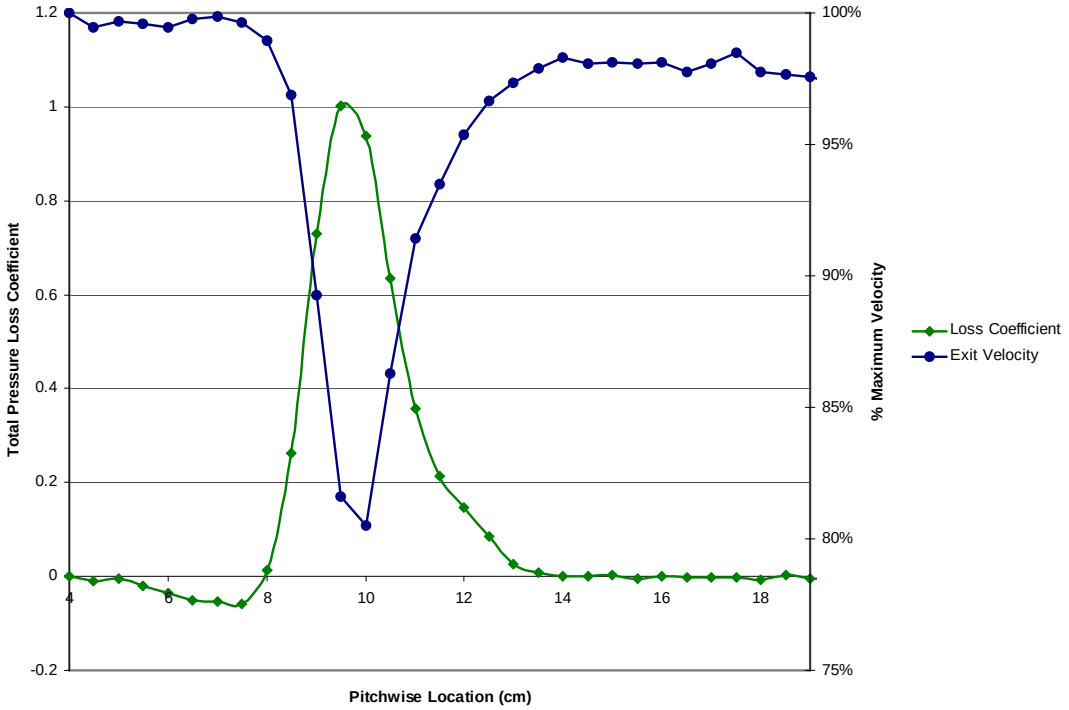

Figure 49. GH1R characterization profile for average Reynolds number of 31,942

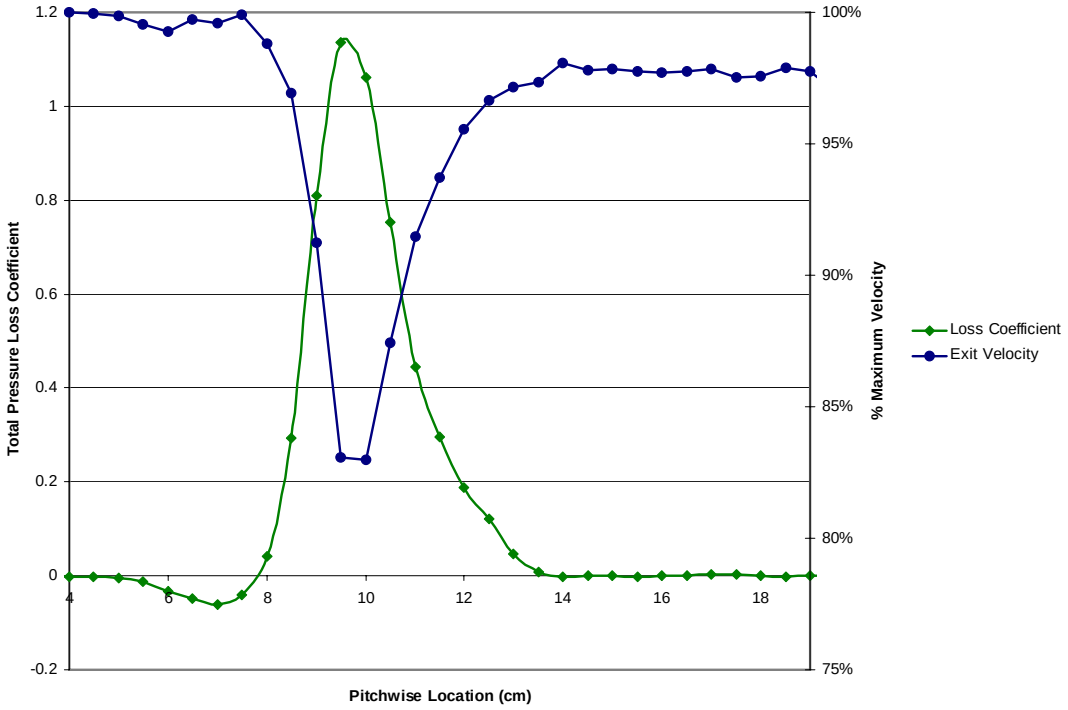

Figure 50. GH1R characterization profile for average Reynolds number of 34,216

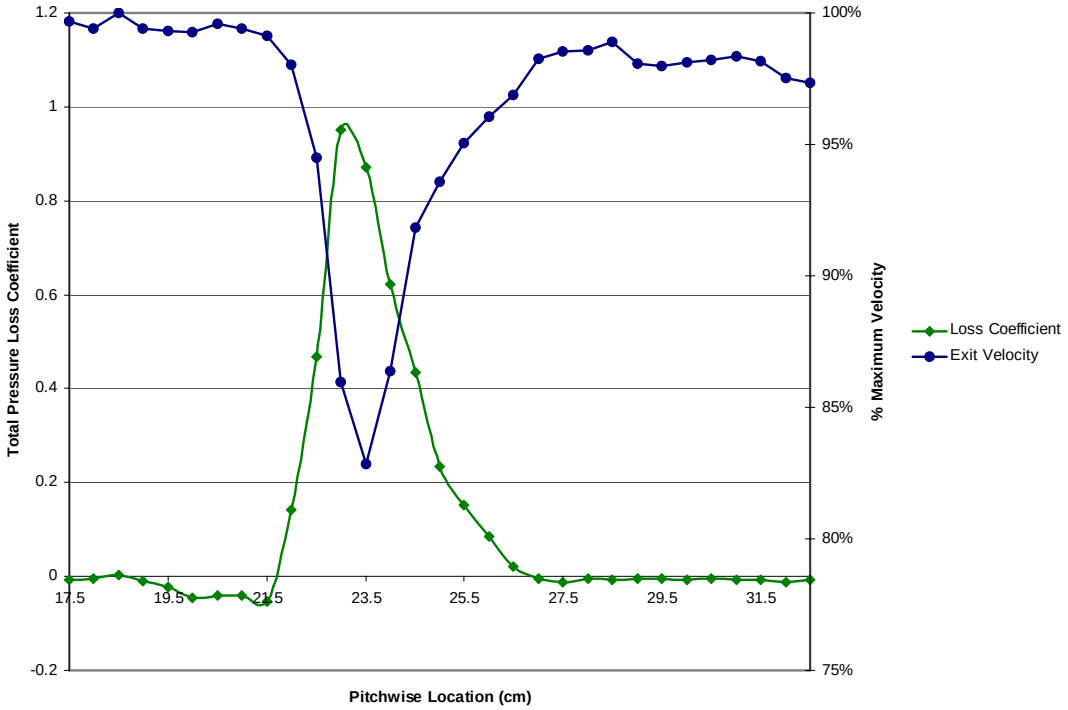

Figure 51. GH1R characterization profile for average Reynolds number of 35,584

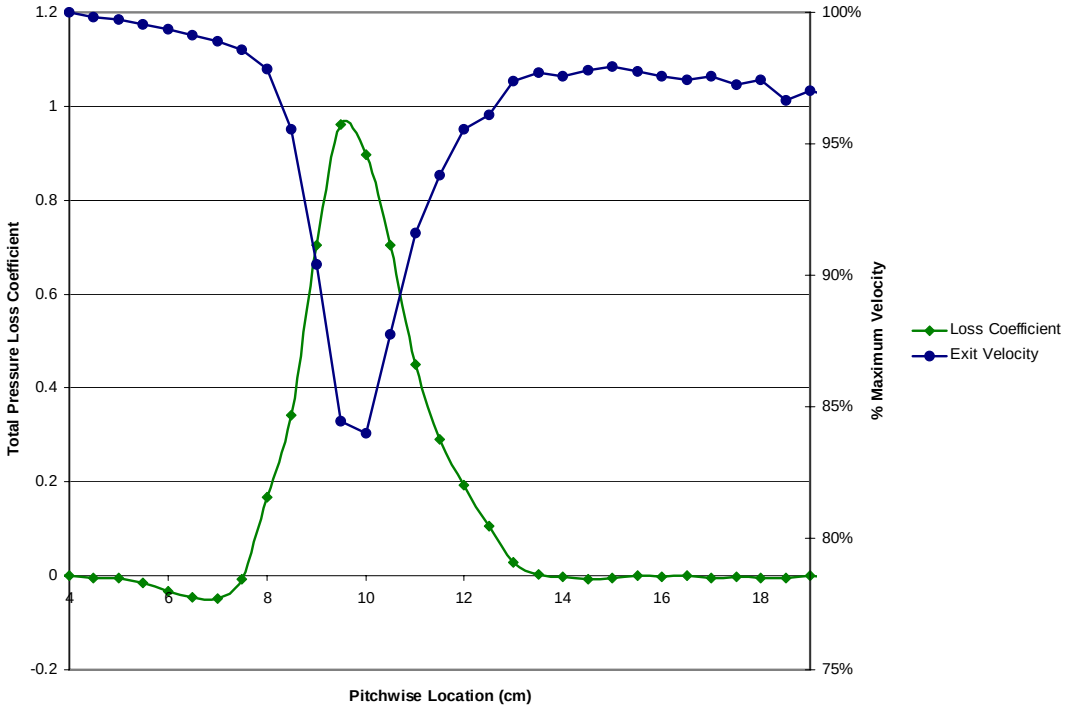

Figure 52. GH1R characterization profile for average Reynolds number of 36,244

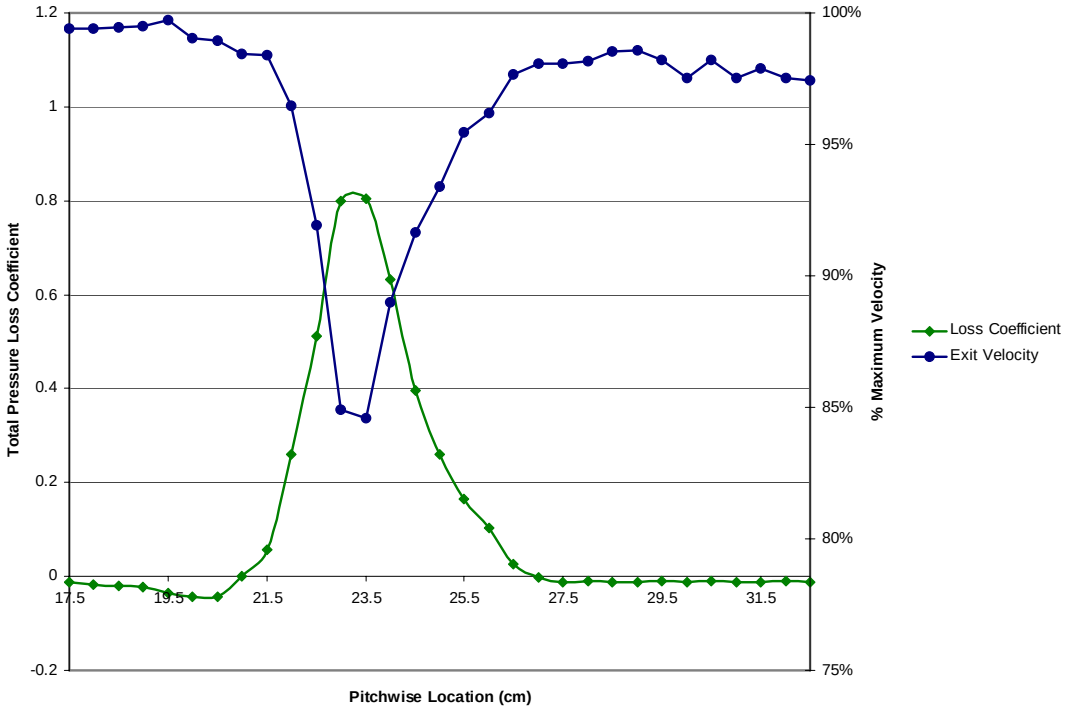

Figure 53. GH1R characterization profile for average Reynolds number of 39,059

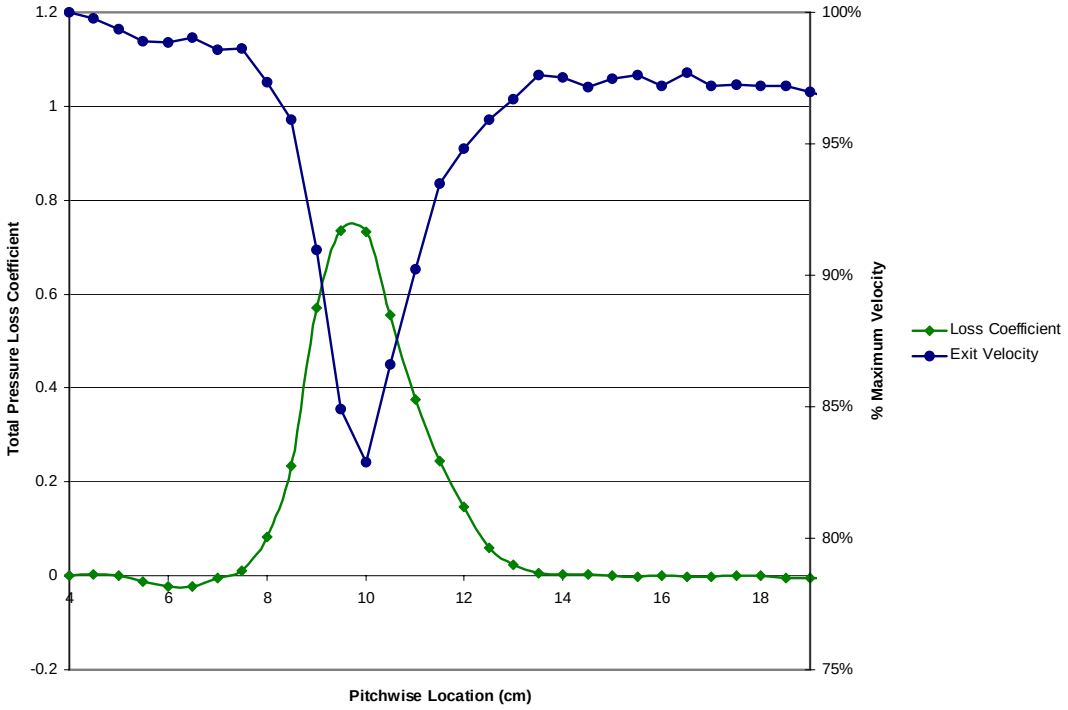

Figure 54. GH1R characterization profile for average Reynolds number of 40,002

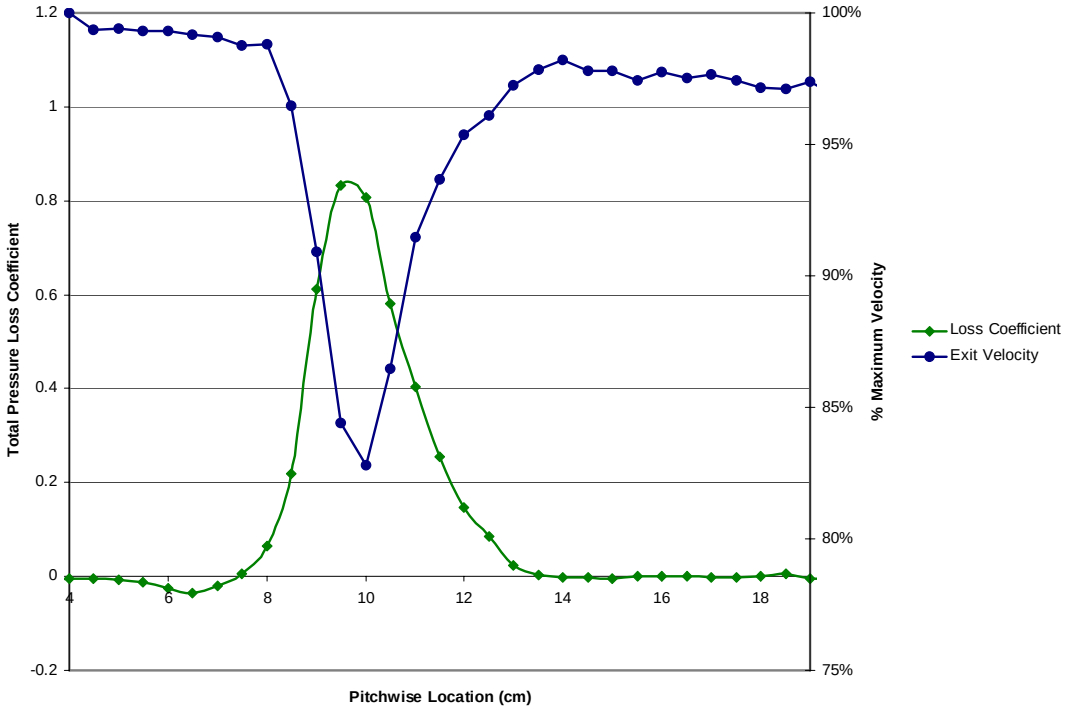

Figure 55. GH1R characterization profile for average Reynolds number of 41,203

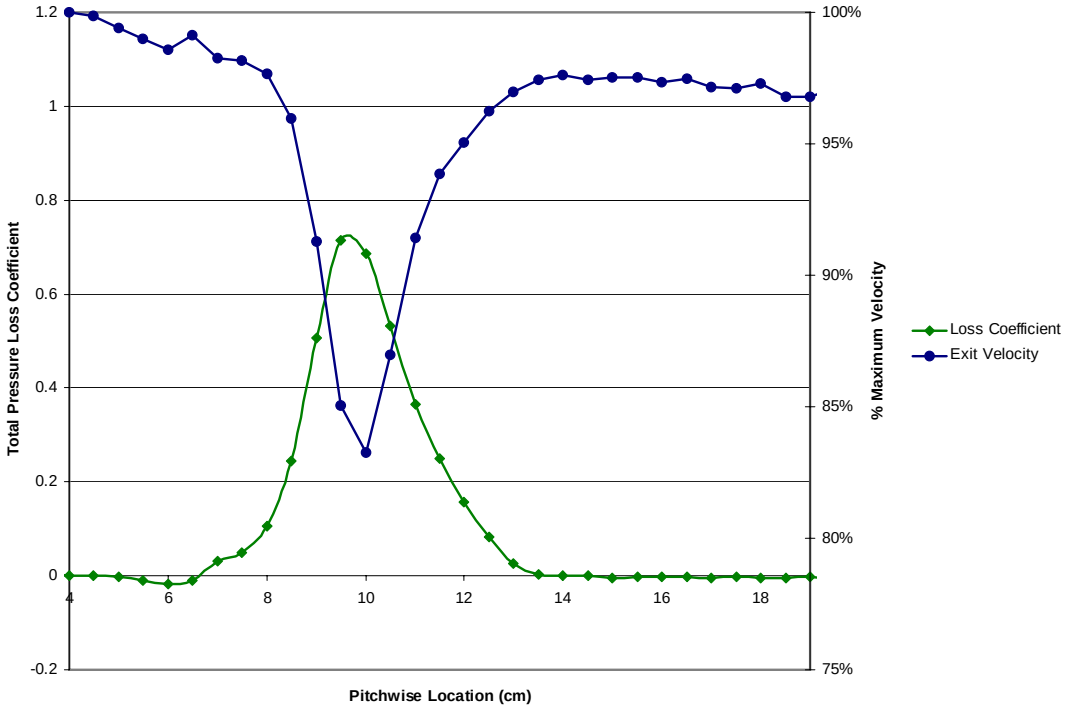

Figure 56. GH1R characterization profile for average Reynolds number of 45,237

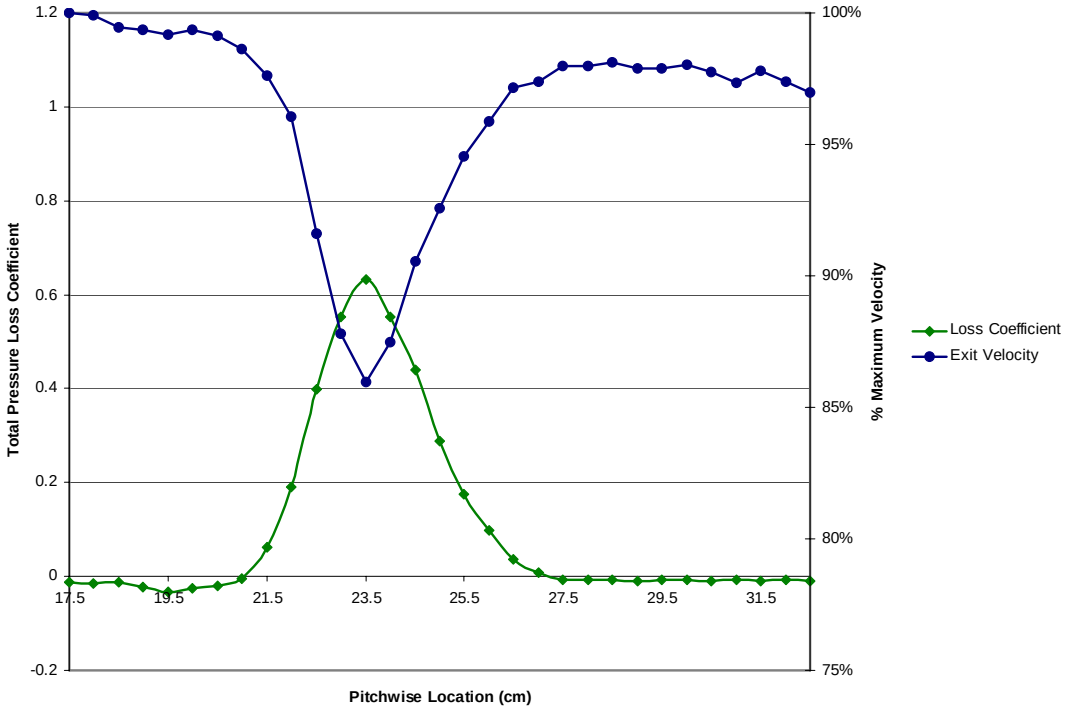

Figure 57. GH1R characterization profile for average Reynolds number of 46,523

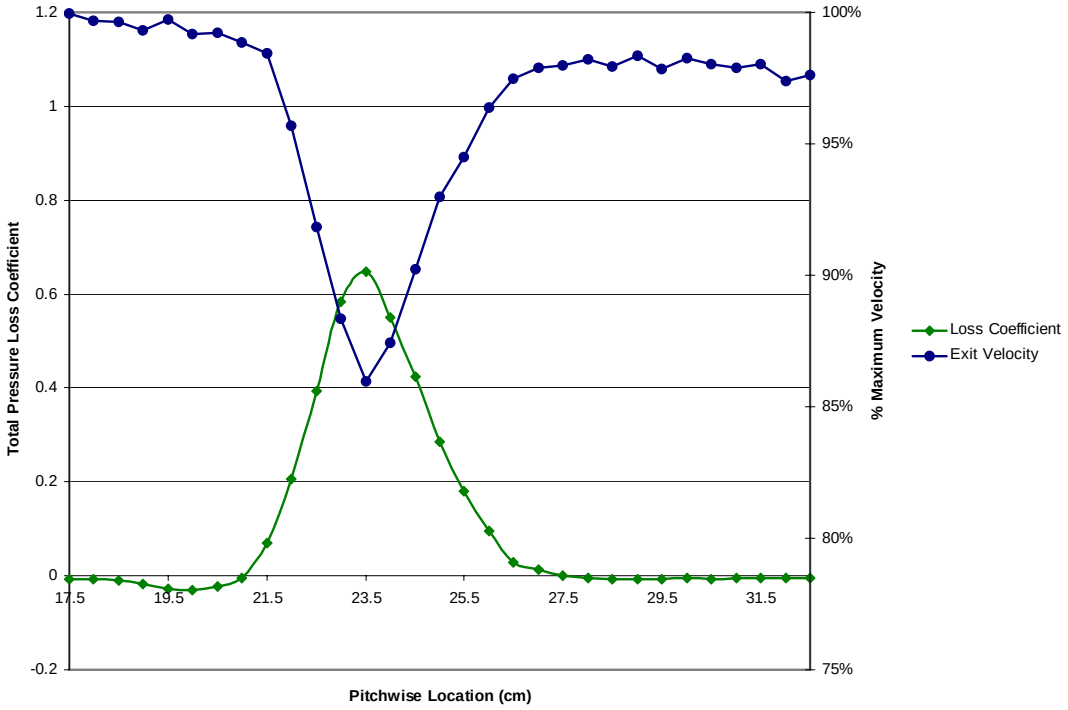

Figure 58. GH1R characterization profile for average Reynolds number of 47,607

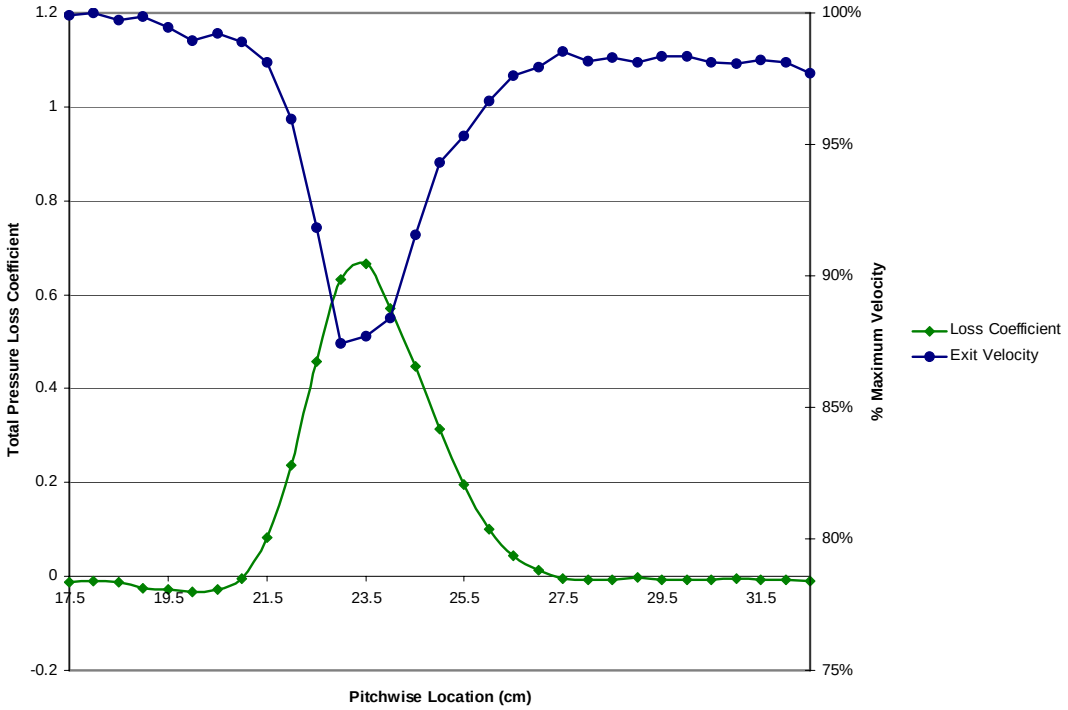

Figure 59. GH1R characterization profile for average Reynolds number of 49,969

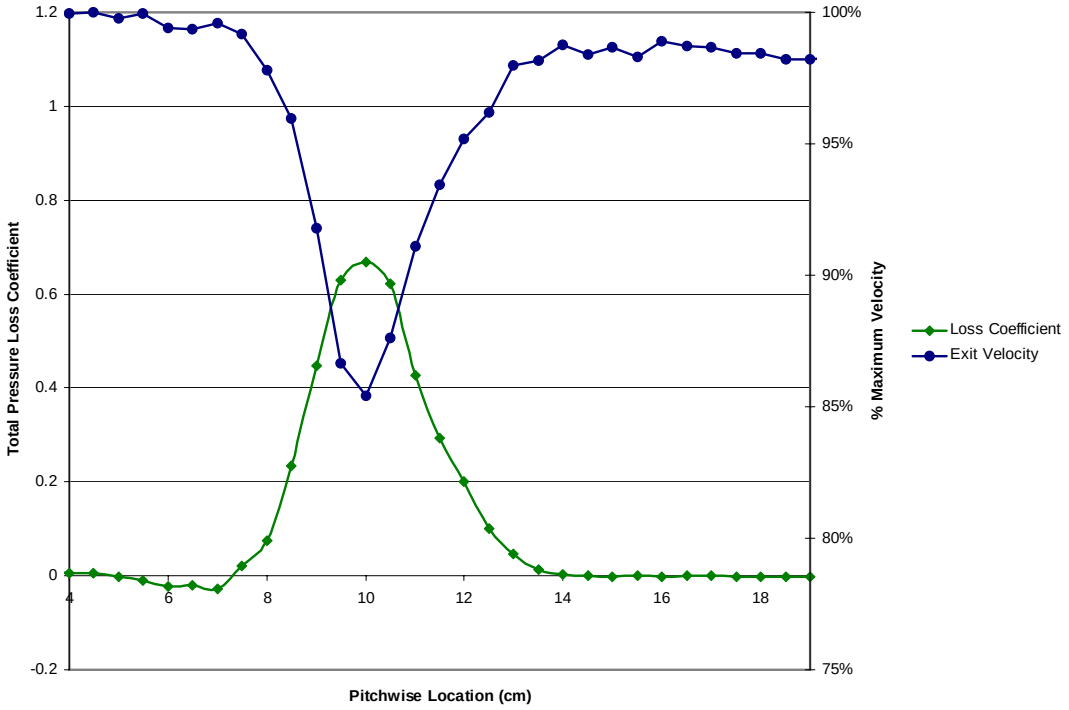

Figure 60. GH1R characterization profile for average Reynolds number of 50,489

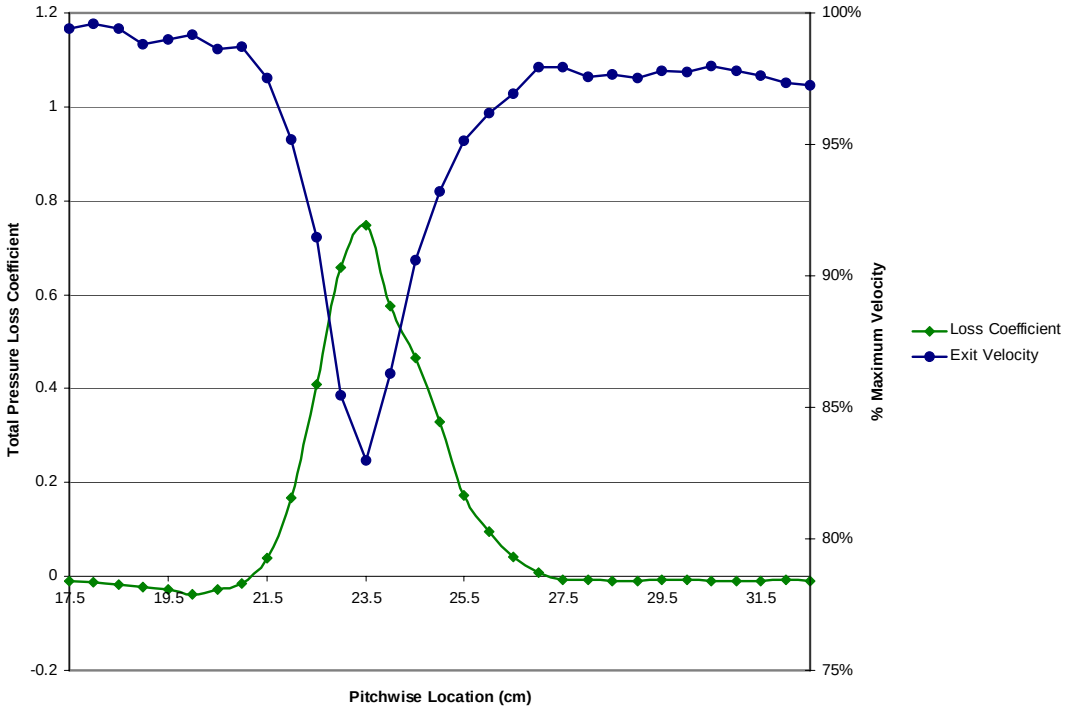

Figure 61. GH1R characterization profile for average Reynolds number of 51,682

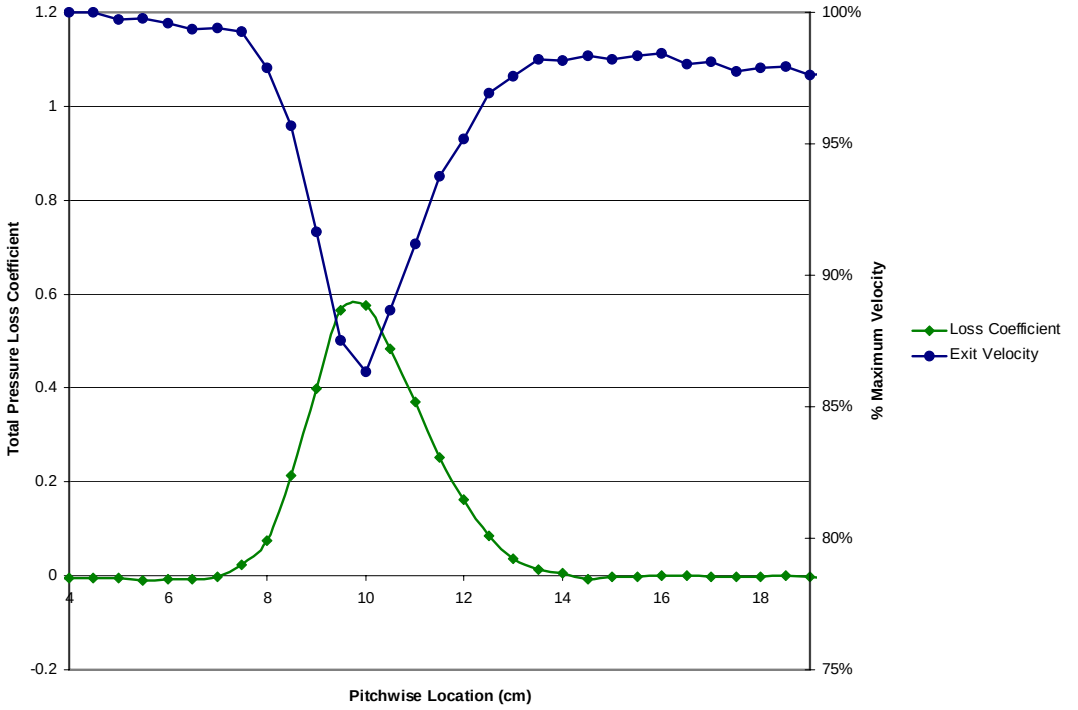

Figure 62. GH1R characterization profile for average Reynolds number of 52,012

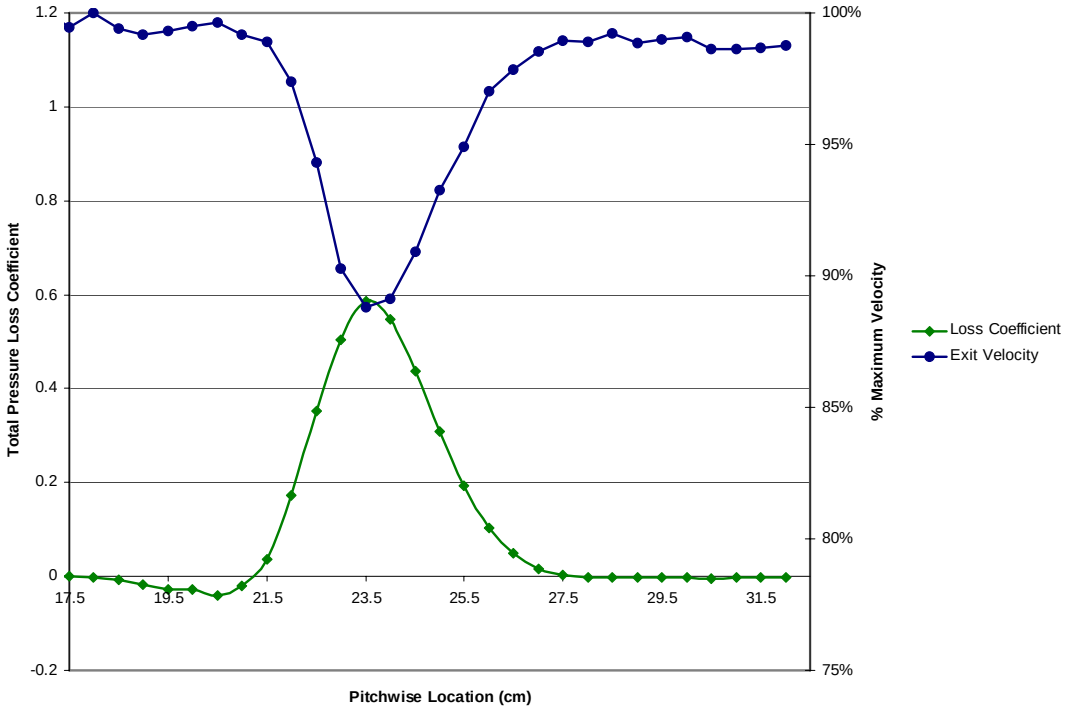

Figure 63. GH1R characterization profile for average Reynolds number of 52,631

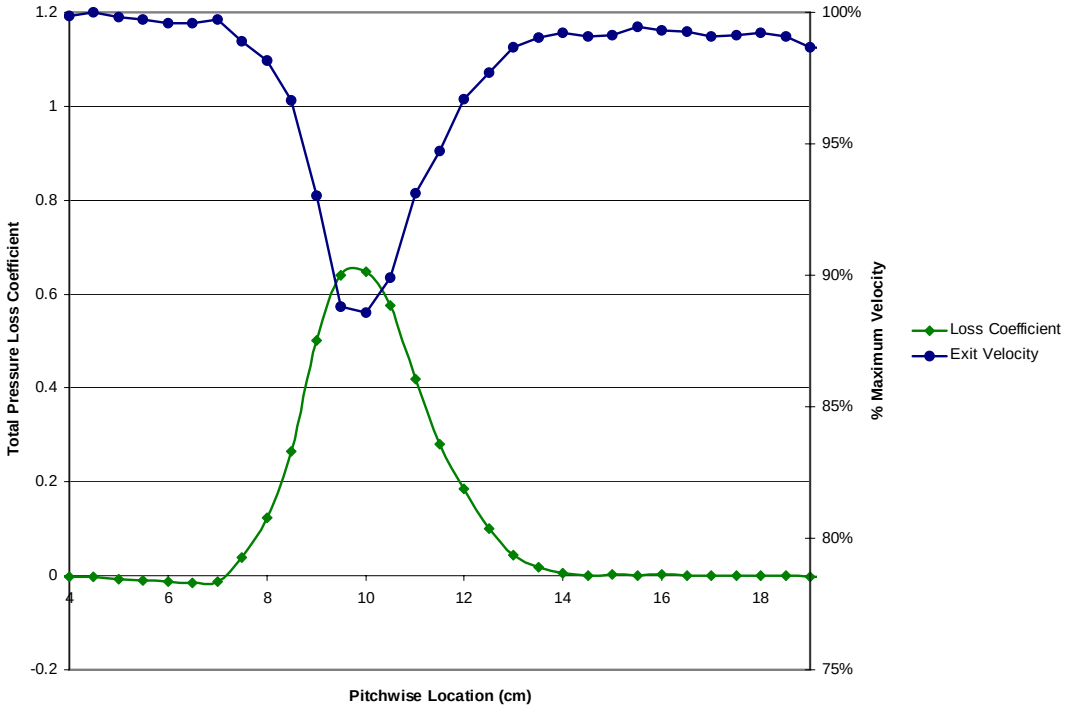

Figure 64. GH1R characterization profile for average Reynolds number of 53,104

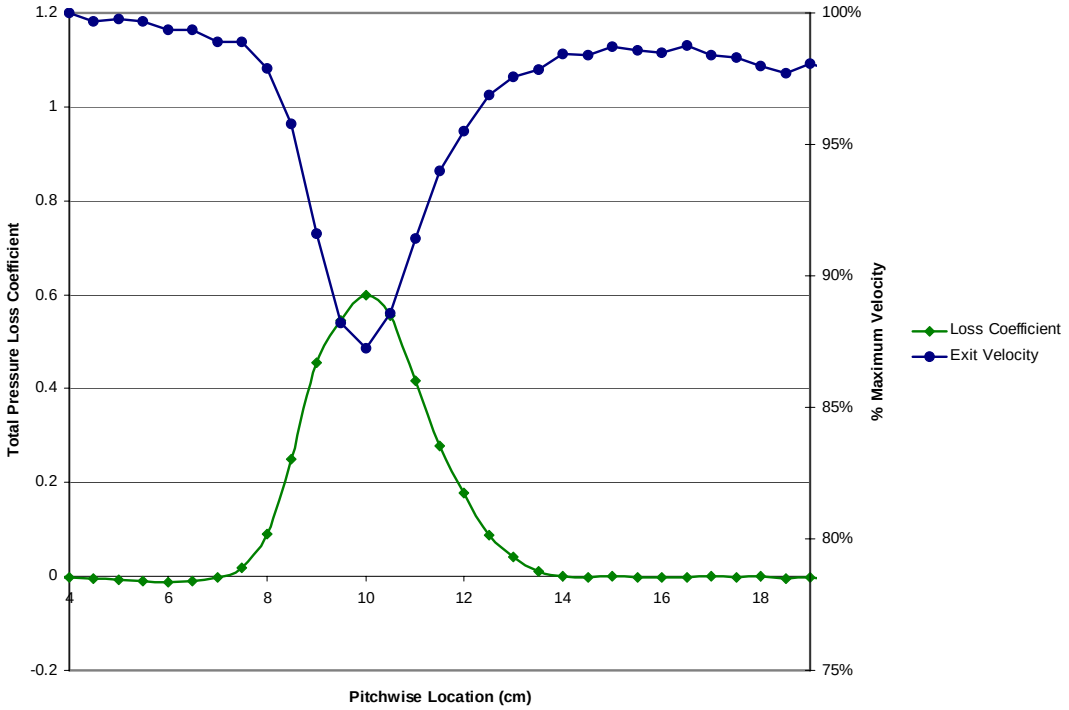

Figure 65. GH1R characterization profile for average Reynolds number of 55,886

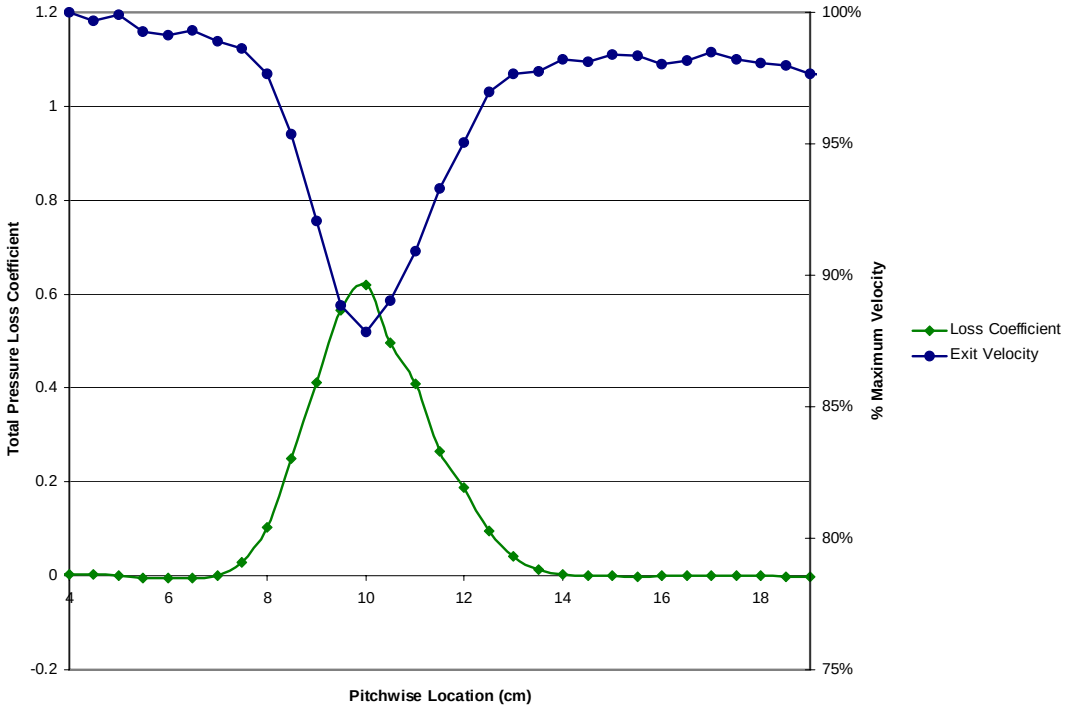

Figure 66. GH1R characterization profile for average Reynolds number of 56,038

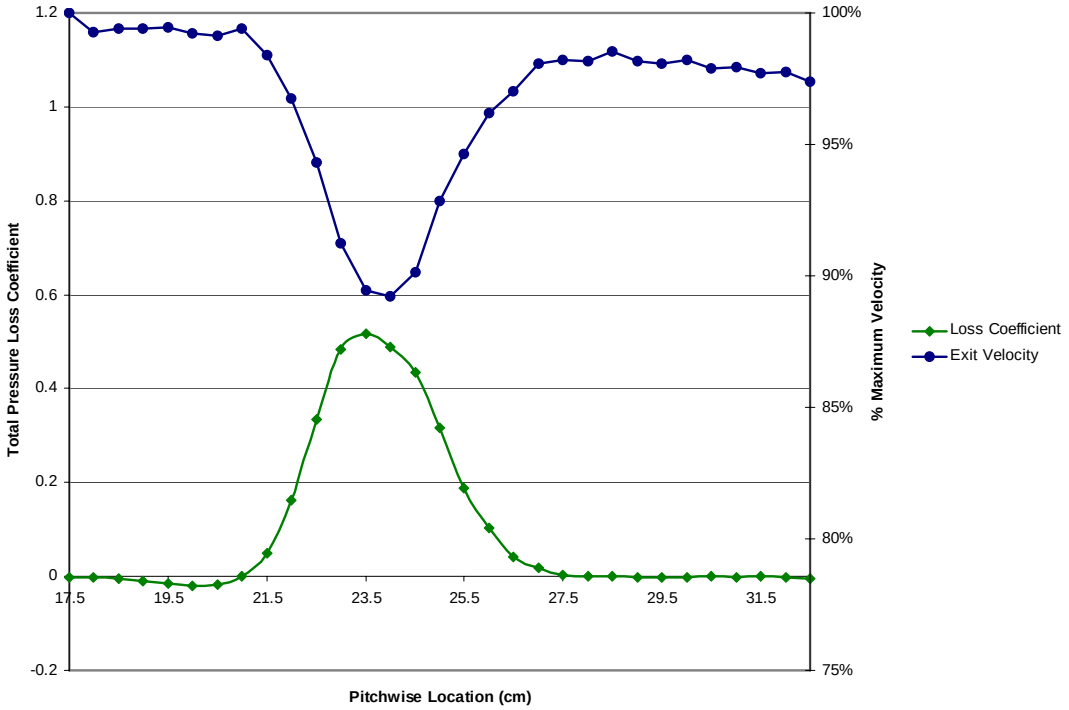

Figure 67. GH1R characterization profile for average Reynolds number of 57,812

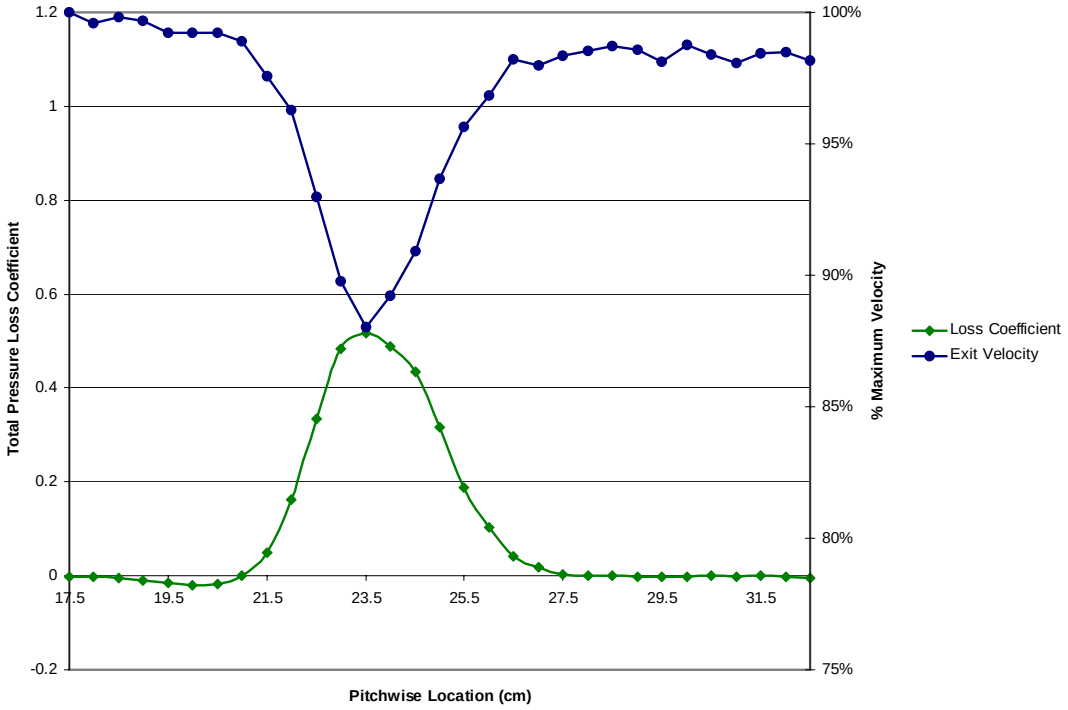

Figure 68. GH1R characterization profile for average Reynolds number of 58,834

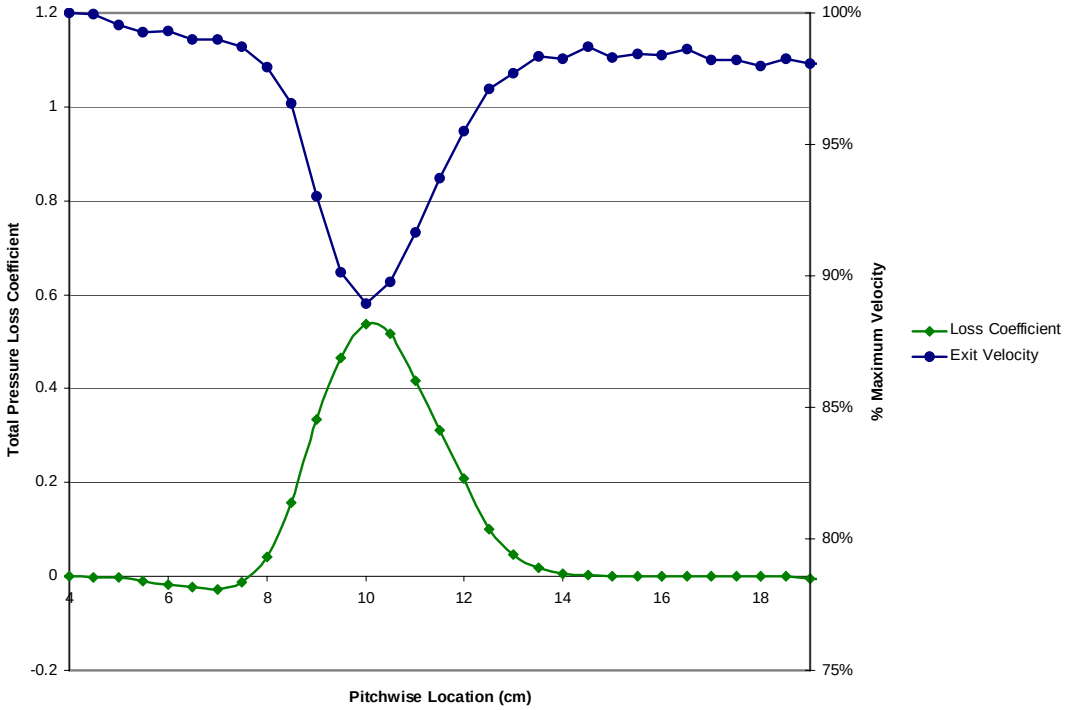

Figure 69. GH1R characterization profile for average Reynolds number of 62,775

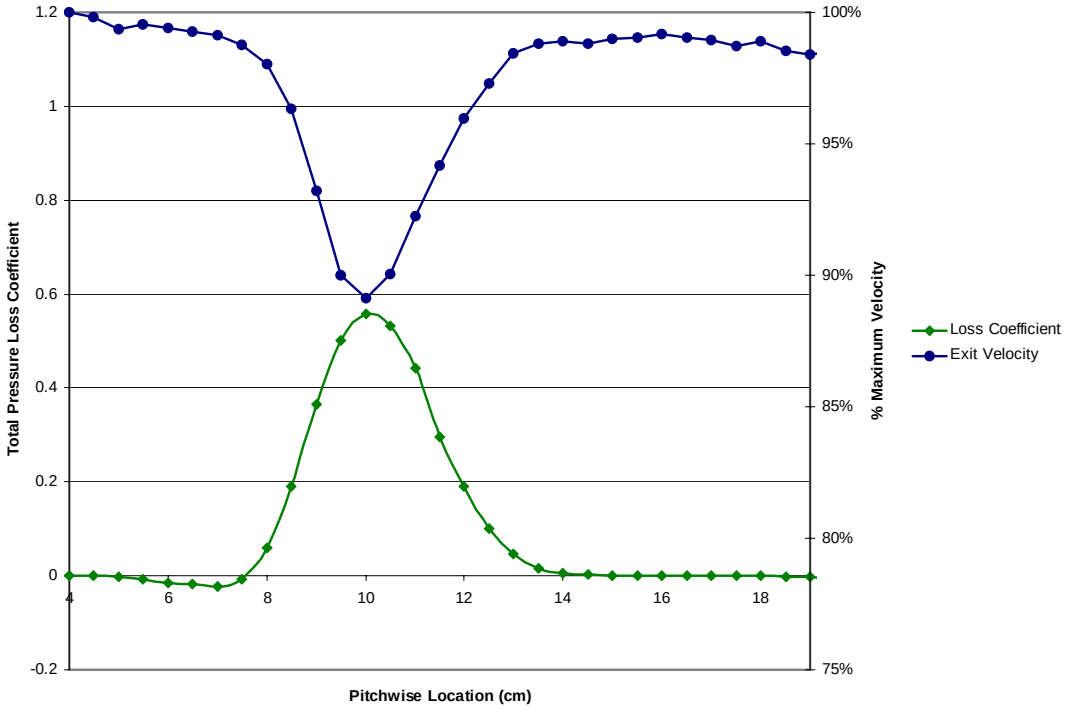

Figure 70. GH1R characterization profile for average Reynolds number of 62,857

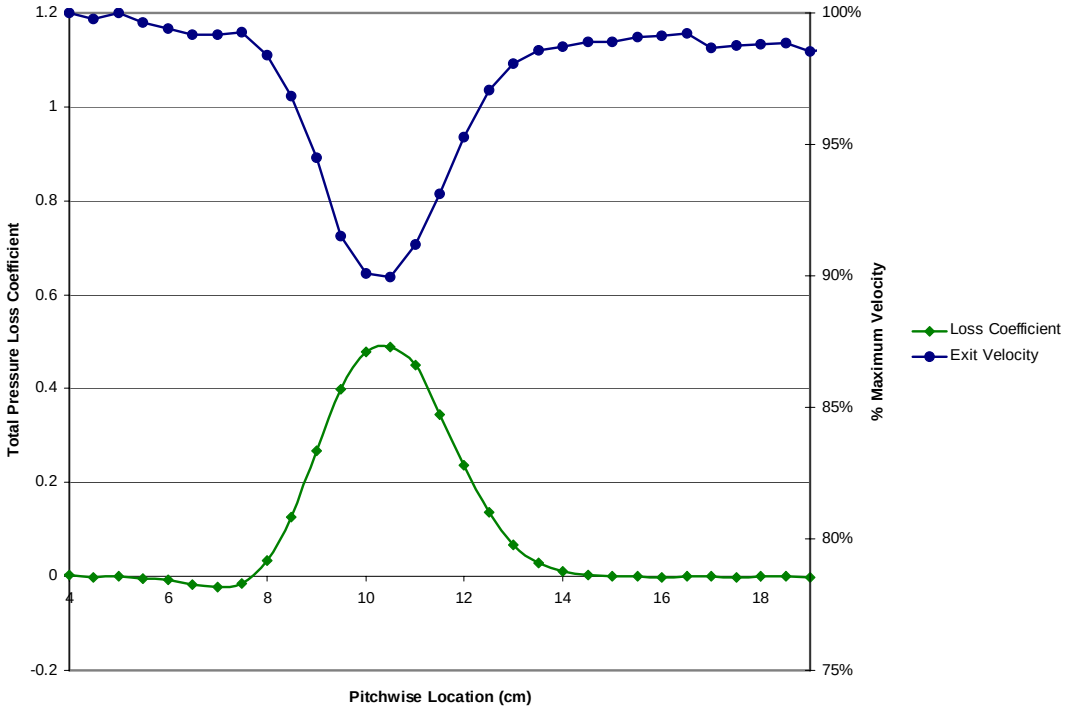

Figure 71. GH1R characterization profile for average Reynolds number of 63,261

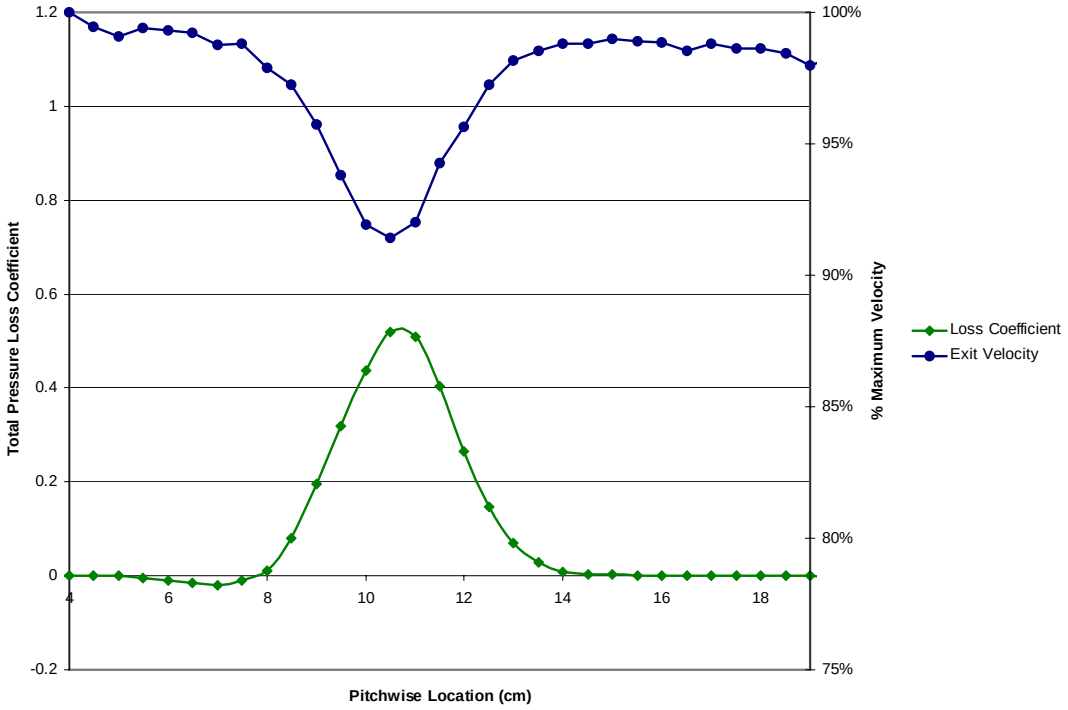

Figure 72. GH1R characterization profile for average Reynolds number of 72,839

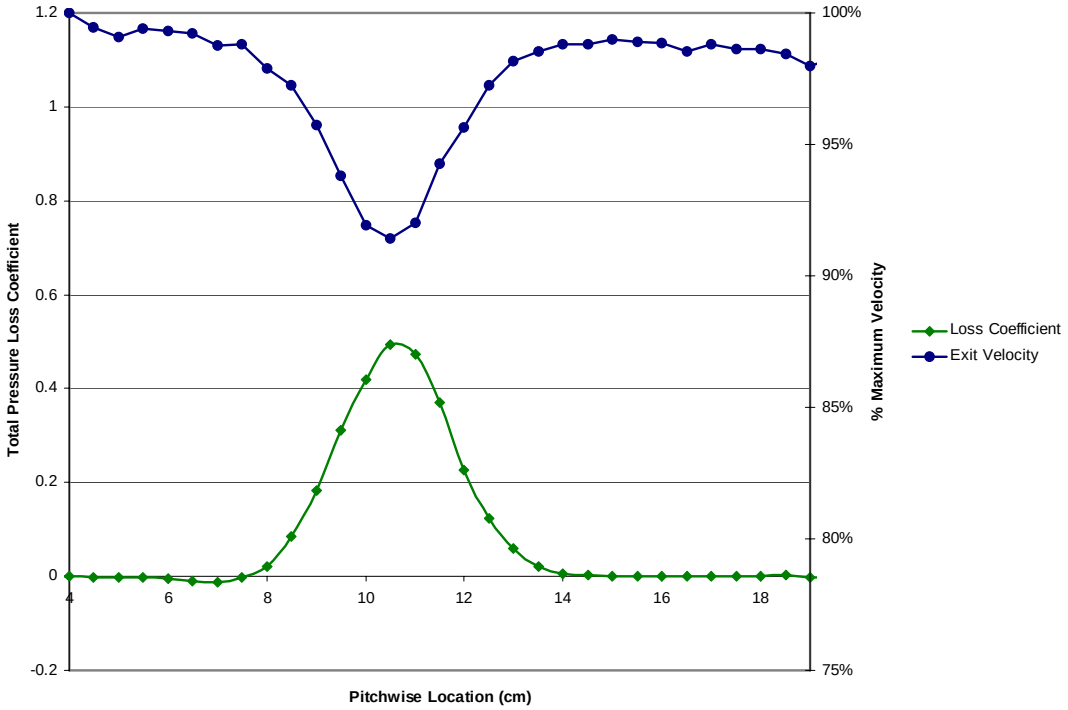

Figure 73. GH1R characterization profile for average Reynolds number of 73,453

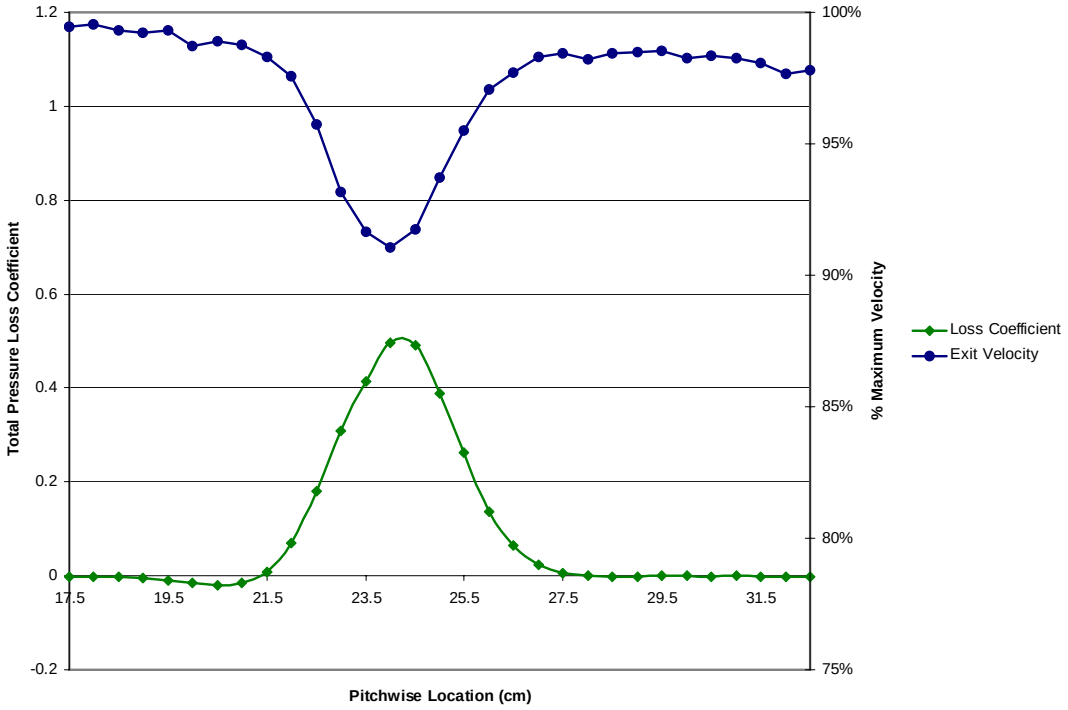

Figure 74. GH1R characterization profile for average Reynolds number of 75,418

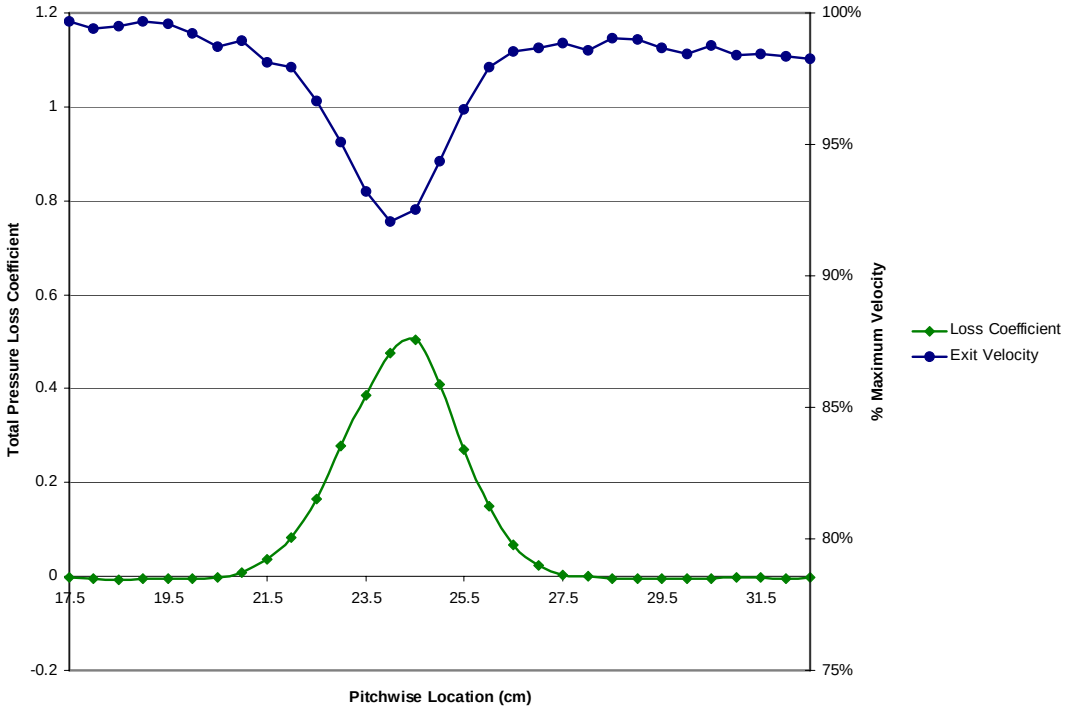

Figure 75. GH1R characterization profile for average Reynolds number of 75,686

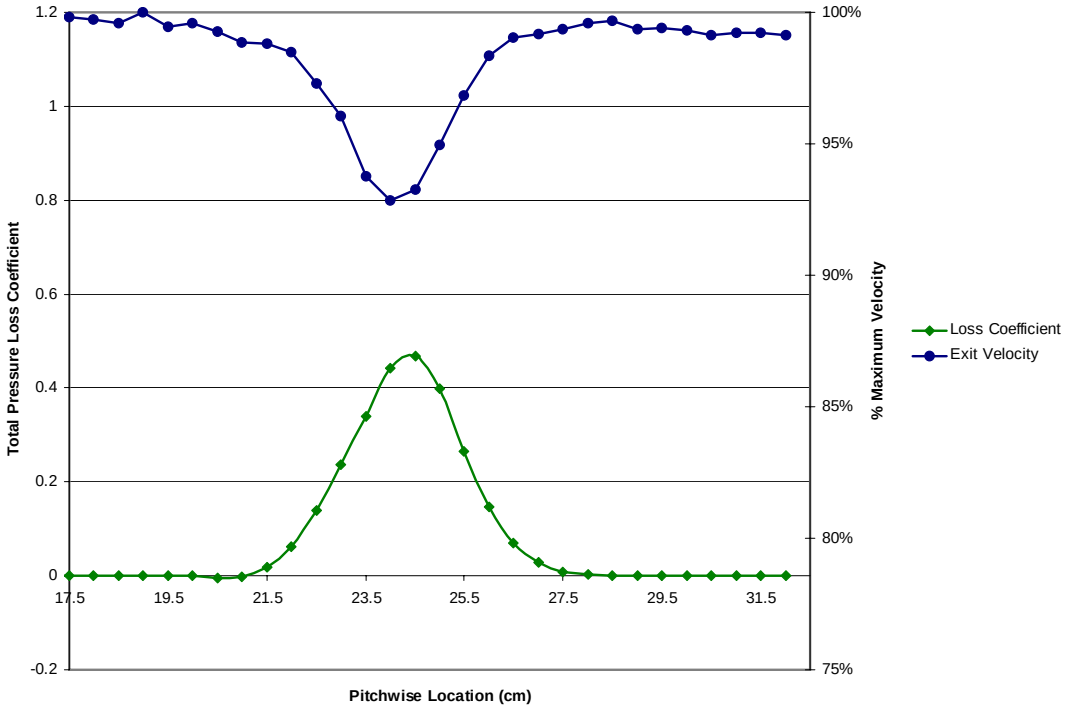

Figure 76. GH1R characterization profile for average Reynolds number of 76,617

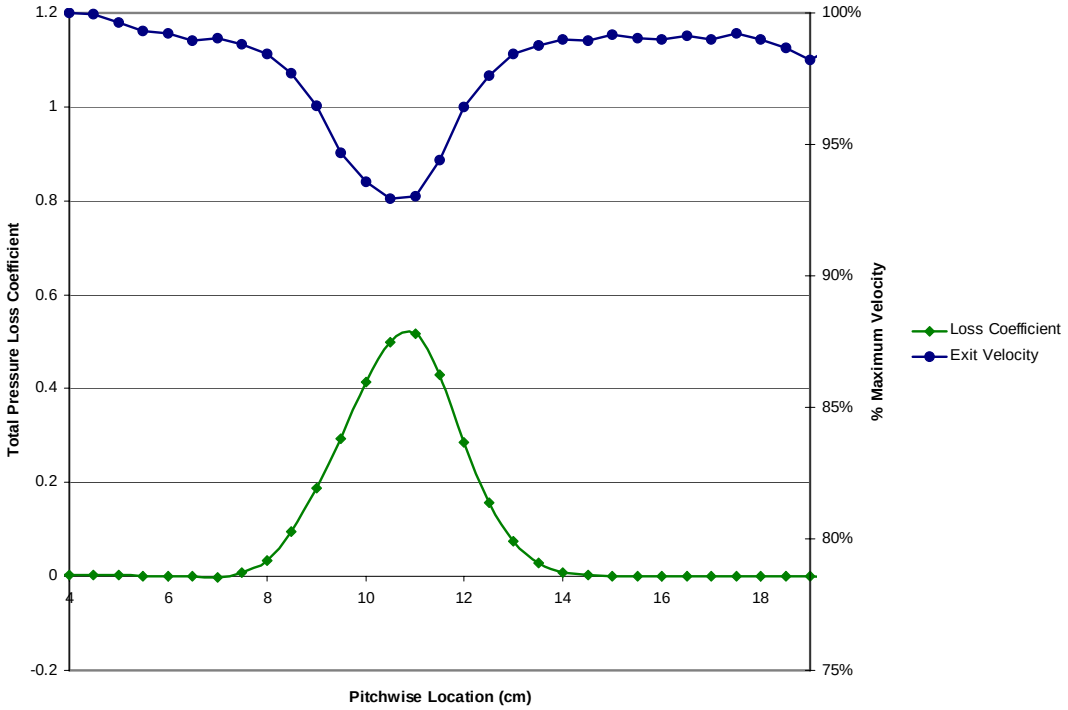

Figure 77. GH1R characterization profile for average Reynolds number of 81,606

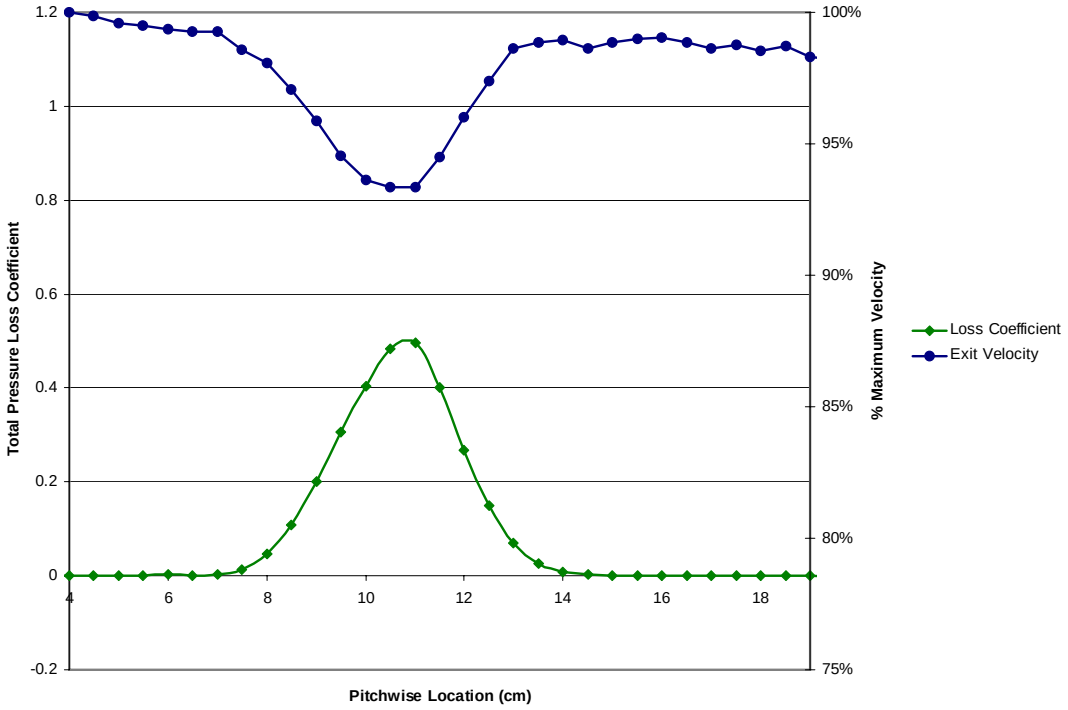

Figure 78. GH1R characterization profile for average Reynolds number of 83,016

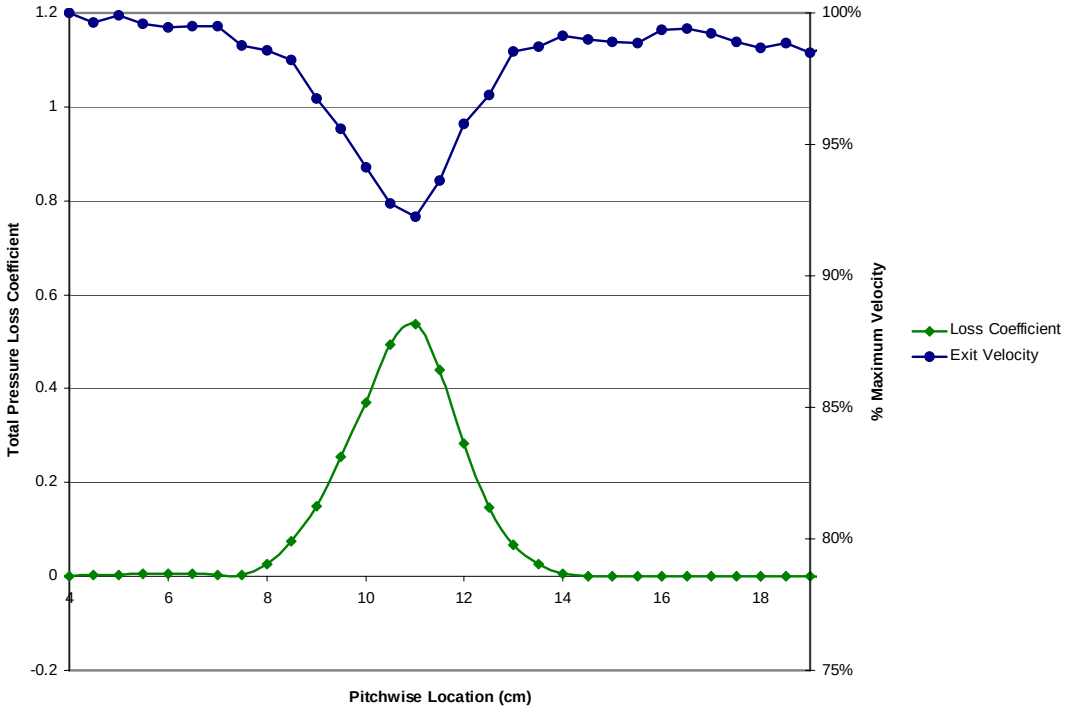

Figure 79. GH1R characterization profile for average Reynolds number of 91,918

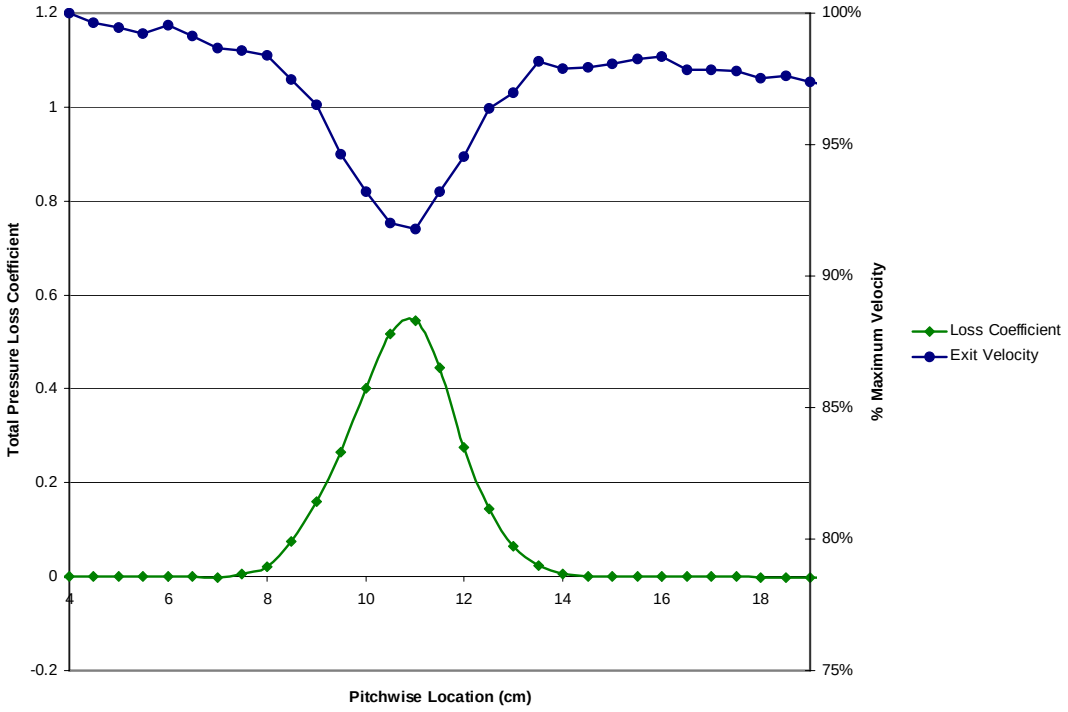

Figure 80. GH1R characterization profile for average Reynolds number of 91,353

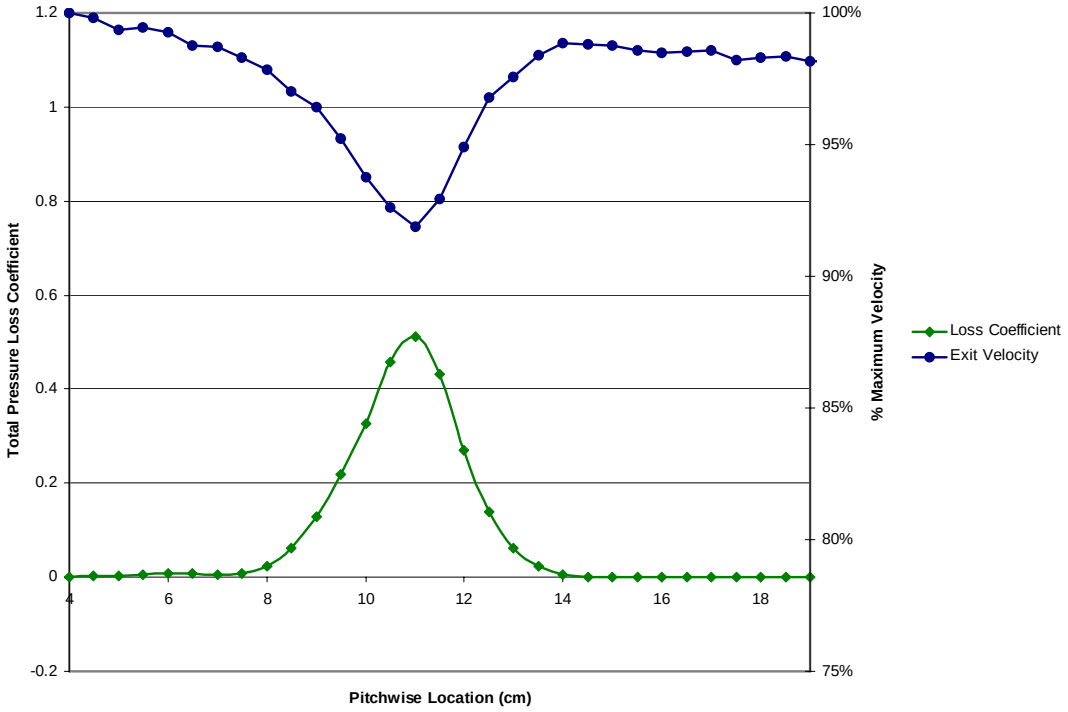

Figure 81. GH1R characterization profile for average Reynolds number of 96,860

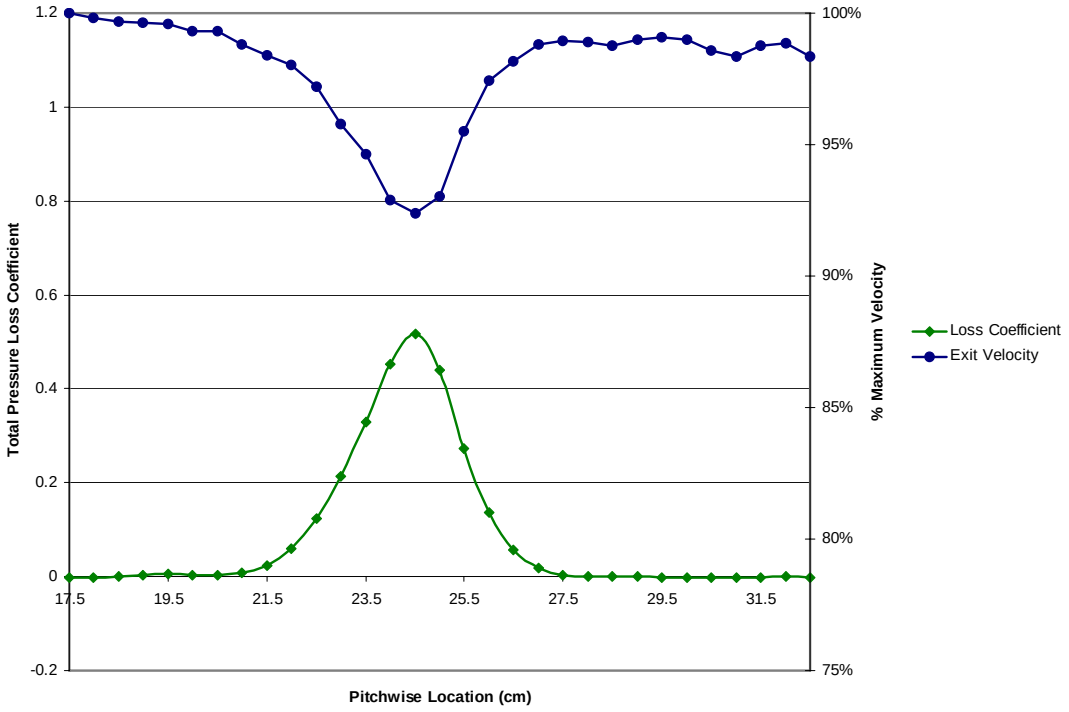

Figure 82. GH1R characterization profile for average Reynolds number of 98,548

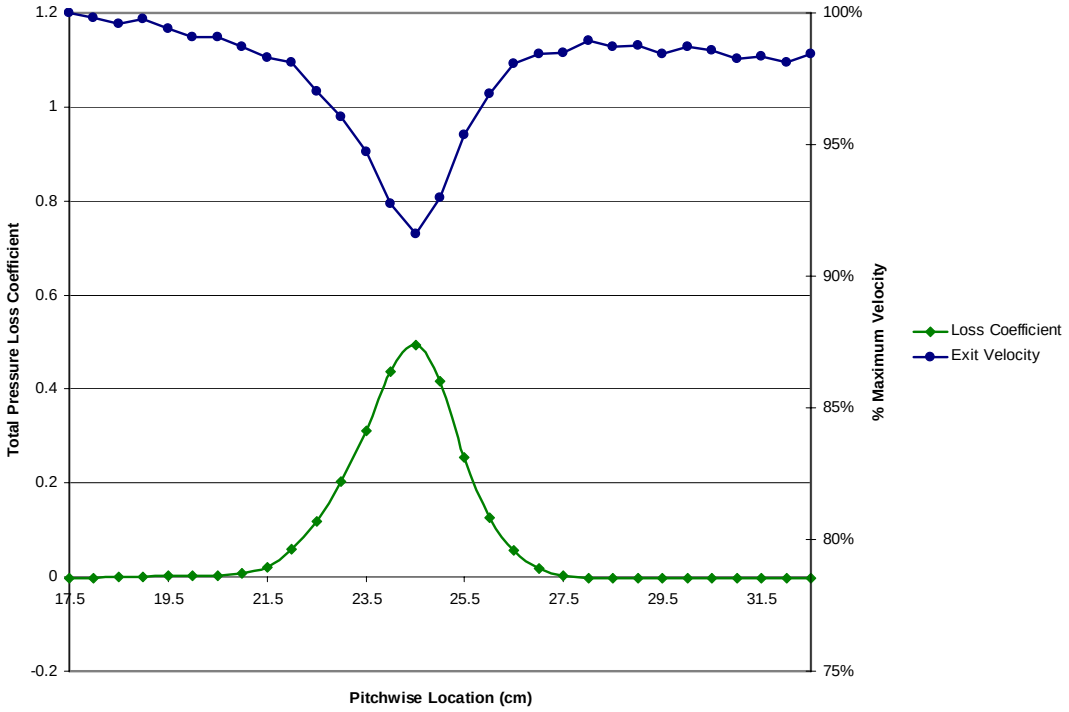

Figure 83. GH1R characterization profile for average Reynolds number of 99,732

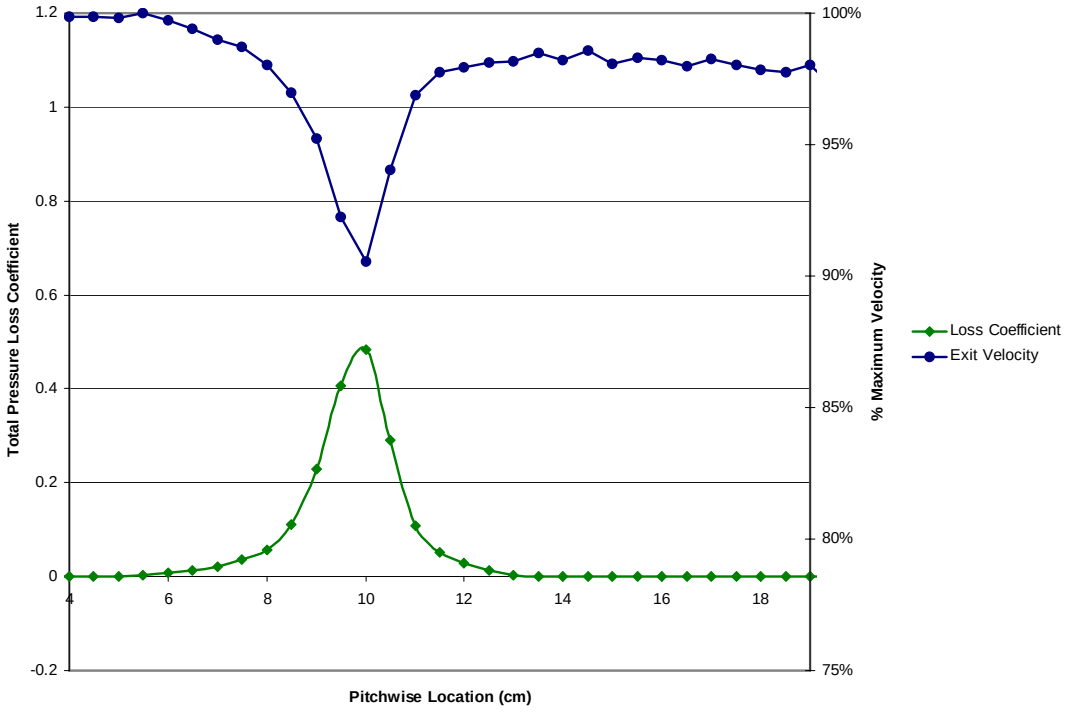

Figure 84. GH1R characterization profile for average Reynolds number of 101,737

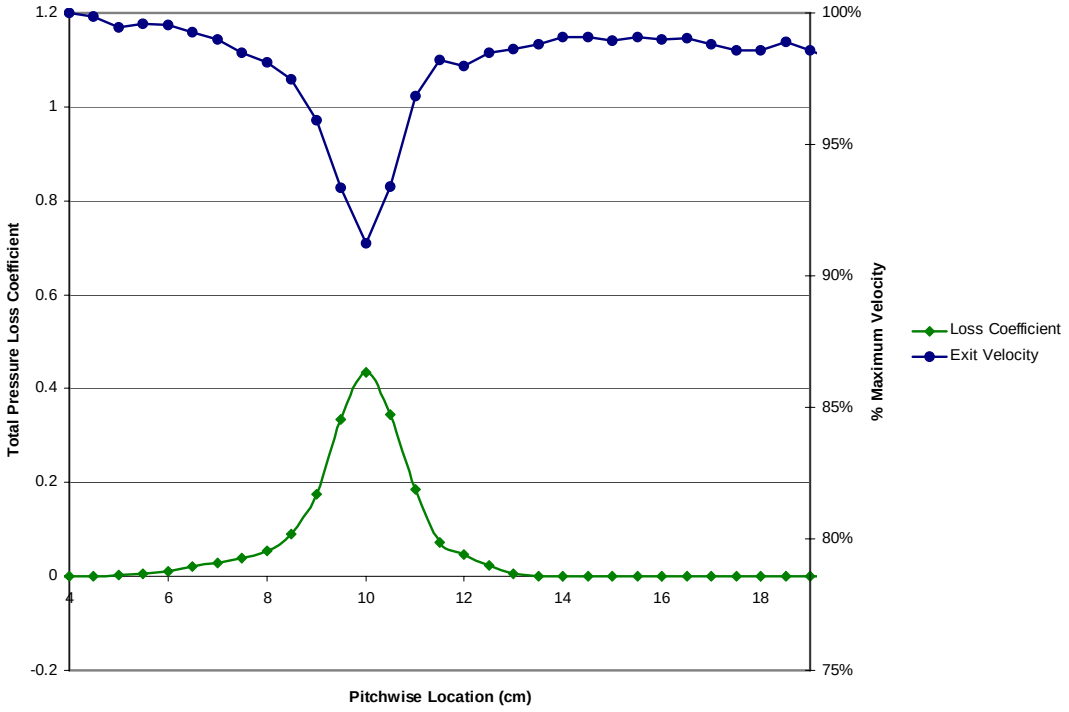

Figure 85. GH1R characterization profile for average Reynolds number of 101,829

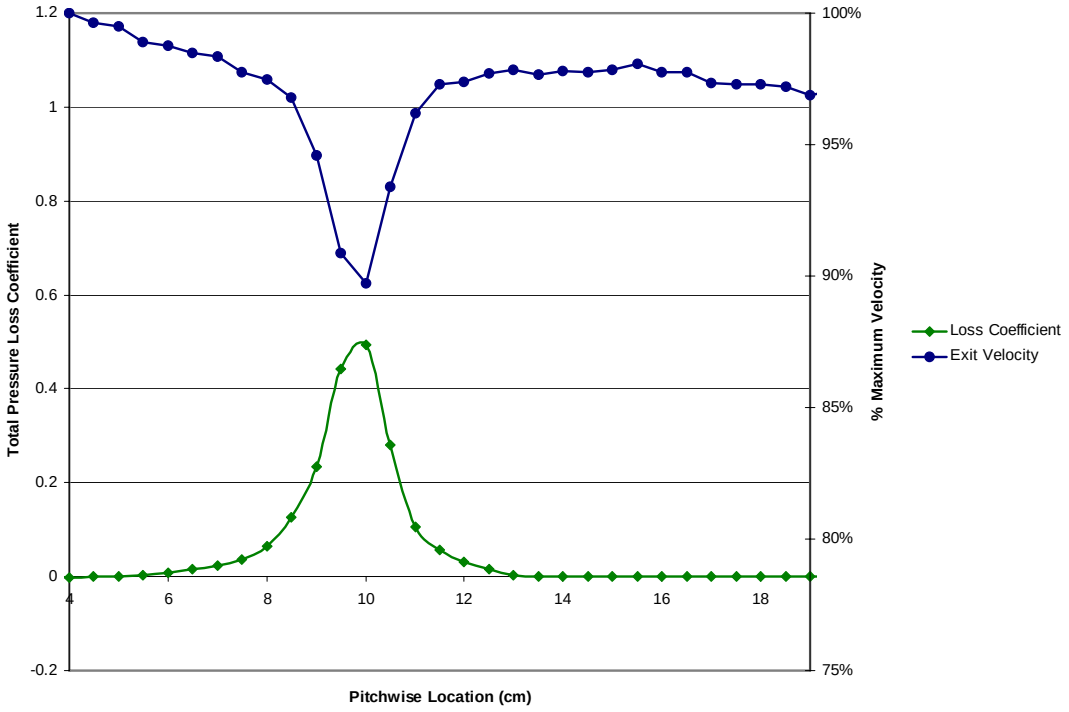

Figure 86. GH1R characterization profile for average Reynolds number of 102,101

APPENDIX E. Data Tables

Table 5. Summary of integrated total pressure loss data for the GH1R blade set

Goal Re of Run	Blade 5 Average Re Using Inlet Hot-film	Recalculated Blade 5 Average Re Using Pitot-static Probe Velocity	Average Pitot-static Probe Inlet Velocity	Integrated Sum Total Pressure Loss Coefficient (cm)	GH1R Pitch (cm)	Integrated Total Pressure Loss Coefficient	Average Hot-film Outlet Velocity	Motor Speed of Wind Tunnel	Date of Run
10000	9933	10387	0.97	2.8527	14.8	0.1927	1.63	4.3	08/06/05
15000	14752	15551	1.47	2.4921	14.8	0.1684	2.46	6	08/07/05
15000	14767	15787	1.39	2.9879	14.8	0.2019	2.50	5.9	8/5/2005
20000	19594	20152	1.88	2.5812	14.8	0.1744	3.29	7.2	08/06/05
25000	24367	24739	2.30	2.2296	14.8	0.1506	4.07	8.5	08/06/05
25000	24310	25478	2.41	2.3276	14.8	0.1573	4.07	8.9	08/07/05
30000	29104	29776	2.78	2.2452	14.8	0.1517	4.87	9.9	08/06/05
30000	29792	31302	2.98	2.4105	14.8	0.1629	4.99	10.6	08/07/05
35000	34081	34216	3.17	2.4986	14.8	0.1688	5.60	11.1	08/06/05
35000	34695	36244	3.45	2.3305	14.8	0.1575	5.77	11.8	08/07/05
40000	39259	40002	3.73	1.8559	14.8	0.1254	6.52	12.7	08/06/05
40000	38966	41203	3.97	1.9595	14.8	0.1324	7.05	13.7	08/03/05
45000	44001	44485	4.29	1.7243	14.8	0.1165	8.10	14.4	07/25/05
45000	43568	45237	4.31	1.8429	14.8	0.1245	7.17	14.4	08/07/05
50000	48979	47607	4.54	1.6513	14.8	0.1116	7.91	15	07/28/05
50000	48806	48460	4.38	1.6080	14.8	0.1087	7.65	14.8	07/29/05
50000	49359	48630	4.65	1.7725	14.8	0.1198	8.68	15.5	07/19/05
45000	44707	50489	3.96	1.8489	14.8	0.1249	7.08	13.9	07/29/05
50000	48989	51895	4.99	1.6026	14.8	0.1083	8.28	16.6	08/04/05
55000	54648	52631	4.83	1.5701	14.8	0.1061	8.76	16	07/28/05
50000	49886	53193	4.91	1.8942	14.8	0.1280	8.88	16.6	08/01/05
55000	54201	53673	4.87	1.7393	14.8	0.1175	8.60	15.5	07/29/05
60000	57631	57812	5.60	1.3720	14.8	0.0927	10.80	18.3	07/26/05
60000	58666	58834	5.54	1.5283	14.8	0.1033	9.01	18.1	07/29/05
50000	49836	62333	4.80	1.7307	14.8	0.1169	8.74	16.9	08/02/05
60000	59321	62775	6.08	1.5324	14.8	0.1035	10.50	19.7	08/02/05
60000	60058	62857	5.96	1.6187	14.8	0.1094	10.59	19.4	08/01/05
65000	63572	63261	5.57	1.5022	14.8	0.1015	10.08	18.6	07/29/05
70000	69999	72637	6.89	1.4734	14.8	0.0996	12.36	22.1	08/01/05
70000	69319	73492	7.08	1.3840	14.8	0.0935	12.41	22.7	08/02/05
75000	73508	75686	7.30	1.3946	14.8	0.0942	14.60	23.5	07/25/05
80000	79080	76617	7.39	1.3140	14.8	0.0888	13.33	23.1	07/27/05
80000	78911	81606	7.73	1.5233	14.8	0.1029	14.27	24.5	08/02/05
80000	78503	83016	7.97	1.4990	14.8	0.1013	14.59	25.4	08/02/05
75000	73068	83467	6.47	1.3820	14.8	0.0934	11.65	21.9	07/28/05
90000	87683	91353	8.61	1.4711	14.8	0.0994	15.76	27.2	08/03/05
90000	89254	91918	8.68	1.4537	14.8	0.0982	15.67	27.3	08/02/05
100000	98452	96860	8.90	1.3542	14.8	0.0915	15.63	28.3	07/29/05
100000	98452	98548	9.36	1.3301	14.8	0.0899	16.56	29.3	07/20/05
100000	97412	99732	8.91	1.2608	14.8	0.0852	16.19	28.3	07/20/05
100000	96256	101737	9.74	0.9280	14.8	0.0627	17.15	30.7	08/03/05
100000	99158	101829	9.58	0.9415	14.8	0.0636	17.40	30	08/02/05
100000	95977	102101	9.78	0.9727	14.8	0.0657	16.28	30.8	08/04/05

Table 6. Averaged integrated total pressure loss data for the GH1R blade set

Reynolds Number Band	Average Blade 5 Re	Maximum ITPLC of Band	Minimum ITPLC of Band	Average ITPLC of Band
10000	10387	0.1927	0.1927	0.1927
15000	15669	0.2019	0.1684	0.1851
20000	20152	0.1744	0.1744	0.1744
25000	25108	0.1573	0.1506	0.1540
30000	30539	0.1629	0.1517	0.1573
35000	35230	0.1688	0.1575	0.1631
40000	40602	0.1324	0.1254	0.1289
45000	44861	0.1245	0.1165	0.1205
50000	49416	0.1249	0.1083	0.1146
55000	53166	0.1280	0.1061	0.1172
60000	59659	0.1169	0.0927	0.1043
65000	62964	0.1094	0.1015	0.1048
75000	74608	0.0996	0.0888	0.0940
80000	81606	0.1029	0.1029	0.1029
85000	83242	0.1013	0.0934	0.0973
90000	91635	0.0994	0.0982	0.0988
95000	96860	0.0915	0.0915	0.0915
100000	100789	0.0899	0.0627	0.0734

APPEDIX F. Data Correction

By at first taking data at 10,000 Reynolds number increments, starting at 100K and working down to 20K, it appeared that the data was nicely forming a line. Next the gaps were filled in starting at 95K and working to 15K by 10K steps. At this point it appeared that the data was forming a ling with a “knee” or rapid change around a Reynolds number of 50,000. In order to better develop this “knee” many data sets were taken between 40K and 60K. At this point the first problem was noted. As seen in Figure 87, which is a graph of the data at this point in the study, there is a large amount of scatter for repeated runs. This was thought to possibly be bad data runs or an effect of the flow in Reynolds numbers near this ‘knee”. To check this, runs at a Reynolds number of 100K which is the most stable region were repeated, unfortunately the scatter was also found at this higher Reynolds number, which can also be seen in Figure 88.

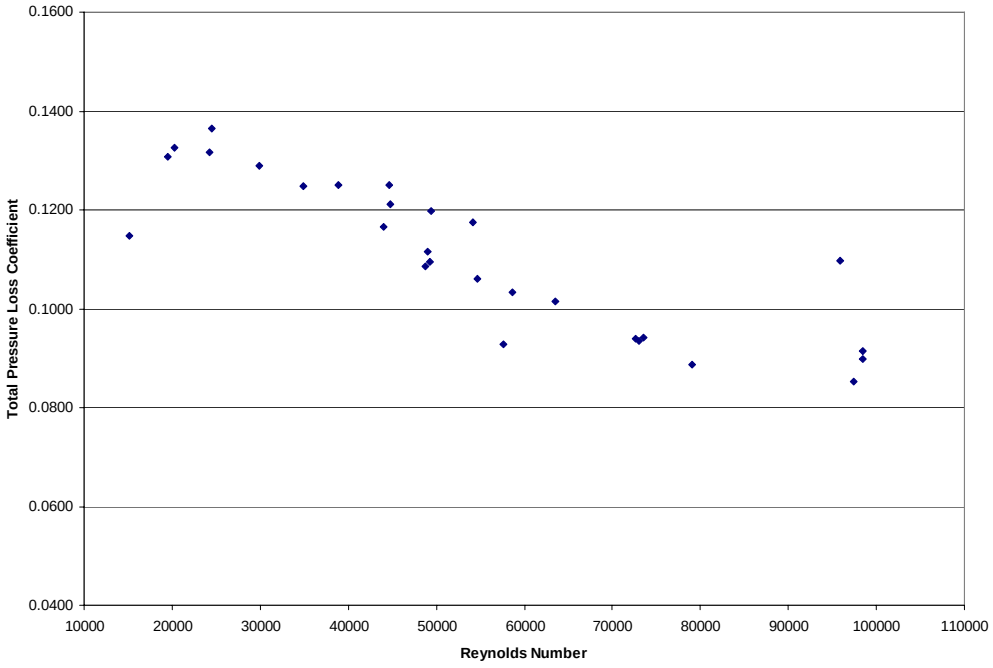

Figure 87. Early integrated total pressure loss coefficient data for the GH1R blade set

At this point another round of trouble shooting was begun. It was thought that all the bugs had been worked out in the validation process discussed in Appendix A.

Unfortunately, two new bugs were found that greatly affected the data. First, the reference temperature being called up by the data acquisition VI was actually a thermocouple monitoring the air conditioned instrumentation rack rather than the temperature at the inlet of the test section. It was also found that a conversion subroutine to convert Fahrenheit to Celsius was incorrect. Both of these problems were a great concern because the reference temperature is not outputted in the data files, and could not be checked. This reference temperature is also used by the IFA-300 to both calibrate the hot-films and calculate velocity during the data runs using the hot-film. This was an immense problem since the 28 runs constituted 70 hours of data runs, and could not be easily redone. It is unknown how long these problems have been present. They may have affected any of the previous tests done in this wind tunnel.

Luckily due to the need of pressure measurements, we had pitot-static probe data that could be used to calculate inlet velocity and in turn Reynolds number. All that was needed was a reference temperature. The Wright Patterson Air Force Base weather shop was able to provide hourly weather conditions for the past two months, which could be matched to the time stamp on each data file. We now had all that was needed to correct the data.

$$\nu = \sqrt{\frac{2\left(P_{stagnation} - P_{static}\right)}{\rho}} \tag{25}$$

$$Re = \frac{\rho \cdot \nu \cdot C}{\mu} \tag{26}$$

Equation 25 was used in conjunction with the new reference temperatures provided by the weather shop to calculate velocity using the pitot-static probe data taken during each test set. With this newly calculated velocity and new reference temperature

and dew point temperature the Reynolds number was then calculated using equation 26. The results of this newly calculated Reynolds number on the data set are shown it Figure 88.

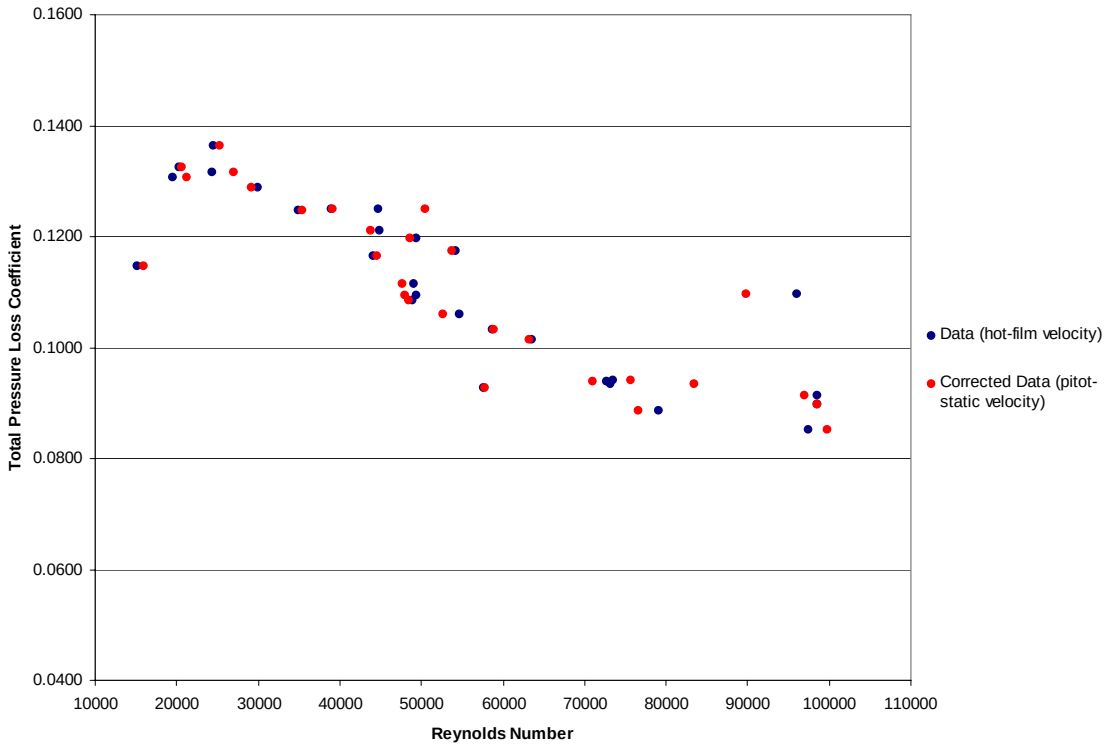

Figure 88. Comparison of original data to data with corrected Reynolds number

It can be seen in Figure 86 that some data points were changed very little. The data sets with little change were taken on cooler days, so the air conditioned cabinet temperature was somewhat close to the actual inlet temperature. The data sets with the greatest change are on the hotter days with a much greater temperature change. The temperature conversion bug only affected the inputted dew point temperature, which had little effect on the data set to begin with, so, though this was corrected, very little change will be seen due to it. If zero is inputted for the dew point temperature, it only affects the Reynolds number by about 3K, so the dew point has a very small effect on the Reynolds number calculation. Unfortunately, this temperature problem also affected the hot-film

calibration, so velocities are only good for relative comparisons, though they are only off by about 10%. The hot-films were not recalibrated, because we wanted to be able to make these comparisons to the numerous data sets already run. Reynolds numbers will be manually calculated using the method described above for all future runs.

Next multiple data runs were taken with the new corrected VI. The Reynolds number is still being recalculated using the pitot-static probe velocity due to the possibly faulty hot-film calibration and for comparison reasons. The new data points fell along the expected line, though scatter was still observed. These new data points with the correct reference temperature can be seen in Figure 89.

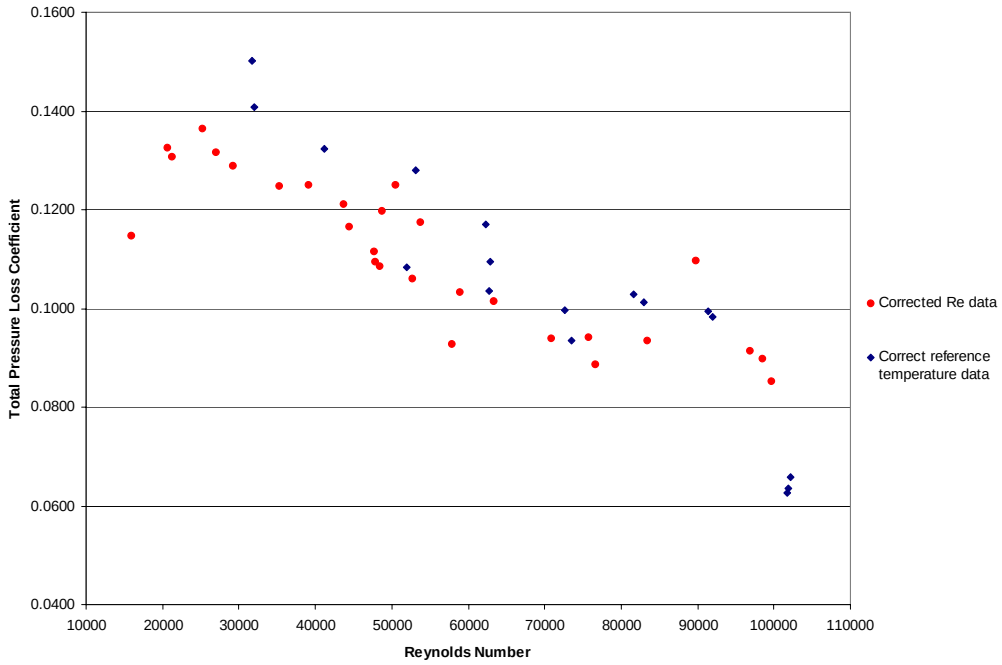

Figure 89. Comparison of corrected data to data taken with the correct reference temperature

The next possible cause of the data scatter is lack of resolution with in the tunnel pressure measurement set up. It was also noted that data for Reynolds numbers below 25K showed a noticeable drop in total pressure loss coefficient. This does not make

sense; TPLC should generally increase with decreased Reynolds number. In order to investigate this possibility, a new much smaller range, higher resolution pressure transducer was calibrated and replaced the current pressure transducer. The original pressure transducer was a Druck model LPM 5481 with a range of -0.2 in H20 to.8 in H20. The new pressure transducer is a Druck model LPM 9481 with a range of 0.0 to .04 in H2O. Both have an input voltage of 10 to 30 Vdc and an output voltage of 0 to 5 Vdc. The new pressure transducer can only be used for Reynolds numbers at or below 45K. At Reynolds numbers greater than 45K the direct differential samples of inlet and exit total pressures is too large for this pressure transducer. The new data with the higher resolution pressure transducer is shown in Figure 90.

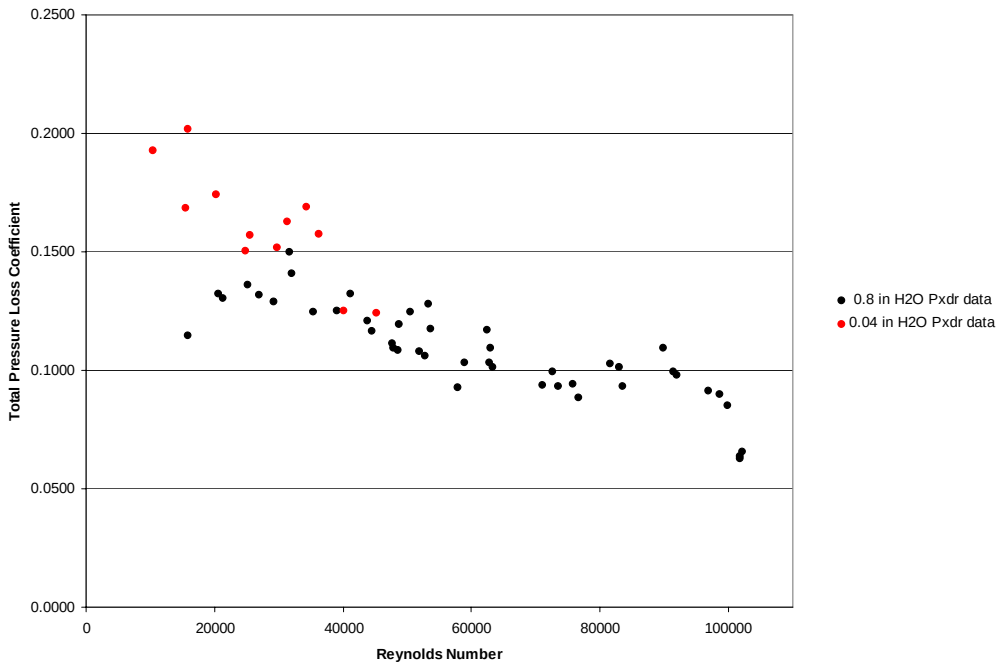

Figure 90. Comparison of GH1R integrated total pressure loss coefficient data taken using the higher resolution 0.04 in H2O pressure transducer data, to data taken with the standard 0.8 in H2O pressure transducer

It can be seen that the new data matched previous data fairly well for Reynolds numbers above 40K. The data for Reynolds numbers below 40K is noticeably different than the previous data. It appears that for Reynolds numbers below 40K the 0 to .04 in H2O pressure transducer is required. It also shows that some of the scatter at higher Reynolds numbers is most likely due to lack of pressure resolution, since it displays similar trends. After studying the data, a 0 to .08 in H2O pressure transducer would be a better choice for data collection for Reynolds numbers above 45K.

APPENDIX G. Boundary Layer Profiles

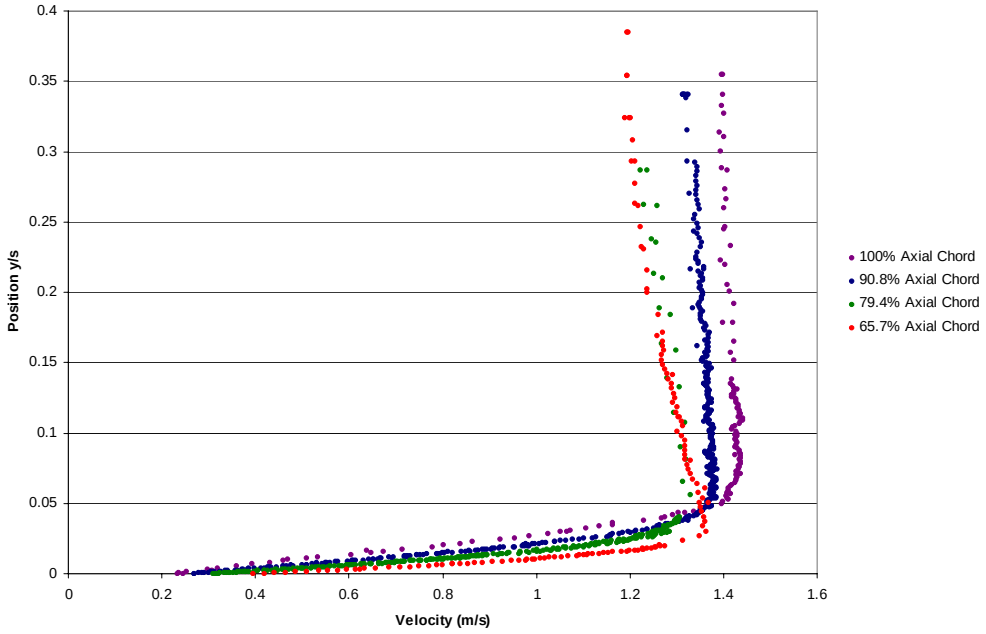

Figure 91. Boundary layer profiles for GH1R at Re 10K and Tu 1%

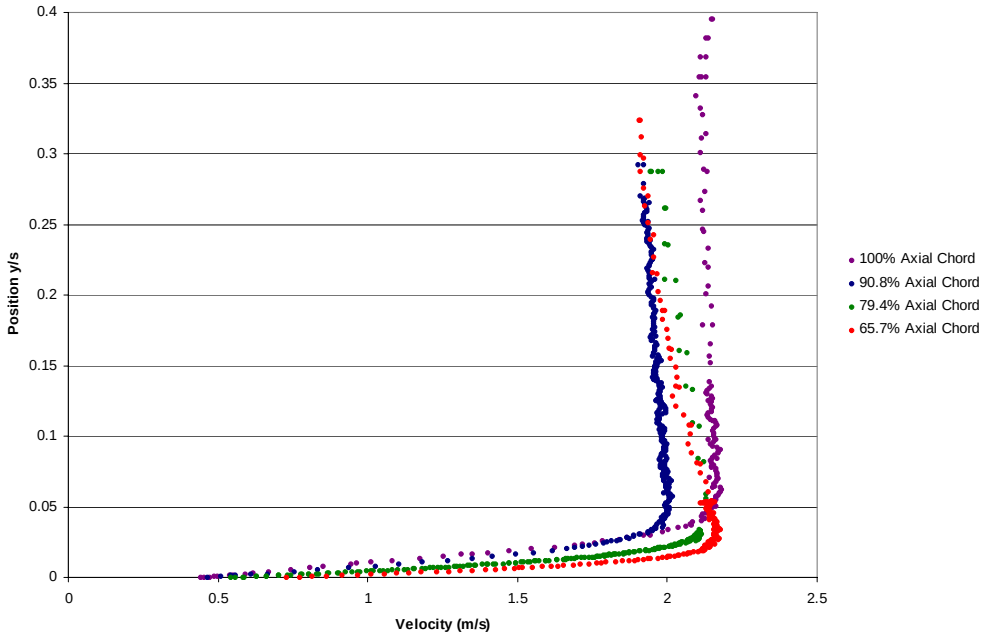

Figure 92. Boundary layer profiles for GH1R at Re 15K and Tu 1%

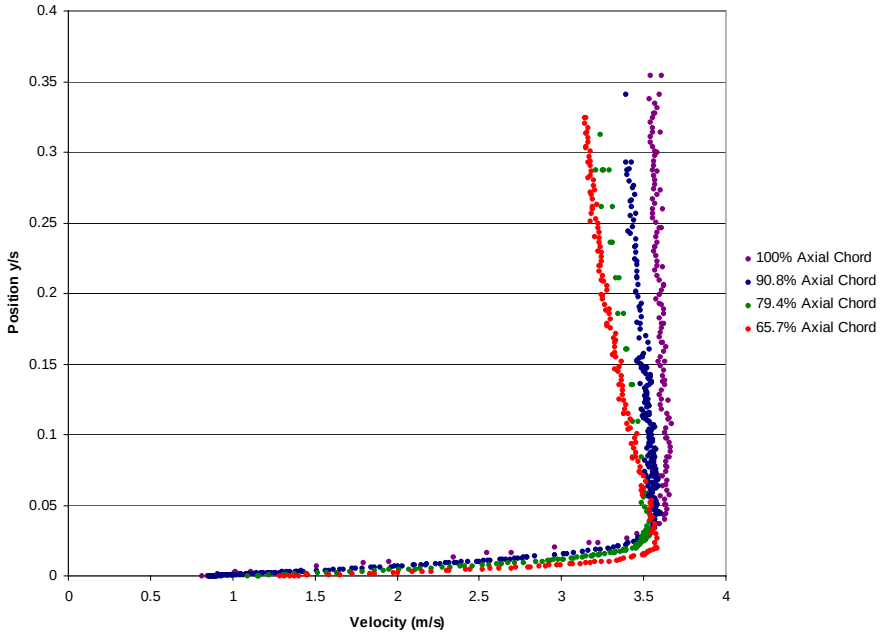

Figure 93. Boundary layer profiles for GH1R at Re 25K and Tu 1%

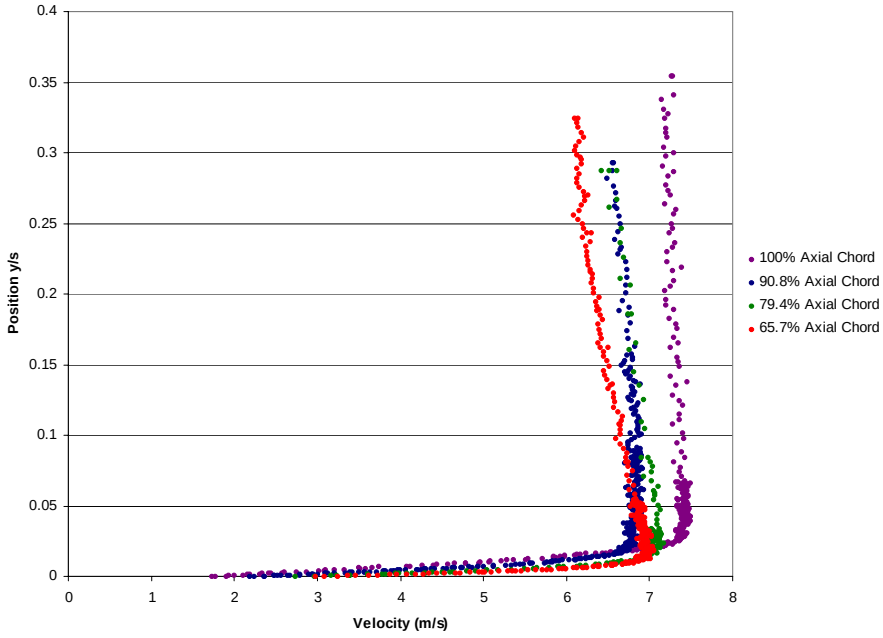

Figure 94. Boundary layer profiles for GH1R at Re 50K and Tu 1%

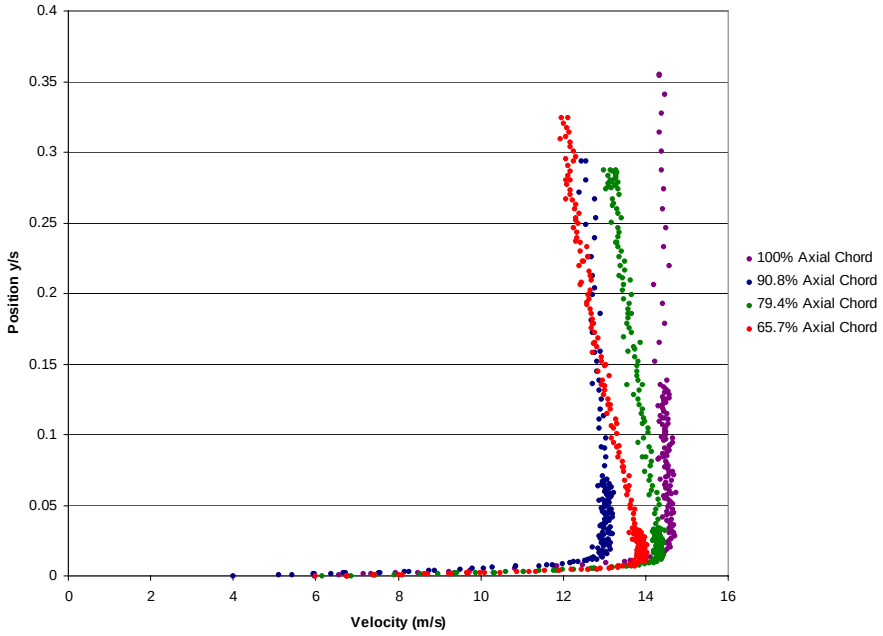

Figure 95. Boundary layer profiles for GH1R at Re 100K and Tu 1%

References

1. Mustin, Jeff, 1st Lt, USAF. "Future Employment of Unmanned Aerial Vehicles," *Aerospace Power Journal*, 3rd Qtr:86-97, (Summer 2002).

2. Lake, James P., "Flow Separation Prevention on a Turbine Blade in Cascade at Low Reynolds Number." PhD Dissertation, Air Force Institute of Technology, 1999. AFIT/DS/ENY/99-01.

3. Rouser, Kurt, P., "Use of Dimples to Suppress Boundary Layer Separation on a Low Pressure Turbine Blade." Masters Thesis, Air Force Institute of Technology, 2002. AFIT/GAE/ENY/02-13.

4. Garg, Vijay K., "Low-Pressure Turbine Separation Control- Comparison With Experimental Data", NASA/CR---2002-211689

5. Schobeiri, Meinhard T., Burak Ozturk, David E. Aships, "On the Physics of Flow Separation Along a Low Pressure Turbine Blade Under Unsteady Flow Conditions", NASA/TM---2003-212290

6. Halstead, D.E., D.C. Wisler, T.H. Okiishi, G.J. Walker, H.P. Hodson and H.W. Shin, "Boundary Layer Development in Axial Compressors and Turbines Part 1 of 4: Composite Picture." *International Gas Turbine Institute and Aeroengine Congress and Exposition*, Houston, TX, June 1995. ASME Paper No. 95-GT-461.

7. Halstead, D.E., D.C. Wisler, T.H. Okiishi, G.J. Walker, H.P. Hodson and H.W. Shin, "Boundary Layer Development in Axial Compressors and Turbines Part 3 of 4: LP Turbines." *International Gas Turbine Institute and Aeroengine Congress and Exposition*, Houston, TX, June 1995. ASME Paper No. 95-GT-463.

8. Werle, M.J. "Compressor and Turbine Blade Boundary Layer Separation." *AGARD Conference Proceedings*, AGARD-CP-351 (1983).

9. Mayle, R.E. "The Role of Laminar-Turbulent Transition in Gas Turbine Engines." *Journal of Turbomachinery*, 113:509-537 (October 1991). ASME Paper No. 91-GT-282.

10. Addison, J.S. and H.P. Hodson. "Modeling of Unsteady Transition Boundary Layers." *International Gas Turbine and Aeroengine Congress and Exposition*, Orlando, FL, June 1991. ASME Paper No. 91-GT-282.

11. Walker, G.J. “The Role of Laminar-Turbulent Transition in Gas Turbine Engines: A Discussion.” *Journal of Turbomachinery*, 115:207-217 (April 1993).

12. Mattingly, J.D. *Elements of Gas Turbine Propulsion*. McGraw-Hill, Inc., New York, 1996.

13. Moran, Michael J. and Howard N. Shapiro. *Fundamentals of Engineering Thermodynamics*. John Wiley and Sons Inc., New York, 1988.

14. Casey, John P., “Effect of Dimple Pattern on the Suppression of Boundary Layer Separation on a Low Pressure Turbine Blade.” *Masters Thesis*, Air Force Institute of Technology, 2004. AFIT/GAE/ENY/04-M05.

15. Rivir, R.B. “Transition on Turbine Blades and Cascades at Low Reynolds Numbers.” *Technical Report WL-TR-96-2084*, Wright Laboratory, 1996.

16. Sharma. O., 1998, “Impact of Reynolds Number on LP Turbine Performance,” *Proceedings of the 1997 Minnowbrook II Workshop on Boundary Layer Transition in Turbomachines*, NASA CP-1998-206958, 1998, pp. 65-69.

17. Murawski, C.G., T.W. Simon, R.J. Volino and K. Vafai, “Experimental Study of the Unsteady Aerodynamics in a Linear Cascade with Low Reynolds Number Low Pressure Turbine Blades.” *International Gas Turbine Institute and Aeroengine Congress and Exposition*, Orlando, FL, June 1997. ASME Paper No. 97-GT-95.

18. Qui, S. and T.W. Simon, “An Experimental Investigation of Transition as Applied to Low Pressure Turbine Suction Surface Flows.” *International Gas Turbine Institute and Aeroengine Congress and Exposition*, Orlando, FL, June 1997.

19. Simon, T.W. and R.J. Volino, “Separating and Separated Boundary Layers.” *Technical Report WL-TR-96-2092*, Wright Laboratory, 1996.

20. Hourmouziadis, J. “Aerodynamic Design of Low Pressure Turbines.” *AGARD*, pages 1-38. 1989. AGARD-LS-167.

21. Bruun, H.H. *Hot-Wire Anemometry*. Oxford University Press, Oxford, 1995.

22. Wilson, David Gordon *the Design of High-efficiency Turbomachinery and Gas Turbines*. Prentice-Hall, Inc., NJ, 1984.

23. Kuethe, Arnold M. *Foundations of Aerodynamics.* John Wiley and Sons, inc., NJ, 1998

Vita

Captain Timothy Lyle Garmoe graduated from Butler High School, Butler, MO in May 1992. He entered college at The University of Kansas (KU), Lawrence, KS, in August 1992. He graduated from KU in May 1997, earning a Bachelor of Science degree in Mechanical Engineering and was granted a commission in the USAF.

Captain Garmoe's first assignment was to Los Angeles Air Force Base (AFB) and where he was assigned to the MILSATCOM Join Program Office. Captain Garmoe was in charge of software maintenance and upgrades for the MILSTAR satellite. After about a year in this position, he was chose for the Education with Aerospace (EWA) program. This consisted of working with the Aerospace Corporation for a year, during which he designed a Ball-pocket bearing tester and did research on space grade lubricants. After the completion of the EWA program, Capt. Garmoe was assigned to the Launch Programs Directorate, where he worked as the Lead Propulsion Engineer for the Atlas rocket program.

Captain Garmoe's second Assignment was to Tyndall AFB, Panama City, FL where he served in the 82nd Aerial Targets Squadron's Special Device's flight. While stationed at Tyndal AFB, Captain Garmoe designed modification for the QF-4 aircraft in the support of operational test and evaluation of aircraft and weapons systems. Captain Garmoe also attended Florida State University (FSU) in the evenings, and his studies culminated in a Master of Business Administration (MBA) degree in 2003.

Captain Garmoe was selected to enter the Air Force Institute of Technology Graduate School of Engineering and Management, Wright-Patterson AFB, Dayton, OH.

There he worked towards a Masters of Science degree in Aeronautical Engineering. Upon graduation, he will be assigned to the Air Force Research Labs, Propulsion Directorate (AFRL/PR) at Edwards AFB California.

REPORT DOCUMENTATION PAGE

Form Approved
OMB No. 074-0188

1. REPORT DATE *(DD-MM-YYYY)*	**2. REPORT TYPE**	**3. DATES COVERED** *(From – To)*
09-02-2005	Master's Thesis	August 2003 – September 2005

4. TITLE AND SUBTITLE

Characterization of the Global Hawk Low Pressure Turbine First Rotor

5a. CONTRACT NUMBER

5b. GRANT NUMBER

5c. PROGRAM ELEMENT NUMBER

6. AUTHOR(S)

Garmoe, Timothy, L., Captain, USAF

5d. PROJECT NUMBER

5e. TASK NUMBER

5f. WORK UNIT NUMBER

7. PERFORMING ORGANIZATION NAMES(S) AND ADDRESS(S)
Air Force Institute of Technology
Graduate School of Engineering and Management (AFIT/EN)
2950 Hobson Way
WPAFB OH 45433-7765

8. PERFORMING ORGANIZATION REPORT NUMBER

AFIT/GAE/ENY/05-S02

9. SPONSORING/MONITORING AGENCY NAME(S) AND ADDRESS(ES)
AFRL/PRTT
Attn: Dr. Rolf Sondergaard
1950 5th Street
WPAFB OH 45433-7251 DSN: 785-7190

10. SPONSOR/MONITOR'S ACRONYM(S)

11. SPONSOR/MONITOR'S REPORT NUMBER(S)

12. DISTRIBUTION/AVAILABILITY STATEMENT
APPROVED FOR PUBLIC RELEASE; DISTRIBUTION UNLIMITED.

13. SUPPLEMENTARY NOTES

14. ABSTRACT

The Air Force Research Laboratory, Propulsion Directorate at Wright Patterson Air Force Base has studied the performance of turbine blade geometries utilizing a large scale, low speed, drawdown wind tunnel in an effort to better understand gas turbine blade aerodynamics. Currently, the Air Force's Unmanned Aerial Vehicle (UAV) Global Hawk has been operated primarily at flight conditions other than the design point of its Allison AE3007H turbofan engine. This off design condition decreased the Reynolds number at the low pressure turbine causing losses in efficiency and loading. Two different blades were studied to maximize performance of the Global Hawk turbine. The first was an experimental, high turning angle blade designated the Pak-B and the second was based on the two dimensional mean diameter section of the first stage blade of the low pressure turbine used in the Global Hawk (GH1R). The Pak-B blade has been the subject of past research.

The primary goals of this study were to validate the wind tunnel after previous upgrades, physically modify the test section to accept the Global Hawk blades, and to characterize the GH1R blades.

A Reynolds number sweep was performed from 10K to 100K by 5K increments on a linear turbine cascade of 8 first rotor test blades. Measurements of wake velocity, total pressure losses, and boundary layer velocity were made to examine the flow. These measurements resulted in an averaged integrated total pressure loss profile for the Global Hawk first rotor. The operational primary mission inlet Reynolds number for the GH1R blade was calculated to be 13,500 and compared to the loss profile. It was shown that the Global Hawk first rotor has much lower losses than that of the Pak-B blade, and shows no signs of mid-line separation.

15. SUBJECT TERMS
Laminar Boundary Layer Separation, Boundary Layer Transition, Turbulent Boundary Layer, Low Pressure Turbine Blade, Low Pressure Turbine Blade Performance, Gas Turbine Engine, Low Reynolds Number, Boundary Layer Measurements, Wake Loss Measurements, Global Hawk

16. SECURITY CLASSIFICATION OF:			**17. LIMITATION OF ABSTRACT**	**18. NUMBER OF PAGES**	**19a. NAME OF RESPONSIBLE PERSON**
REPORT	**ABSTRACT**	**c. THIS PAGE**			Dr. Paul I. King (ENY)
U	**U**	**U**	**UU**	137	**19b. TELEPHONE NUMBER** *(Include area code)* (937) 255-6565, ext 4314; e-mail: Paul.King@afit.edu